EXPLORING THE SYNTHESIS AND CHARACTERIZATION OF NANOENERGETIC MATERIALS FROM SOL-GEL CHEMISTRY

A Dissertation
Presented to
The Academic Faculty

by

Jeremy D. Walker

In Partial Fulfillment
of the Requirements for the Degree
Doctor of Philosophy in the
School of Materials Science and Engineering

Georgia Institute of Technology
May 2007

EXPLORING THE SYNTHESIS AND CHARACTERIZATION OF NANOENERGETIC MATERIALS FROM SOL-GEL CHEMISTRY

Approved by:

Dr. Rina Tannenbaum, Advisor
School of Materials Science and Engineering
Georgia Institute of Technology

Dr. Naresh Thadhani
School of Materials Science and Engineering
Georgia Institute of Technology

Dr. Hamid Garmestani
School of Materials Science and Engineering
Georgia Institute of Technology

Dr. Karl Jacob
School of Polymer, Textile, and Fiber Engineering
Georgia Institute of Technology

Dr. Thomas Sanders, Jr.
School of Materials Science and Engineering
Georgia Institute of Technology

Date Approved: November, 10 2006

For my family and friends

ACKNOWLEDGEMENTS

I wish to extend my deepest, most sincere gratitude to my advisor, Dr. Rina Tannenbaum, for her guidance during our years together. I would also like to thank my committee members – Dr. Naresh Thadhani, Dr. Thomas Sanders, Dr. Hamid Garmestani, and Dr. Karl Jacob.

I also could not have finished this work without the help of my research group members, past and present: Melissa, Kasi, Wren, Dan, Erin, Larry, Kit, and Lex. Also, I want to thank all of the friends I have made over the years at Georgia Tech, from the early days to the end: Chuck, Phill, Brent, Chris, Heather, Matt, Rob, Shubhra, Laura, Scott, Dan C., Dan M., Kip, Lou, Morgan, Mike, Pete, and especially Jelila. I also greatly appreciate the Thadhani research group for allowing me to use their equipment (their DTA) time and time again.

I would also like to thank the money. This work was supported by the Air Force/Bolling AFB/DC MURI project on Energetic Structural Materials, award No. F49620-02-1-0382.

TABLE OF CONTENTS

LIST OF TABLES

LIST OF FIGURES

SUMMARY

Nanoenergetic composite materials have been synthesized by a sol-gel chemical process where the addition of a weak base molecule induces the gelation of a hydrated metal salt solution. A proposed 'proton scavenging' mechanism, where a weak base molecule extracts a proton from the coordination sphere of the hydrated iron (III) complex in the gelation process to form iron (III) oxide/hydroxide, $Fe^{III}_xO_yH_z$, has been confirmed for the weak base propylene oxide (PO), a 1,2 epoxide, as well as for the weak bases tetrahydrofuran (THF), a 1,4 epoxide, and pyridine, a heterocyclic nitrogen-containing compound. Gelation mechanisms for the formation of $Fe^{III}_xO_yH_z$ from THF and pyridine have been presented and confirmed through pH, XPS, and IR studies. THF follows a similar mechanism as PO, where the epoxide extracts a proton from the coordination sphere of the hydrated iron complex forming a protonated epoxide, which then undergoes irreversible ring-opening after reaction with a nucleophile in solution. Pyridine also extracts a proton from the hydrated metal complex, however, the stable six-membered molecule has low associated ring strain and does not endure ring-opening.

Energetic properties for the Fe_2O_3/Al and RuO_2/Al sol-gel synthesized systems are also presented. Sol-gel chemistry synthesizes x-ray amorphous oxide matrices which contain substantial quantities of residual water and organic species. The iron (III) matrix, formed from the addition of a weak base epoxide molecule to a hydrated iron (III) nitrate solution, consists of stoichiometric Fe_2O_3, FeO(OH), and $Fe(OH)_3$ and can only definitely be described as of $Fe^{III}_xO_yH_z$. XPS characterization of the metal oxide matrix synthesized from the addition of the weak base propylene oxide to a hydrated ruthenium (III) chloride solution corresponds to that of hydrous ruthenium (IV) oxide.

Fe_2O_3/Al energetic systems were synthesized from the epoxides PO, trimethylene oxide (TMO) and 3,3 dimethyl oxetane (DMO). Energetic systems formed from each epoxide were each synthesized with different components, including: varying concentrations of nano-scale Al, micron Al, and carbon nanotubes. Surface area analysis of the synthesized matrices shows a direct correlation between the surface area of the iron (III) oxide matrix and the quantified exothermic heat of reaction of the energetic material due to the magnitude of the interfacial surface area contact between the iron (III) oxide matrix and the aluminum particles. The Fe_2O_3(PO)/Al systems possess the highest heat of reaction values due to the oxide surface area available for contact with the aluminum particles. Also, within systems, 1:1 Fe:nano Al samples possess the highest heat of reaction. Samples with nano-scale Al particles start reaction at 430°C, before the melting point of Al, whereas samples containing micron-Al do not react until ~800°C, after the melting point of Al.

The RuO_2/Al energetic systems behave differently dependent on the atmosphere the sample is heated. Heating the RuO_2/Al samples in an inert atmosphere results in the complete reduction of the ruthenium oxide matrix to $Ru^{(0)}$ before reaction with the aluminum particles. This results in the exothermic formation of Ru_xAl_y intermetallics, with the stoichiometry dependent on the initial Ru:Al concentration. However, heating the samples in an oxygen-rich atmosphere results in an exothermic reaction between RuO_2 and Al. Post-reaction analysis of these samples reveals the sole existence of ruthenium (IV) oxide as the exothermic reaction vaporizes the aluminum particles.

CHAPTER 1

INTRODUCTION

Nanomaterials allow for the realization of materials properties unattainable in the bulk. Nanoenergetic materials, in which at least one of the component phases has particle dimensions on the nanometer scale, have superior exothermic characteristics and possess properties unobtainable by traditional energetic materials.[1-3] In general, energetic materials store energy in chemical form and are typically categorized as propellants, explosives, and pyrotechnics.[4-6] Energetic materials are categorized into two main classes: monomolecular energetic materials and composite energetic materials. Monomolecular energetic materials contain both fuel and oxidizing components in a single compound. These materials have a high energy release rate which is controlled mainly by chemical kinetics resulting in greater energetic power release, but with lower overall energetic release density.[7] Composite energetic materials offer energy release density values much greater than monomelcular materials.[8] However, in these materials energy release in governed by mass transport, resulting in slow release rates due to the large scales of the reactants. By synthesizeing composite energetic materials with components on the nano-scale, a superior class of energetic can be synthesized with high energy release densities as well as high energy release rates as mass transport issues are reduced on this scale. The classification of nanoenergetic materials examined here are comprised of a particulate metal fuel (e.g. Al, Ta, Cr) closely mixed with metal oxide particles (e.g. Fe_2O_3, MgO, CuO, WO_3), which, after a stress-induced oxidation-reduction

reaction, result in a substantial exothermic heat release. This variety of energetic reaction is classified as a thermite reaction[9] which is a self-propagating reaction with temperatures reaching several thousand degrees.[10, 11] In these materials, reactions between different metal oxide networks (oxidants) and dispersed metallic particles (fuels) will result in different energetic release rates and outputs. Figure 1.1 shows a schematic of such a material.

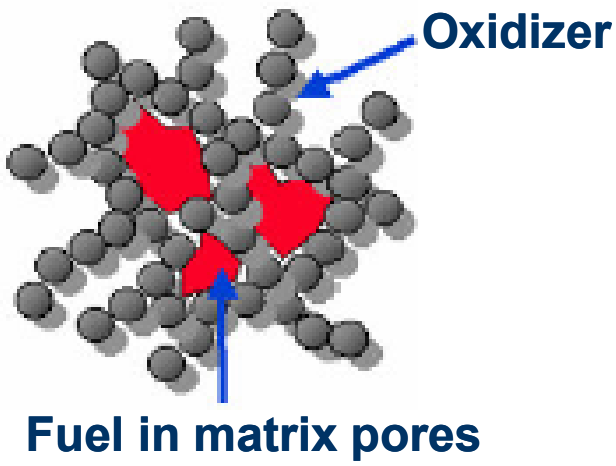

Figure 1.1: Schematic of energetic materials in which the oxidant and fuel phases are intimately mixed.[12]

In nanoenergetic composite materials, the interfacial contact area between the fuel and the oxidant phases is a crucial factor influencing the true magnitude of the exothermic heats of reaction. Poor surface contact between the oxidant and fuel results in exothermic heat of reaction values that are lower than the theoretical predictions, as with materials with phases of larger length scales. It is known that the number of contact points between the fuel and oxidant phases increases with decreasing particle size due to the increasing specific surface area.[13, 14] Hence, only systems with a large interfacial contact area between well dispersed fuels in close proximity to the metal oxide matrix,

such is the case with nanoscale components, can achieve heats of reaction that approach the predicted theoretical values.[15]

There are two possible methods of creating energetic materials comprised of a metal oxide matrix in intimate contact with zero-valent particulate fuels: (1) As in a traditional thermite, the mechanical mixing of powders of metal oxide and zero-valent fuel forms an energetic powder composite. A major problem that arises from this method is that the interfacial contact area between the two constituents is limited by the efficiency of the mixing process.[16, 17] Also, this is an inherently dangerous process due to safety issues associated with unplanned reactions if mixing were to initiate the thermitic reaction. (2) A second synthesis method is based on sol-gel chemistry, by which the energetic metal oxide/fuel composite materials are produced in solution, eliminating safety issues associated with mechanical mixing. The sol-gel method also provides a means of controlling properties such as particle size and matrix morphology.[18] This permits the metal oxide matrix to be tailored purely by changing the synthesis conditions.

The work presented is concerned with the synthesis and characterization of nanoenergetic composite materials synthesized via sol-gel chemistry with the goal of attaining distinctive metal oxide network morphologies, therefore resulting in different exothermic heats of reaction due to the varied interfacial surface area between the oxidant and fuel phases. In addition to altering the metal oxide network morphology, the metal oxide matrix itself will be altered. Analysis of the iron (III) oxide/aluminum and ruthenium (IV) oxide/Al systems are presented. Knowing the effect of metal oxide network morphology and the specific metal oxide is desired in order to possess the ability to select the most appropriate system for a particular application based on both the

desired reaction temperature as well as the desired heat of reaction. Along with quantification of the thermal analysis data, identification of the pre- and post-reaction phases of the synthesized material by x-ray diffraction and x-ray photoelectron spectroscopy, surface area analysis of the synthesized metal oxide matrices, and imaging through transmission electron microscopy and atomic force microscopy are to be performed.

Also, a mechanistic study is to be performed to probe the sol-gel formation of the iron (III) oxide matrix using different weak base gelation chemicals. Previous work, in which the weak base propylene oxide was used as the gelation agent, has proposed that a 'proton scavenging' mechanism was responsible for the formation of the xerogel. In the current study, this mechanistic view has been further investigated and generalized to encompass a broader class of weak bases, through pH studies, XPS and infrared spectroscopy.

CHAPTER 2

BACKGROUND

2.1 Overview

This chapter will discuss prior and current research of energetic materials, both nano-scaled and traditional macro-scaled. Section 2.2 will relate an overview of the two main classifications of energetic materials, monomolecular energetic materials and composite energetic materials. Section 2.3 will describe the current state of nanoenergetic materials, from synthesis to characterization. Section 2.4 will outline a proposed 'proton scavenging' mechanism in the sol-gel synthesis of various metal oxides from weak base molecules. Finally, Section 2.4 will discuss the relevance of the presented background information to the current project.

2.2 Energetic materials

2.2.1 Monomolecular energetic materials

Monomolecular energetic materials contain both the fuel and oxidizing component of an energetic material in a single molecule. Here, the fuel is usually carbon, with oxygen present in the molecule and in the atmosphere accounting for the oxidizing moieties. Energy release rates for these materials are high with reactions being controlled by intermolecular bond-breaking and temperature-dominated chemical kinetics.[17] The monomolecular decomposition reaction can reach energy release velocities of almost 7,000 m/s .[19] However, energy release densities are lower than composite energetic

materials; with the highest energy density for these materials currently one-half that of energetic composite systems.[7] A common example of a monomolecular energetic material is trinitrotoluene, or TNT. Figure 2.1 shows a schematic of this type of material.

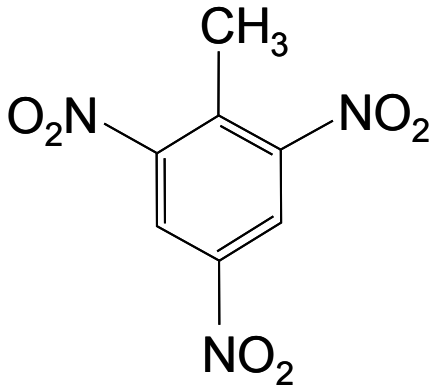

Figure 2.1: Drawing of the monomolecular energetic material trinitrotoluene, TNT.

2.2.2 Composite energetic materials

As opposed to monomolecular energetics, composite energetic materials comprise the other major category of energetic materials. These materials undergo exothermic reactions when two materials interact in oxidation-reduction reactions, as with thermite-type materials, or through the reaction of two metals to produce an intermetallic.

The oxidation-reduction thermite reaction was first described by Goldschmidt in 1908.[20] These extremely exothermic reactions involve a transfer of electrons between one reactant to the other, where, in essence, one reactant is oxidized, while the other reactant is reduced. Examples of such reactive mixtures and their associated theoretical exothermic heats of reaction are shown in Table 2.1. Note that all of these systems possess large theoretical exothermic heats of reaction. Fisher and Grubelich have

published an extensive list of oxidant/fuel systems as well as their calculated heats of reaction and adiabatic temperature, or the highest temperature reached during reaction.[9]

Table 2.1: Examples of reactive metal oxide/fuel thermite-type systems.[21]

$Fe_2O_3 + 2Al \rightarrow 2Fe + Al_2O_3 \Rightarrow \Delta H_R = -282kJ/mol$
$3MnO_2 + 4Al \rightarrow 3Mn + 2Al_2O_5 \Rightarrow \Delta H_R = -253kJ/mol$
$5MnO_2 + 4Ta \rightarrow 5Mn + 2Ta_2O_5 \Rightarrow \Delta H_R = -175kJ/mol$
$5Fe_2O_3 + 6Ta \rightarrow 10Fe + 3Ta_2O_5 \Rightarrow \Delta H_R = -197kJ/mol$
$6Cu_2O + 4Al \rightarrow 12Cu + 2Al_2O_3 \Rightarrow \Delta H_R = -233kJ/mol$
$5Cu_2O + 2Ta \rightarrow 10Cu + Ta_2O_5 \Rightarrow \Delta H_R = -177kJ/mol$

When initiated, these reactions emit large energy densities.[22] As described earlier, composite energetic materials possess twice the energy density as monomolecular energetic materials. However, the interfacial contact area between the two constituents is limited by the efficiency of the mixing process. Therefore due to the large scale of the reactants, the reaction is controlled by mass transfer limitations, resulting in low energy release rates.[4] Typical reaction velocities of composite energetics is on the order of 0.1-1 m/s, four orders of magnitude than monomolecular energetic materials.[23]

Exothermic reactions created from composite energetic materials are used in a wide variety of applications. These include a method for the welding together of railroad track, the underwater welding of metals, additives to explosives for even greater performance, car airbag initiators, and independent heat sources.[9] The decision as to the composition of the thermite mixture is dependent on the specific application. As the different mixtures release various quantities of heat, an application such as an airbag

initiator would require a mixture generating much less heat release as opposed to welding large quantities of railroad track, thereby making the knowledge of the heat of reactions of the various mixtures critical.

The traditional method of creating composite energetic materials comprised of a metal oxide in intimate contact with zero-valent particulate fuels is the mechanical mixing of powders of metal oxide and zero-valent fuel. However, this is an inherently dangerous process due to safety issues associated with unplanned reactions if mixing were to initiate the stress-induced reaction. Also, to vary energetic responses, the only variables to change are the oxidizer and fuel components in the system or to vary the ratio of oxidizer to fuel in the original composition.

The selection of the fuel component in composite energetic materials is dependent on numerous variables. Desired properties of the zero-valent metal fuel include high density, a low melt temperature, and low toxicity. High density of the fuel is desired for a maximum concentration of possible reactions with the oxidizing agent on the atomic level. Also, metals with large heats of formation for their oxides are desirable as these metals will generate the highest heat density. A low melt temperature is preferred as diffusion of the fuel particles increases in the liquid state to increase reaction velocity as mass transport issues are reduced. Having the fuel component possess low toxicity is self-explanatory, where a fuel such as beryllium would be a prime candidate with high potential energy content if not for health reasons.[9] Aluminum is typically desired as the fuel component due to its low melting temperature. Also, aluminum has a propensity to form a passive oxide later, Al_2O_3, to decrease the chance of unplanned reactions from the initial mechanical mixing.

2.3 Nanoenergetic composite materials

2.3.1 Advantages of the nano-scale

Recently, research has been focused on the development of nanoenergetic composite materials. As previously mentioned, traditional macro-scale composite materials possess large energy release densities. However, due to the large physical dimensions of both the oxidizer and fuel components, mass transport issues upon reaction initiation inhibit high energy release rates. The most effective method to decrease mass transport issues with these materials and to increase reaction rates is to reduce the scale of the oxidizer and fuel components. Presently, research is being performed on systems in the nano-scale. This decrease in the size of the reactants should result in faster energy release rates and higher energy outputs due to greater interfacial contact area between the oxidizer and fuel phases.

2.3.2 Iron (III) oxide/aluminum nanoenergetic materials

Due to the recent advances in nanotechnology, nano-scale fuel and oxidizer components have become commercially available. Mechanical mixing of these components can be accomplished to produce nanoenergetic composite materials. However, again, safety issues associated with unplanned reactions remain due to the physical mixing of the components.

As opposed to the mechanical mixing of oxidizer and fuel components, a second synthesis method is based on sol-gel chemistry, by which the energetic metal oxide/fuel composite materials are produced in solution, eliminating safety issues associated with

mechanical mixing and unplanned reactions. Sol-gel chemistry generates porous inorganic networks through the formation of a colloidal suspension (sol) and gelation of the sol to form a network (gel) in a continuous liquid phase, as shown in Figure 2.2.[24]

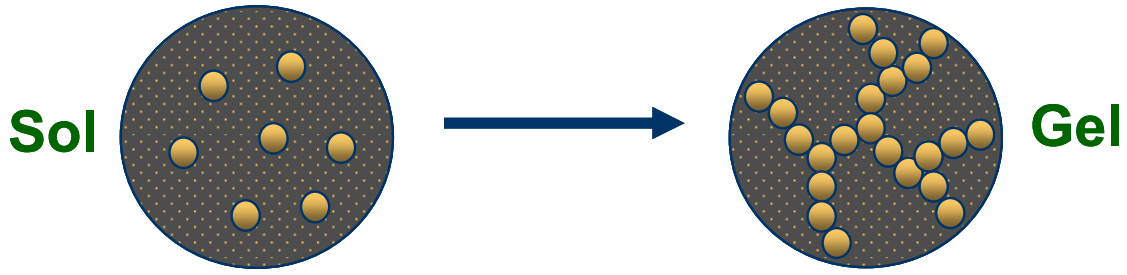

Figure 2.2: Schematic of the process where colloidal particles in suspension (sol) react to form a porous inorganic network (gel) within a liquid phase.

Sols are prepared mainly from metal salts, e.g. $FeCl_3$ and $Fe(NO_3)_3$, and metal alkoxides, e.g. $Al[O(CH_3)CHC_2H_5]_3$ and (TEOS), $Si(OC_2H_5)_4$.[25] Sols are also prepared from combinations of salts and alkoxides. The colloidal suspension of particles in the sol stage range in diameter from 2-200 nm, where the suspended particles must balance the forces of gravity and buoyancy to remain in suspension. The gel in sol-gel chemistry refers to the porous 3-dimensional interconnected solid network of the inorganic colloidal particles throughout the liquid medium. The sol to gel transition is continuous, and is characterized by the sharp increase in viscosity approaching infinity when nearing the gel point.[26] Beyond the gel point, there is also an increase in the elastic modulus of the material, as shown in Figure 2.3.[27] This type of chemistry is extremely versatile since it allows the formation of a large variety of metal oxides at relatively low temperatures via the processing of metal salt or metal alkoxide precursors,[28] enabling synthesis of yttria-

stabilized zirconia (YSZ), magnetite (Fe_3O_4), alumina (Al_2O_3), as well as numerous other metal oxides.[29]

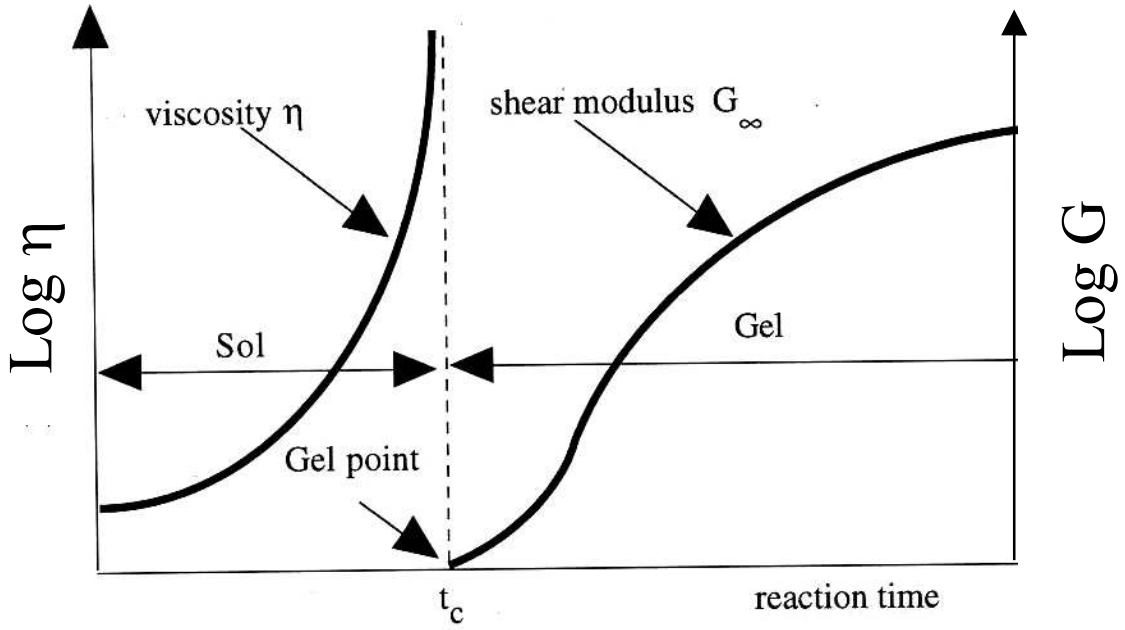

Figure 2.3: Schematic demonstrating the increased viscosity in the sol phase which approaches infinity at the gel point as well as the increased modulus in the gel phase in sol-gel chemistry.

The sol-gel reaction mechanism is comprised of two main steps: hydrolysis and condensation. The process starts when a metal salt, M_yX_z, which is demonstrated here, is dissolved into its respective metal cations and anionic species in an aqueous solution, as seen in Figure 2.4.

Figure 2.4: Dissolution of metal salt M_yX_z into metal cation M^{z+} and salt anion X^{y-} in an aqueous solution during sol-gel chemistry.

Figure 2.5 shows how the positively charged metal cations in solution, M^{z+}, attract the partial negative charge of the oxygen species in surrounding water molecules to form a hydrated coordination sphere.

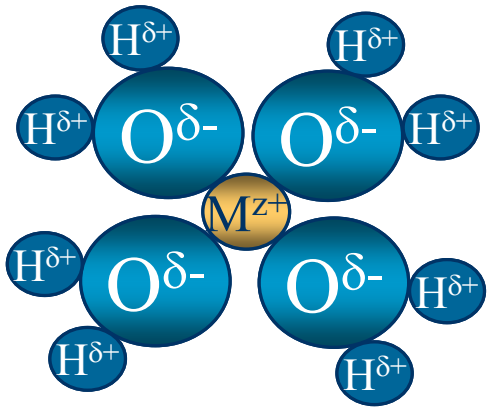

Figure 2.5: The positively charged metal cations in solution attract the negative charge of the oxygen species in surrounding water molecules.

Hydrolysis then occurs when the hydrated metal complex, $[M(OH_2)_N]^{z+}$, generated by the coordination of the water molecules in solution to the metal cations, reacts with a base in solution, such as water, through a proton transfer to form $[M(OH)(OH_2)_{N-1}]^{(z-1)+}$, a hydroxo ligand, and the conjugated acid, H_3O^+, shown in Equation 1:[30]

$$\underset{\text{Acidic hydrated metal complex}}{\left[M(OH_2)_N\right]^{z+}} + \underset{\text{Base}}{H_2O} \Leftrightarrow \underset{\text{Hydroxo ligand}}{\left[M(OH)(OH_2)_{N-1}\right]^{(z-1)+}} + \underset{\text{Conjugated acid}}{H_3O^+} \quad (1)$$

Equation 2 shows how the hydroxo ligand reacts with another base in solution, again such as water, deprotonating the hydroxo ligand, to form an oxo ligand, $[MO(OH_2)_{N-1}]^{(z-2)+}$ and the conjugated acid, H_3O^+:

$$\underset{\text{Acidic hydroxo ligand}}{\left[M(OH)(OH_2)_{N-1}\right]^{(z-1)+}} + \underset{\text{Base}}{H_2O} \Leftrightarrow \underset{\text{Oxo ligand}}{\left[MO(OH_2)_{N-1}\right]^{(z-2)+}} + \underset{\text{Conjugated acid}}{H_3O^+} \quad (2)$$

Via condensation, the oxo ligands polymerize to form a three-dimensional network of metal hydroxide/oxyhydroxides:

$$-MO(OH)-MO(OH)-$$

Further aging and drying to remove residual hydroxyl species yields the final stoichiometric metal oxide network, M_xO_z.[24] In the case of energetic materials, fuel particles can be dispersed within the sol phase, and as gelation occurs, the fuel particles become embedded within the matrix pores, resulting in a straightforward procedure to produce materials of this nature with excellent contact between the fuel and oxidizer components.

Researchers at Lawrence Livermore National Laboratories have previously synthesized Fe_2O_3/Al nanoenergetic composite materials of this nature using sol-gel

chemistry. Previously, iron (III) oxides formed by sol-gel synthesis have been extensively studied for their use as sensors, as catalysts, and as magnetic recording media.[31-37] The synthesized iron oxide matrix results in a high surface area/highly porous material.[38, 39] Gash et al. showed that using an iron (III) metal salt precursor in an alcohol solution representing the sol and adding an epoxide, such as an 1,2 epoxide, propylene oxide, as the gelation agent, a dry, porous iron oxide xerogel matrix is formed after the solvent in the gel is allowed to evaporate at ambient conditions. To create the nanoenergetic composite, the zero-valent metal fuel component, aluminum, is mixed into the iron salt solution in the sol-stage of the synthesis before gelation occurs in order to embed the Al particles within the pores of the forming three-dimensional network of iron oxide. This method allows for the intimate mixing of fuel and oxidant on the nano-scale. This situation is illustrated in Figure 2.6.

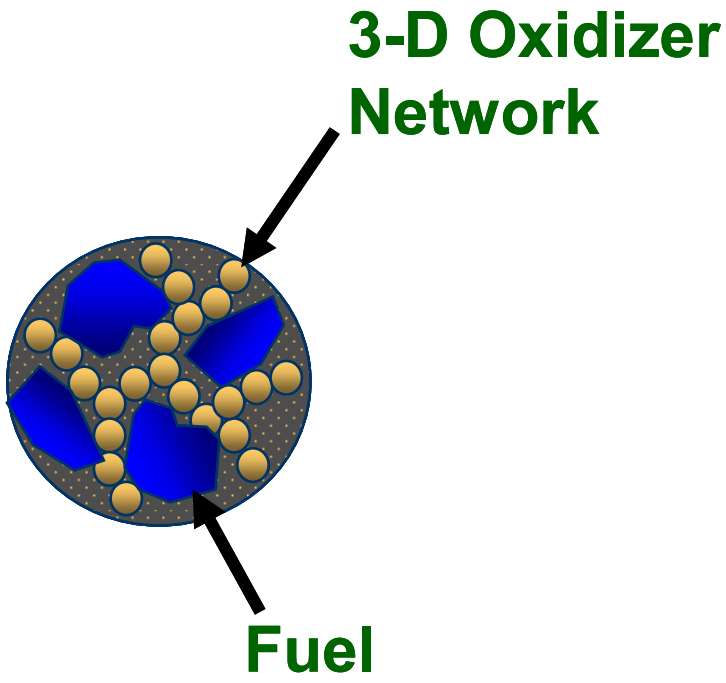

Figure 2.6: Schematic of a sol-gel synthesized energetic composite material where the fuel component resides within the pores of the three-dimensional oxide network.

The final morphology of the gel is dependent on the drying process. A xerogel is formed by the slow evaporation of liquid phase solvents contained within the gel and forms a solid that is approximately 50% porous due to densification by gravity. This ambient drying leads to the collapse of the pores and generates a gel of higher density as composed to aerogels where the solvents are exchanged with carbon dioxide under super-critical conditions resulting in a low-density material with higher porosity and surface area.[7] Specifically, the ambient drying of the as-synthesized gel leads to the collapse of the pores and generates a gel of high density with Fe_2O_3 particles of 2-5 nm when propylene oxide is used as the gelation agent, as shown in Figure 2.7(a).[40]

This basic procedure template can be altered by changing the gelation agent as a parameter in altering the matrix geometry. Research on the effect of changing the gelation agent has been performed by using a 1, 3 epoxide, trimethylene oxide, as opposed to the aforementioned 1, 2 epoxide, propylene oxide. The addition of trimethylene oxide as the gelation agent to the hydrated iron salt solution produces a fibrous network of Fe_2O_3 particles with diameter of 15-35 nm, shown in Figure 2.7(b). Also, by using another 1,3 epoxide, 3,3 dimethyl oxetane, a similar fibrous network of Fe_2O_3 particles with fibers of 3-5 nm form, as seen in Figure 2.7(c). This establishes that the metal oxide matrix can be altered purely by changing gelation agents.

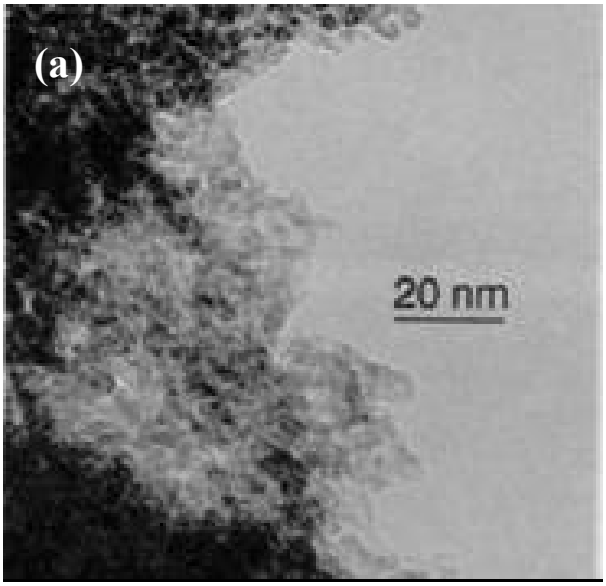

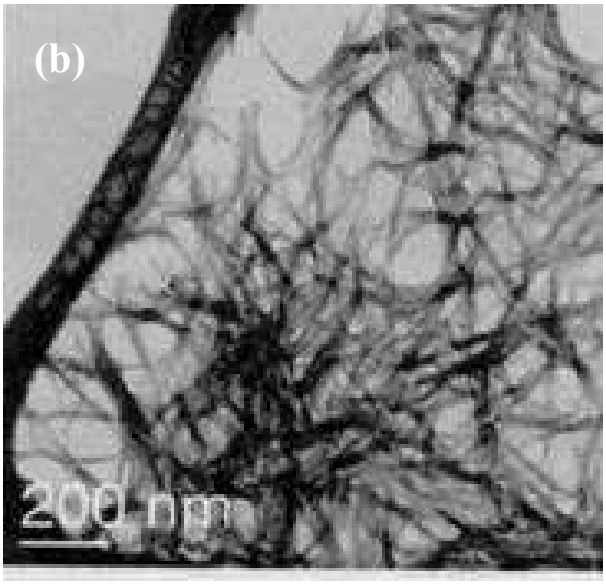

Figure 2.7: TEM images of sol-gel derived Fe_2O_3 materials using (a) propylene oxide (PO), (b) trimethylene oxide (TMO), and (c) 3,3 dimthyl oxetane (DMO) as the gelation agent.

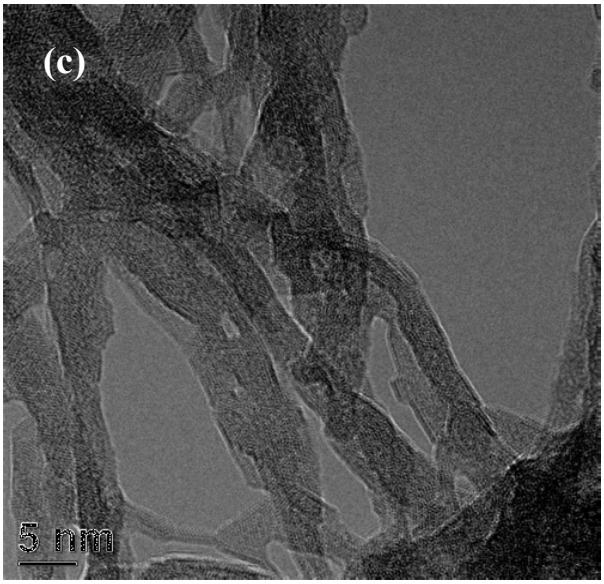

Figure 2.7 (continued)

The zero-valent metal fuel component, aluminum, is mixed into the metal oxide matrix in the sol-stage of the synthesis before gelation occurs to form the energetic material with aluminum particles embedded within the Fe_2O_3 matrix pores. The sol-gel synthesis route to produce nanoenergetic materials is schematically shown in Figure 2.8.

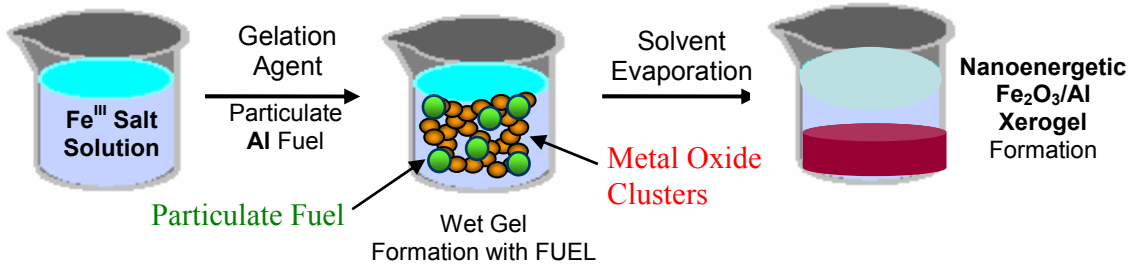

Figure 2.8: Schematic of synthesis of energetic nanomaterials from sol to gel phases for a Fe_2O_3/Al system.

Imaging the nanoenergetic material using propylene oxide as the gelation agent reveals iron (III) oxide clusters of 2-5 nm, as seen in Figure 2.9. Ultra fine grade (UFG) aluminum particles of 30 nm can be seen in contact with the metal oxide clusters.[5]

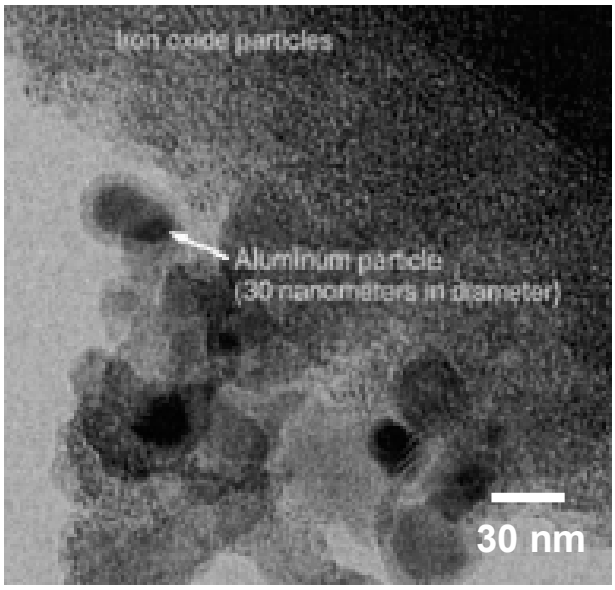

Figure 2.9: TEM image of sol-gel derived Fe_2O_3 materials using propylene oxide as the gelation agent showing iron oxide clusters of 2-5 nm in immediate contact with 30 nm diameter aluminum particles.

Energetic analysis of this material was performed using differential scanning calorimetry (DSC). The theoretical heat of reaction for this oxidant/fuel system (Fe_2O_3/Al) is -282 kJ/(mol Fe_2O_3 reactant). The experimental value of the heat of reaction of this material was -110 kJ/(mol Fe_2O_3 reactant), as shown in Figure 2.10. This lower than theoretical heat of reaction is explained as being a result of the partial surface oxidation of the aluminum particles which prevents the achievement of the theoretical yield, since this passivation layer, ~3 nm in thickness for 30 nm Al particles, reduces the ignition sensitivity of the particles.[41]

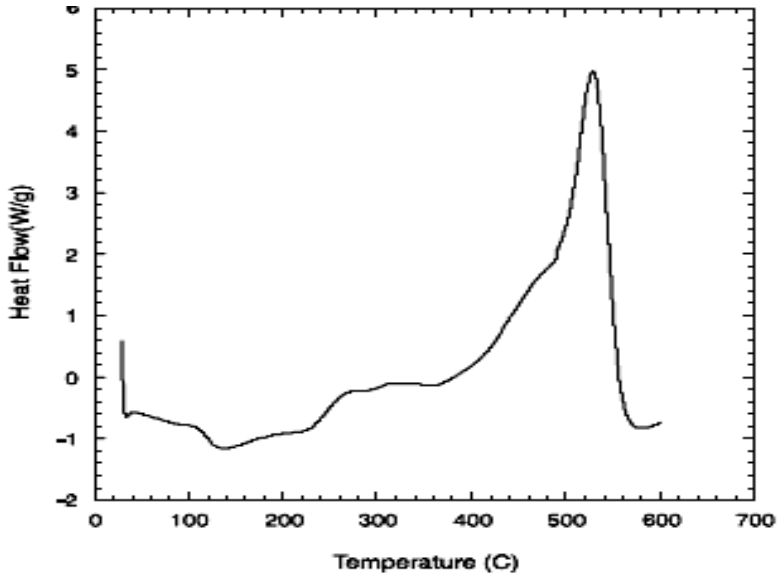

Figure 2.10: Thermal analysis data for heat of reaction of Fe_2O_3/UFG Al system derived from sol-gel chemistry.

However, energetic Fe_2O_3 samples synthesized from the gelation agents TMO and DMO, as shown in Figures 2.7(b) and 2.7(c), have not been studied for energetic properties. Figure 2.11 shows an illustration of how the formation of different metal oxide networks formed from sol-gel chemistry can possibly result in different interfacial surface area contact between the oxidizer and fuel components, resulting in different energetic responses. In the figure, the sample on the left, with the higher concentration of oxide particles in direct contact with the fuel particles, would result in higher exothermic release densities with the initiation of the thermite reaction.

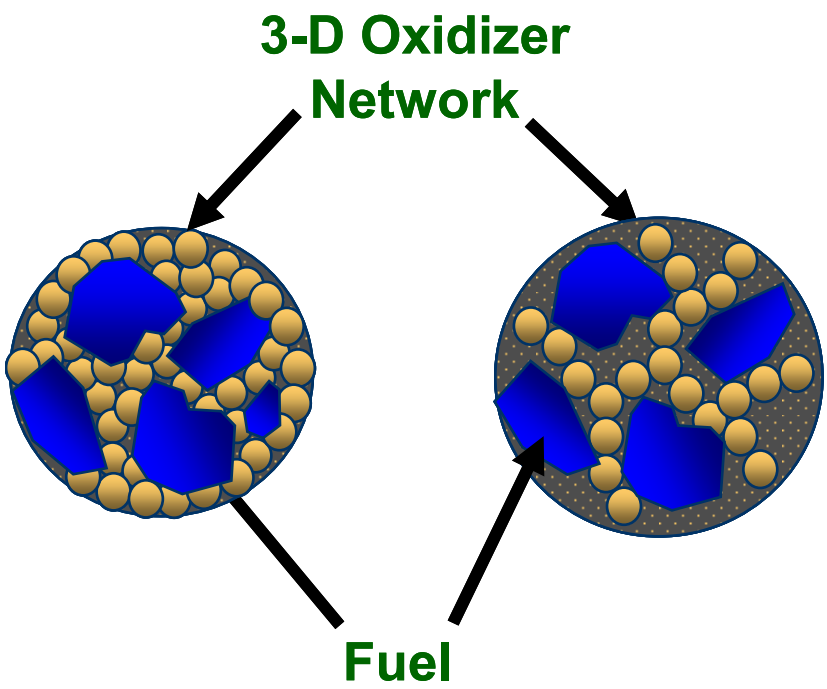

Figure 2.11: Illustration of the differing interfacial contact areas between fuel and oxidizer molecules arising from the difference in the morphologies of the metal oxide matrices. The configuration on the left, with greater interfacial surface area contact between the fuel and oxidizer components, will yield a greater heat of reaction after reaction.

In an effort to probe the effect of the surface area contact between the fuel and oxidizer particles on reaction initiation, Pantoya et al. researched the energetic behavior of composite energetic materials of molybdenum trioxide (MoO_3) and aluminum.[15] Experiments were performed on samples with nano-scale aluminum fuel particles with diameters of 17-202 nm. Also, experiments with aluminum fuel particles on the scale of 3-20 microns were carried out. In comparison to micron scale fuel particles, nano scale particles approach molecular dimensions and mixing at this level enhances the homogeneity of the mixture. The samples were synthesized by mechanically mixing the two constituents. The fuel:oxidizer ratio was 1.2:1, an excess of fuel particles is due to the inevitable oxidation of the pyrophoric aluminum particles. It should be noted that the

MoO_3 particles had a sheet-like crystalline structure with particles of varying sizes, ranging from as small as 100 nm. Their results indicate a clear disparity in the reaction ignition time between the samples containing nano-scale and micron-scale aluminum fuel particles. The composites containing nano-scale aluminum initiate reaction more than two orders of magnitude faster than the samples containing micron-scale aluminum. The nano aluminum samples start reaction in ~12 ms, where the micron aluminum samples react after ~6 seconds. However, within the nano-regime, the reaction initiation time did not vary significantly, all the samples reacted within 15-25 ms. However, the samples were still synthesized by mechanical mixing of the composite constituents where safety hazards remain for potential unplanned reactions.

To continue the sol-gel approach to the synthesis of nanoenergetic materials, Prakash et al. presented a novel approach to the synthesis of the metal oxide matrix in nanoenergetic materials.[4] Their reactions started with the same precursors as the researchers at Lawrence Livermore; however, the method synthesizes Fe_2O_3 via an aero sol-gel approach. This aero sol-gel method is designed to scale-down the full scale methods presented by Gash and perform the experiments in a single droplet. The researchers started the reaction using the same iron (III) salt/alcohol solution to which an atomizer ejected droplets of ~1 micron. These droplets were sent to a reactor where the solution droplets reacted with a 1,2 epoxide, 1,2-epoxybutane. Within the reactor, the droplets successfully gelled to form Fe_2O_3. The novel approach presents some issues. First, the Fe_2O_3 particles formed are larger than the 3-5 nm particles imaged by Gash. Particle size distribution revealed that the aero sol-gel method particles have a mean diameter of 180 nm. Again, increased particle size decreases possible interfacial surface

area between the oxidizer and fuel components, reducing reaction rates and energetic outputs. Second, the process only produces the oxidizer component. To synthesize the nanoenergetic material, the iron (III) oxide matrix synthesized here requires mechanical mixing with a fuel to produce the energetic material, again, leading to safety issues.

Kim et al. expounded upon the aero sol-gel synthesis procedure.[11] Here, an iron (III) salt solution in addition to zero-valent aluminum particles are each sent through separate atomizers where they interact within a reactor, which again contains the gelation agent 1,2 epoxybutane. Within the reactor, the iron (III) sol gels to form Fe_2O_3, leading to enhanced interaction with the aluminum particles introduced by the second atomizer. TEM images show Fe_2O_3 particles with mean diameters of 200 nm in direct contact with aluminum particles of 50 nm. This procedure creates a safer, more straightforward aero sol-gel method to produce Fe_2O_3/Al composite nanoenergetic materials, however, the larger diameter of the iron (III) oxide particles limits interfacial contact area between the two phases reducing energetic outputs.

Prentice et al. researched the tailoring of energetic outputs of Fe_2O_3/Al based nanoenergetic materials by adding a third reactant, SiO_2.[17] The researchers mixed aluminum nanoparticles into two different Fe_2O_3/SiO_2 oxidizer mixtures. One mixture was prepared by the mechanical mixing of purchased nanometer scale metal oxide particles. The second mixture was prepared by a similar sol-gel synthesis as described by Gash. The results showed the ability to control the exothermic output of various compositions of Fe_2O_3/SiO_2/Al. However, again, mechanical mixing of the oxidizer and fuel components was again employed. Also, the addition of SiO_2 was shown to decrease

reaction velocities. As there was no mention of particles sizes of the oxidizer phases, no conclusions in respect to interfacial contact area can be presented.

2.3.3 Ruthenium (IV) oxide/aluminum nanoenergetic materials

In addition to altering the gelation chemical to tailor the metal oxide matrix geometry, the epoxide addition synthesis procedure can be altered by replacing the hydrated iron salt with hydrated salts of other metals. This epoxide addition in the sol-gel formation of metal oxides has also been successful in the synthesis of other technologically-relevant oxides such as NiO,[42] Al_2O_3,[43] Cr_2O_3, ZrO_2, WO_3, as well as numerous other transition metals.[44] These oxides may be used in a variety of applications in the areas of sensors, optical materials, catalysts, gas separation, information storage, wet-type solar cells, oxide ion conductors for solid-oxide fuel cells, as well as many other research areas.[45-61] Ruthenium oxides have been prepared by sputtering,[62] cathodic electrosynthesis,[63] and solution chemistry including thermal decomposition of hydrated $RuCl_3$[64] and sol-gel processes.[65, 66] Anhydrous ruthenium oxide materials possess versatile functionalities and properties that make them useful in numerous industries. RuO_2 is known as an exceptional electrode material for high power and high energy density capacitors as a result of its high capacitance[67] and exhibits low resistivity and good thermal stability.[68, 69] It is also known to be a metallic conductor[70-72] and has been used as a catalyst for organic and inorganic reactions,[73, 74] an anode material in the production of chlorine,[75] and in cryogenic temperature sensors.[76] Due to its etching capability, RuO_2 is also a good candidate for the bottom electrode for high dielectric constant capacitors.[77] Hydrous ruthenium oxide, $RuO_2 \cdot xH_2O$, can be used as an

electrochemical capacitor due to its high energy density.[78] These hydrous materials possess high capacitance, low resistance,[79] and good electrochemical cyclability[80] with maximum capacitance values of the material occurring when $x \sim 0.5$.[81]

Suh et al. have demonstrated that the sol-gel epoxide addition method can produce ruthenium oxide aerogels of high porosity from hydrated ruthenium chloride solutions.[79] The research group examined materials properties, such as gelation time and phase identification, in addition to the capacitance of aerogels of the material. Surface area analysis of the aerogels reveals a nano-porous material with 18.3 nm to 23.6 nm, even after calcinations.

Nanoenergetic materials of hydrous ruthenium (IV) oxide and aluminum have not been reported in the literature. If this combination was to react, the balanced thermite-type reaction would be:

$$3RuO_2 + 4Al \rightarrow 2Al_2O_3 + 3Ru$$

Knowing that the standard heat of formation of anhydrous ruthenium (IV) oxide is -314.15 kJ/mol,[82] the heat of formation of alumina is -1,668 kJ/mol,[21] and the heat of formation of elements is zero, the calculation of the overall heat of reaction can be determined. The theoretical overall heat of reaction for this system is -2,424.6 kJ/mol, or -346.4 kJ/(mol reactant). This molar based heat of reaction value makes such a system more energetic than even the classic thermite, Fe_2O_3 and Al.

However, the energetic intermetallic reactions between composite ruthenium and aluminum materials have been reported. The main purpose of studying Ru_xAl_y intermetallics is due to the exceptional properties of the intermetallic. Mucklich et al. has compiled a thorough review of the intermetallic RuAl.[83] In respect to other aluminide

intermetallics with similar crystal structures, such as NiAl, CoAl, and FeAl, RuAl possesses superior properties. RuAl has higher ductility, higher toughness, and lower brittleness than other similar intermetallics. It has extraordinary corrosion resistance with electrical properties comparable to ruthenium metal. Energetically, RuAl has a large, negative heat of formation of -124.1 kJ/mol, indicating a strong chemical attraction between the two metals.

2.4 Proposed 'proton scavenging' mechanism

The general mechanistic view regarding the formation of the Fe_2O_3 xerogel by the addition of an epoxide to a hydrated iron salt precursor solution is based on the assumption that the gelation agent, propylene oxide, can be regarded as a 'proton scavenging' weak base that does not cause vigorous precipitation of Fe^{III}. The use of a weak base is emphasized, as strong bases are known to form iron oxide precipitates due to the rapid reaction rate of the base with the metal species.[84] Propylene oxide has traditionally been used in organic syntheses as an acid scavenger.[85] In this scenario, the propylene oxide extracts protons from the water molecules in the immediate coordination sphere of the hydrated metal complex, resulting in a protonated epoxide, as shown below in Equation 3.

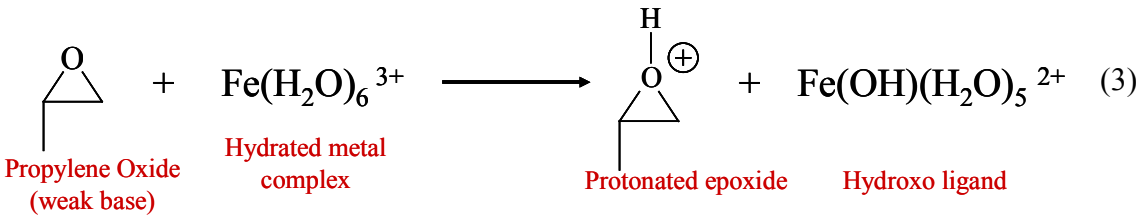

The protonated epoxide subsequently undergoes irreversible ring-opening by reacting with a nucleophile present in solution, either a nitrate ion or water. Also, as a result of this reaction, a diol is formed, leading to a net elimination of protons from solution, as shown in Equation 4. A nuclear magnetic resonance study has confirmed the presence of the diol species.

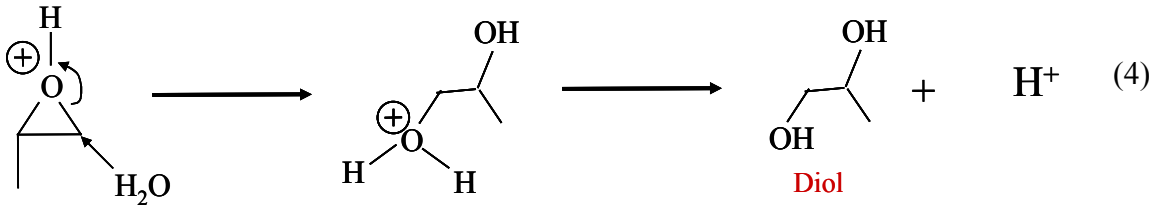

(4)

After further hydrolysis and condensation of the original hydrated metal complex, Fe_2O_3 is formed. These hydronium ions are eliminated from solution by bonding with the salt anions in solution, lowering hydronium ion concentration in solution, thereby leading to a proposed increase in pH with time. This hypothesis is validated by the confirmed increase in pH as a function of reaction time, as shown in Figure 2.12.[39]

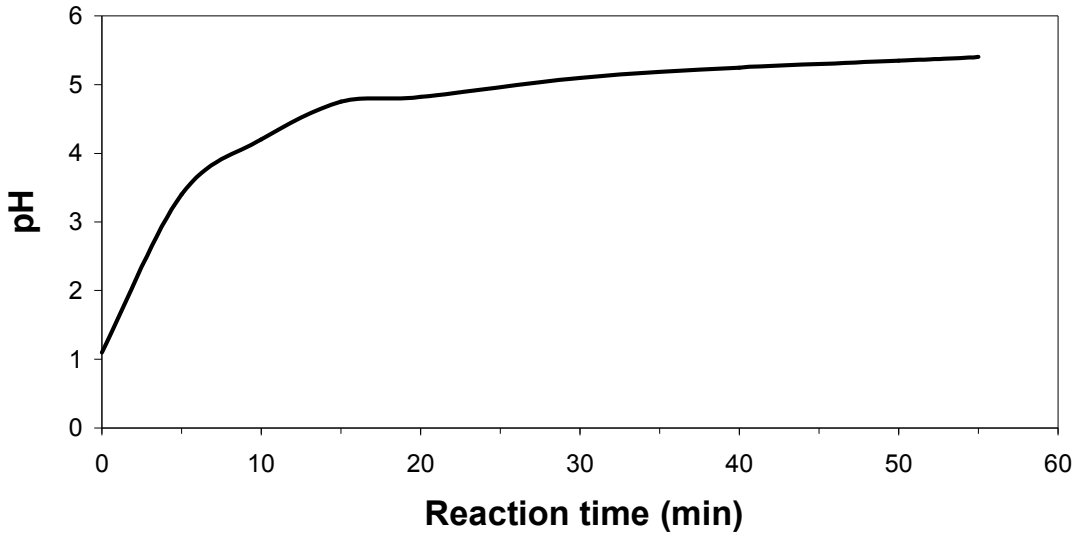

Figure 2.12: Reaction pH study of gel formed adding propylene oxide as gelation agent to an iron (III) salt precursor solution. Notice the increase in pH with increasing reaction time.

2.5 Relevance of current research with background

By reviewing the literature for nanoenergetic materials, much emphasis has been placed on the synthesis of energetic materials with nano-scaled dimensions. There is a definite advantage to using materials on this scale due to increased contact area between the metal fuel and oxidizer phases. From the epoxide addition sol-gel synthesis method, it is evident that metal oxides with different morphologies with varying surface areas are able to be synthesized. However, no published research has been performed to take advantage of this idea. This work focuses on exploiting this fact by synthesizing nanoenergetic materials of the iron (III) oxide and aluminum system from different gelation epoxides which have been shown to result in different metal oxide geometries in able to tailor the heat of reaction values of the exothermic thermite oxidation-reduction reaction. Also, novel ruthenium (IV) oxide and aluminum nanoenergetic systems were

synthesized as an extension of this same sol-gel synthesis procedure. Here, the metal oxide matrix has been changed, which will result in different energetic outputs. Confirming the sol-gel 'proton scavenging' synthesis will provide the researcher the knowledge of which gelation chemicals will induce gelation to produce further innovative metal oxide matrices.

CHAPTER 3

EXPERIMENTAL PROCEDURES

3.1 Overview

This chapter discusses the materials, experimental procedures, and characterization techniques used in this work. Section 3.2 discusses the materials used in the synthesis and characterization of metal oxide gels from sol-gel chemistry. Section 3.3 describes the experimental procedure in the elucidation of the 'proton scavenging' mechanism. Section 3.4 details the sol-gel procedures employed to produce nanoenergetic materials of iron (III) oxide and aluminum, while Section 3.5 details the procedure to synthesize ruthenium (IV) oxide and aluminum nanoenergetic materials. Section 3.6 describes the experimental techniques utilized throughout the research along with a brief description of the technique.

3.2 Materials

Ferric nitrate nonahydrate, $Fe(NO_3)_3 \cdot 9H_2O$; tetrahydrofuran (THF), C_4H_8O; pyridine, C_5H_5N; propylene oxide (PO), C_3H_6O, and micron scale aluminum powder were purchased from Fisher Scientific and used as received. Figure 3.1 displays the structure of these organic molecules.

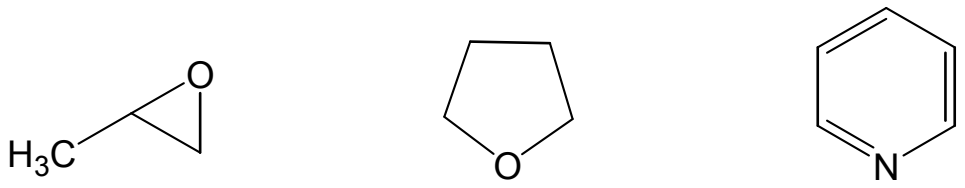

(a) (b) (c)

Figure 3.1: The structure of weak base molecules used as gelation chemicals: (a) propylene oxide (PO), C_3H_6O, (b) tetrahydrofuran (THF), C_4H_8O, and (c) pyridine, C_5H_5N.

Trimethylene oxide (TMO), C_3H_6O, and 3,3-dimethyloxetane (DMO), $C_5H_{10}O$, were purchased from Aldrich Chemical Company and used as received. Figure 3.2 shows the structure of these epoxides. Zero-valent aluminum particles with a mean particle size of 50 nm were purchased from Nanotechnologies, Inc. Ruthenium (III) chloride hydrate, $RuCl_3 \cdot xH_2O$, was also purchased from Fisher Scientific and used as received. Stock absolute ethanol and single-walled carbon nanotubes (CNT), 1.1 nm in diameter with lengths of 0.5 – 100 μm, were obtained from Aldrich and used as received.

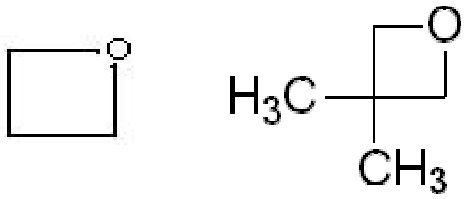

(a) (b)

Figure 3.2: The structure of epoxides: (a) trimethylene oxide (TMO), C_3H_6O, and (b) 3,3-dimethyloxetane (DMO), $C_5H_{10}O$.

3.3 Elucidation of sol-gel mechanism by epoxide addition

3.3.1 Synthesis of iron (III) materials by addition of weak base molecules

Syntheses were performed in 20 mL glass scintillation vials and performed under ambient conditions. For all syntheses, 0.65 g $Fe(NO_3)_3 \cdot 9H_2O$ was added to 3.5 mL of ethanol and stirred until the solid ferric nitrate component was completely dissolved in the ethanol. Then a 1.2 mL allotment of weak base, propylene oxide, THF, or pyridine, was added as the gelation chemical to the solution and stirred. After addition of the gelation chemical, times to gelation were monitored and recorded. After gelation occurred, the wet gels were covered and allowed to age for 24 hours. Then, the gels were allowed to dry in a fume hood under ambient conditions or heated at 60°C for seven days to allow solvents to evaporate. The dried xerogel materials were ground into a fine powder using a ceramic mortar and pestle.

3.3.2 pH studies of gel formation

A 0.43 M aqueous solution of Fe(III) was formed by adding 3.60 g $Fe(NO_3) \cdot 9H_2O$ to 20 mL of deionized water.[39] To this solution, 77 mmol of respective gelation chemical was added and continually stirred. pH measurements were taken using a Fisher Scientific Accumet AB15 pH meter consisting of a glass pH indicating electrode in conjunction with a silver/silver chloride reference electrode starting with time zero corresponding to the addition of the gelation chemical (i.e. pyridine). A 3-point calibration set at pH values of 4.0, 7.0, and 10.0 was performed on the pH meter prior to the onset of each experiment.

3.4 Fe_2O_3/Al nanoenergetic materials systems

3.4.1 Synthesis of Fe_2O_3 xerogels

For all syntheses, 1.30 g $Fe(NO_3)_3 \cdot 9H_2O$ was added to 7.0 mL of ethanol and stirred until the solid ferric nitrate component was completely dissolved in the ethanol. Finally, a 2.4 mL allotment of PO, TMO, or DMO was added to the solution and stirred, inducing gelation. The time to gelation for the syntheses was monitored and recorded. The as-synthesized wet gels were covered and allowed to age for 24 hours. Then the gels were dried in atmospheric conditions or in an oven at 60°C for 7 days which resulted in evaporation of solvents and densification of the samples to form xerogels.

3.4.2 Synthesis of Fe_2O_3/Al energetic materials systems

For all syntheses, 1.30 g $Fe(NO_3)_3 \cdot 9H_2O$ was added to 7.0 mL of ethanol and stirred until the solid ferric nitrate component was completely dissolved in the ethanol. Then 0.083 g of nano Al powder was added to the solution and continually stirred into the solution. This quantity of Al allows for a 1:1 Fe:Al molar ratio, as it is in the balanced thermite reaction. Finally, a 2.4 mL allotment of PO, TMO, or DMO was added to the solution and stirred, inducing gelation. The time to gelation for the syntheses was monitored and recorded. The as-synthesized wet gels were covered and allowed to age for 24 hours. Then the gels were dried in an oven at 60°C for 7 days which resulted in evaporation of solvents and densification of the samples to form xerogels.

In addition to a 1:1 stoichiometric ratio of Fe:nano Al, other energetic systems were synthesized following an analogous procedure. In all cases, 1.30 g $Fe(NO_3)_3 \cdot 9H_2O$

was added to 7.0 mL of ethanol and stirred until the solid ferric nitrate component was completely dissolved in the ethanol. Then additional components were individually added into the sol stage of the synthesis. These components include: a 1:3 Fe:Al ratio of nano Al powder (3x the stoichiometric quantity, 3 x 0.083 g = 0.249 g Al), a 2:1 Fe:Al quantity of nano Al powder (½ the stoichiometric ratio, ½ x 0.083 g = 0.0415 g Al), a 1:1 stoichiometric ratio of Fe:nano Al (0.083 g Al) plus 0.083 g CNT, a 1:1 Fe:Al ratio of micron scale Al powder (0.083 g Al), and a 1:1 Fe:Al ratio of micron Al powder (0.083 g Al) plus 0.083 g CNT. Table 3.1 summarizes the systems prepared.

Table 3.1: Summary of the nanoenergetic systems of iron (III) oxide and aluminum synthesized using sol-gel chemistry from the gelation chemicals propylene oxide (PO), trimethylene oxide (TMO), and 3,3 dimethyloxetane (DMO).

Sample	
Fe_2O_3(PO)/1:1 nano Al	**Fe_2O_3(DMO)/3x nano Al**
Fe_2O_3(PO)/3x nano Al	**Fe_2O_3(DMO)/0.5x nano Al**
Fe_2O_3(PO)/0.5x nano Al	**Fe_2O_3(DMO)/1:1 nano Al CNT**
Fe_2O_3(PO)/1:1 nano Al CNT	**Fe_2O_3(DMO)/1:1 micron Al**
Fe_2O_3(PO)/1:1 micron Al	**Fe_2O_3(DMO)/1:1 micron Al CNT**
Fe_2O_3(PO)/1:1 micron Al CNT	
Fe_2O_3(TMO)/1:1 nano Al	
Fe_2O_3(TMO)/3x nano Al	
Fe_2O_3(TMO)/0.5x nano Al	
Fe_2O_3(TMO)/1:1 micron Al	
Fe_2O_3(TMO)/1:1 nano Al CNT	
Fe_2O_3(TMO)/1:1 micron Al CNT	
Fe_2O_3(DMO)/1:1 nano Al	

3.5 RuO_2/Al nanoenergetic materials systems

3.5.1 Synthesis of hydrous RuO_2 xerogels

Syntheses were performed in a 20 mL glass scintillation vial and performed under ambient conditions. The synthesis was performed by adding 0.42 g (1.6 mmol) $RuCl_3 \cdot xH_2O$ to 3.5 mL of ethanol and stirring until the powdered ruthenium chloride component was completely dissolved in the ethanol. (1.6 mmol was calculated by using the exact formula of the Ru precursor, $RuCl_{3.37} \cdot 2.5H_2O$, having a molecular weight of 265.6 g/mol, which was obtained after performing elemental analysis on the as-purchased $RuCl_3 \cdot xH_2O$ salt). Then a 1.2 mL allotment of the weak base, propylene oxide, was added as the gelation chemical to the solution and stirred. After addition of the gelation chemical, the time to gelation was monitored and recorded. After gelation occurred, the gel was covered and allowed to age for 24 hours. Then the aged gel was allowed to dry in a fume hood under ambient conditions to allow solvents to evaporate.

3.5.2 Synthesis of RuO_2/Al energetic systems

Syntheses were performed in 20 mL glass scintillation vials and performed under ambient conditions. Four identical syntheses were performed by adding 0.42 g (~1.6 mmol) $RuCl_3 \cdot xH_2O$ to 3.5 mL of ethanol and stirring until the powdered ruthenium chloride component was completely dissolved in the ethanol. To each individual vial a specific quantity of Al powder was added: 0.083 g, 0.065 g, 0.028 g, and no Al. Then a 1.2 mL allotment of weak base, propylene oxide, was added as the gelation chemical to each solution and stirred. After addition of the gelation chemical, the time to gelation

was monitored and recorded. After gelation occurred, the gels were covered and allowed to age for 24 hours, at which point they were dried in atmospheric conditions or heated at 60°C for seven days to remove residual solvents.

3.6 Characterization Methods

3.6.1 Transmission electron microscopy (TEM)

High-resolution transmission electron microscopy (HRTEM) images were obtained from a Hitachi HF 2000 FE TEM with an accelerating voltage of 200.0 keV. The powder samples were suspended in an ethanol solution into which a copper grid was submerged. The submerged copper grid caught the suspended particles at which point the grid was removed from the solution. After evaporation of the ethanol solvent, the samples could be imaged by TEM. TEM was used to image the morphology of metal oxide matrices and its contact with the aluminum particles. TEM is an imaging technique where a beam of electrons is diffracted by a sample and the diffracted electrons show a two-dimensional image of the sample. TEM requires thin samples for imaging. As much of the sample powder was too thick to be imaged, images were always taken at the edge of the samples.

3.6.2 Infrared Spectroscopy (IR)

IR spectra were taken of the synthesized solid xerogels through the use of a Nujol mull in which a small amount of a powder sample is mixed with the Nujol. The sample mull was pipetted between two KBr windows which possessed a diameter of 25 mm and a thickness of 2 mm. A Nicolet Nexus 870 Spectrophotometer scanned the range from

400 – 4000 cm^{-1} with a resolution of 2 cm^{-1} and a data spacing of 0.964 cm^{-1}. Fifty scans per sample were taken. The resulting spectra were further refined by the subtraction of the pure Nujol spectrum, taken under the same conditions, without scaling (scaling factor = 1). The sample chamber was thoroughly purged with dry, CO_2-free air prior to measurements in order to avoid the superposition of strong water and/or carbon dioxide bands onto the spectrum of interest. IR spectroscopy is a spectroscopic technique used to identify functional groups within a sample where infrared light of different frequencies is beamed through a sample and to a detector. The detector measures the absorption of the original infrared radiation by the sample as a function of frequency, or wavenumber. Sample characterization is possible as specific chemical bonds will absorb in varying intensities and at varying frequencies.

3.6.3 Thermal Analysis

Differential thermal analysis was performed on a Perkin Elmer DTA 7 Differential Thermal Analyzer (DTA). Powder samples of the synthesized materials were heated at a constant ramp of 10°C/min in alumina crucibles. Air and ultra-high purity argon were used as purge gases at a flow rate of 20.00 mL/min. High temperature DTA/TGA data (to 1400°C) was determined using a Netzsch STA 449-Jupiter TGA-DTA. Again, powder samples were placed in alumina crucibles and heated at 10°C/min in both air and argon atmospheres up to 1400°C. Thermal analysis was a critical technique utilized in this study. It was used to quantify the heats of reaction for the exothermic reactions. Also, thermal transformations are able to be reasoned based on the type of transformation, either exothermic or endothermic. Thermogravimetric analysis

(TGA) is a thermal characterization method which determines weight change as a function of temperature. TGA measurements can determine materials properties such as thermal degradation temperatures and the level of organic species within a sample.

3.6.4 Surface area analysis

Surface area analysis was performed using a Quantachrome Instruments Autosorb-1 surface area analyzer. Powder samples of non-alumninum containing iron (III) oxide xerogels were degassed at 130°C for 24 hours under vacuum using nitrogen as the adsorbate. BET theory was employed to determine surface area. Surface area analysis is based on the theory of the adsorption of gas molecules on the surface of a solid sample. Here, the technique was employed to determine the specific surface areas of the synthesized metal oxide matrices in order to infer the amount of surface area available for the particulate aluminum particles to contact the metal oxide matrix.

3.6.5 X-ray photoelectron spectroscopy (XPS)

XPS scans of powder samples were taken using a Surface Science Laboratories SSX-100 ESCA Spectrometer using monochromatic Al K-α radiation (1486.6 eV). The system operated at a pass energy of 50 eV. Powder samples were housed in aluminum foil during analysis and a flood gun was used at a voltage of 3 eV. The operating pressure of the vacuum chamber was less than 3×10^{-8} Torr. General scans covered the binding energy range of 0-1,100 eV. High resolution C(1s) and/or C(1s)/Ru(3d) scans were run with a central binding energy (CBE) of 285 eV with a window width of 20 eV at a spot size of 400 μm. High resolution scans were run on the Fe(2p) region with a

CBE of 715 eV, a window width of 30 eV at a spot size of 400 μm. High resolution O(1s) scans were run at a CBE of 532 eV using a spot size of 400 μm and a window width of 20 eV. High resolution N(1s) scans were run at a CBE of 400 eV using a spot size of 400 μm and a window width of 20 eV. Each high resolution scan possessed a 0.1 eV per step interval. Curve fitting of the data was accomplished using the program Spectral Data Processor, Version 4.1. XPS is used to determine elemental composition and oxidation state of samples. For example, a shift in the peak position to higher binding energies from the elemental state results in samples of higher oxidation states. Also, during deconvolution of peaks, more electronegative bonds are located at higher binding energies.

3.6.6 X-ray diffraction (XRD)

X-ray diffraction of the samples was performed on a Philips PW 1800 X-Ray Diffractometer. Patterns from 15° to 80° were examined with a step size of 0.02° using monochromatic CuKα x-rays with a wavelength of 1.54056 Å. Powder samples were analyzed using a zero background sample holder. X-ray diffraction is able to determine lattice structures and identify phases present in a sample as a result of the diffraction of x-rays in a crystalline material. XRD was used as a technique to verify phases present in the sample before and after possible energetic reactions.

3.6.7 Elemental analysis

Elemental analysis of the material was performed by Atlantic Microlabs, Norcross, GA. Quantitative values of carbon, hydrogen, oxygen, nitrogen, and/or

chlorine were determined through experimental measures, including: combustion and pyrolysis of the samples. The balance of the compositional make-up of the sample was assigned as iron or ruthenium. Elemental analysis is able to determine the elemental composition of a sample on a weight percent percent basis. The technique was utilized here to determine precise compositional make-ups of the hydrated iron and, particularly, ruthenium salts.

3.6.8 Atomic force microscopy (AFM)

Atomic force microscopy (AFM) images were taken using a Pacific Nanotechnology Nano-R AFM. Synthesized monoliths of the materials were placed on the surface of a wet epoxy and the epoxy was allowed to dry. Therefore, the sample was embedded within the epoxy but left with an appreciable amount of the sample above the upper level of the epoxy, allowing access of the AFM probe to freely contact the sample surface. The sample was scanned using a scan size of 0.76 μm x 0.76 μm at a scan rate of 1 Hz and a resolution of 512 scan lines. The AFM probes used possess a radius of less than 10 nm with a force constant of 42 N/m. This imaging technique uses a tipped cantilever which scans the surface of the sample and determines the surface morphology of a sample based on the deflection of the cantilever.

CHAPTER 4

ELUCIDATION OF 'PROTON SCAVENGING' MECHANISM

4.1 Overview

This chapter discusses the elucidation of the sol-gel mechanism by which weak base molecules are added to a hydrated iron salt solution to induce gelation. Section 4.2 describes the results of the syntheses using weak base molecules propylene oxide (PO), tetrahydrofuran (THF), and pyridine as gelation chemicals. Section 4.3 outlines the proposed mechanisms for the weak base gelation chemicals studied based on presented data. In conclusion, Section 4.4 summarizes the work on the elucidation of the 'proton scavenging' mechanism using weak base molecules as gelation chemicals.

4.2 Iron (III) oxide xerogels synthesized from weak base molecules

4.2.1 Results of (III) oxide xerogels synthesized from weak base molecules

The addition of propylene oxide to a hydrated iron (III) nitrate metal salt precursor solution results in a heat-releasing reaction with the formation of a reddish-brown monolithic wet gel within 3 minutes. A porous xerogel iron oxide matrix forms after the solvent in the gel is allowed to evaporate in ambient conditions. The addition of pyridine to an equivalent hydrated iron nitrate solution results in the formation of a dark-brown material after 10 days. Ambient drying of the material for an excess of two weeks yields a dry xerogel. The addition of tetrahydrofuran to the same iron nitrate solution results in the formation of a gel in 7 days. Ambient drying of the wet gel for an excess of

two weeks yields a dry xerogel. Figure 4.1 displays x-ray diffraction data for the as-synthesized samples. Due to their largely amorphous character, as well as the fact that diffraction peaks tend to broaden in the nano-scale, the iron oxide materials should be analyzed in a more qualitative manner. As a reference, Figure 4.1(d) shows the diffraction patterns for different iron (III) oxide, hydroxide, and oxyhydroxide phases: γ-Fe_2O_3; $Fe(OH)_3$; FeO(OH), ferrihydrite; α-Fe_2O_3; α-FeO(OH); and β-FeO(OH). The most intense peaks from many of these iron (III) phases fall within the two broad bands of the diffraction patterns in Figure 4.1(a)–4.1(c). Therefore, it would not be unreasonable to describe the materials with the empirical formula of $Fe^{(III)}_xO_yH_z$. For the sake of simplicity, the term "iron (III) oxide" will be used to denote the formation of the mixture of iron (III) compounds that constitute the xerogel material. However, while definitive identification of the iron species present in the samples is impossible, the XRD data gives clear indication as to the nanocrystalline nature of the samples.

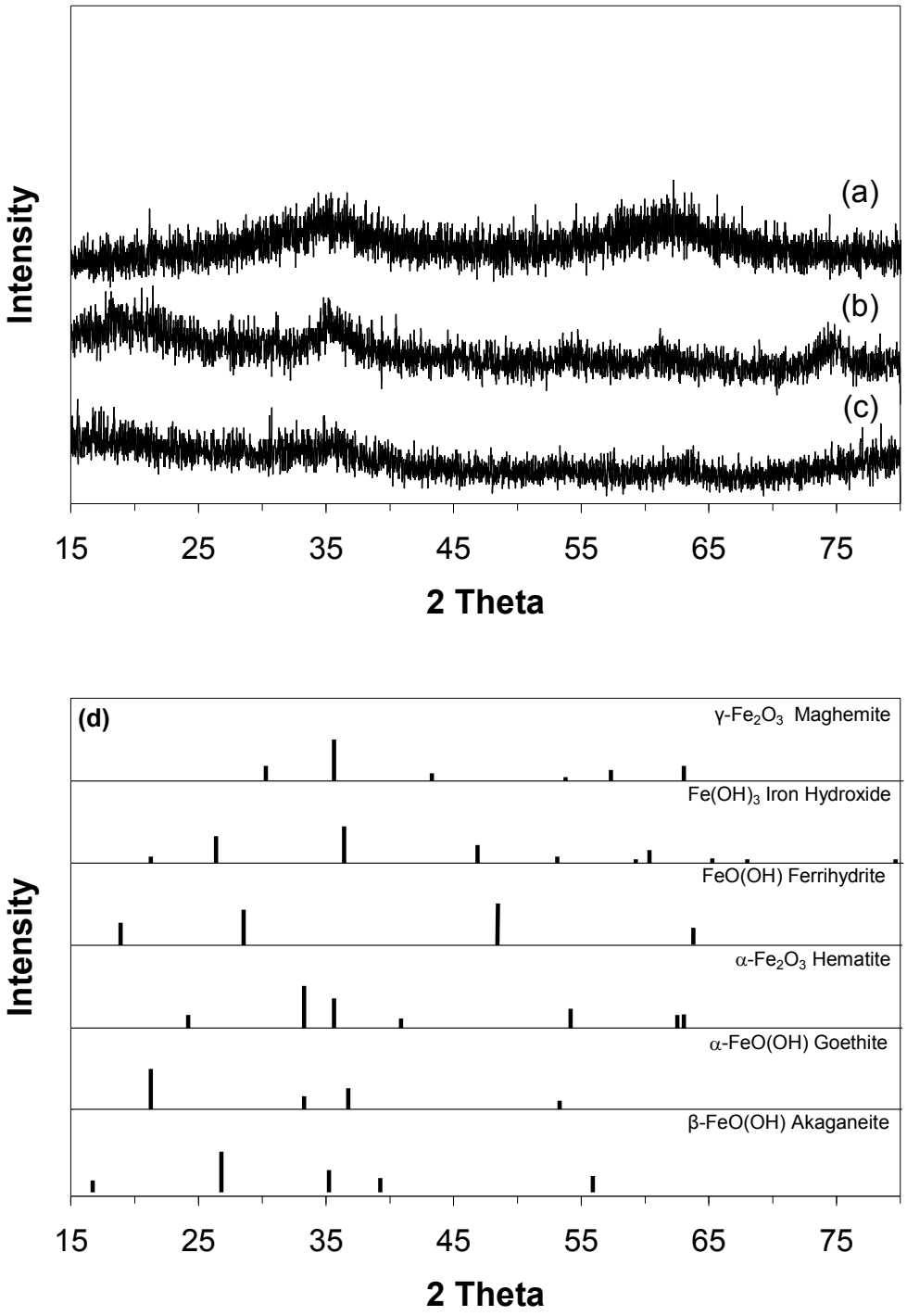

Figure 4.1: X-ray diffraction patterns for the $Fe^{(III)}_xO_yH_z$ xerogel formed with (a) PO, (b) pyridine, and (c) THF and (d) x-ray diffraction patterns for various iron oxide/oxyhydroxide phases: γ-Fe_2O_3, $Fe(OH)_3$, FeO(OH), ferrihydrite, α-Fe_2O_3, α-FeO(OH), and β-FeO(OH).

Figures 4.2(a) and 4.2(b) show TEM and AFM images of the structure of the PO-synthesized material having closely-packed particles of 2-5 nm with clusters on the order of 25-40 nm. Figure 4.2(c) images the $Fe^{(III)}_xO_yH_z$ material synthesized from pyridine showing a porous morphology with individual, interconnected $Fe^{(III)}_xO_yH_z$ clusters on the order of 40-50 nm with individual particles of approximately 10 nm. Figure 4.2(d) shows TEM image revealing a porous structure with $Fe^{(III)}_xO_yH_z$ particles of approximately 5 nm forming clusters of 25 nm when THF is used as the gelation chemical.

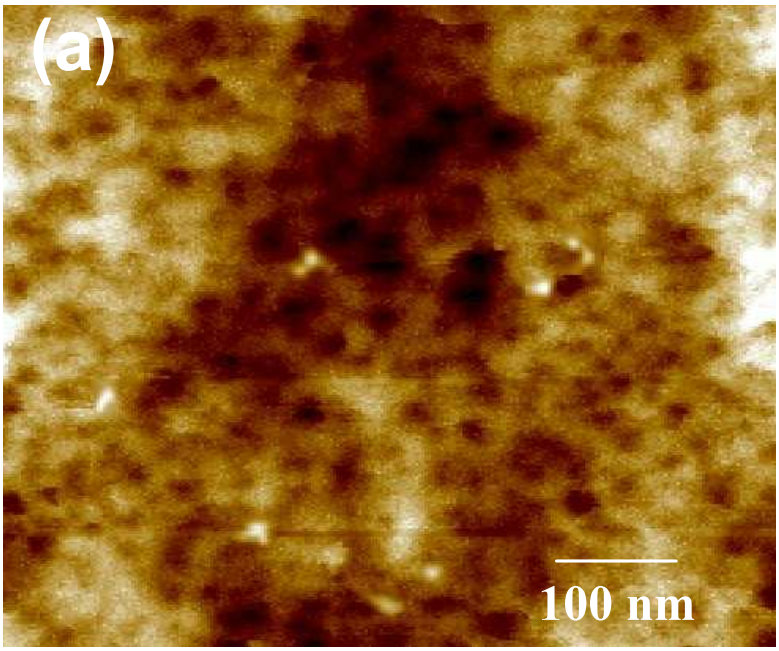

Figure 4.2: Imaging by AFM and TEM of the $Fe^{(III)}_xO_yH_z$ xerogel formed with (a) and (b) PO, (c) pyridine, and (d) THF.

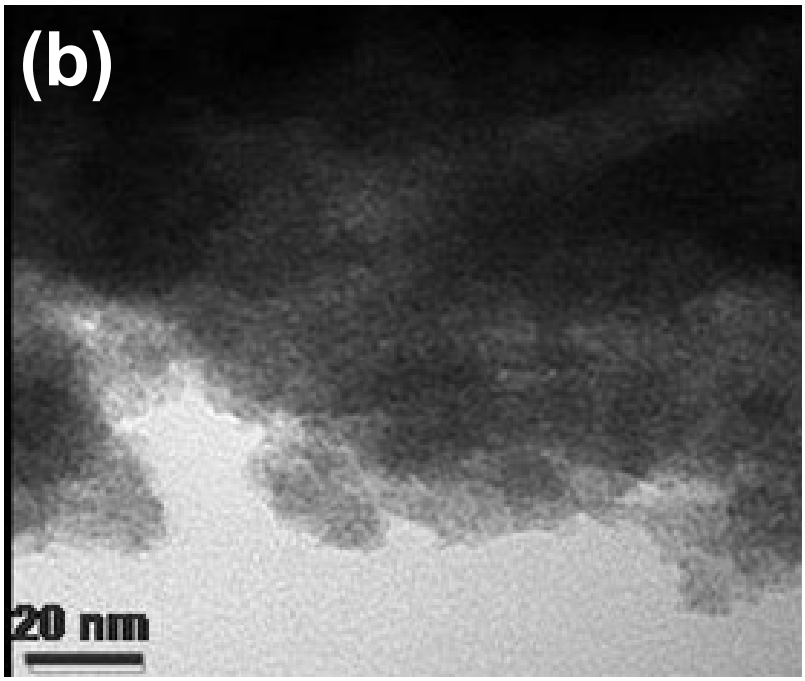

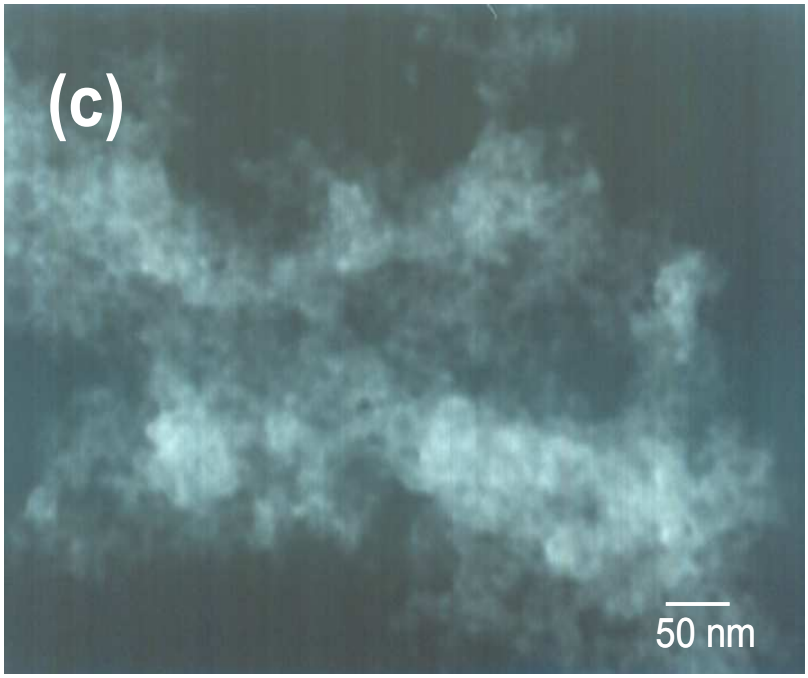

Figure 4.2 continued

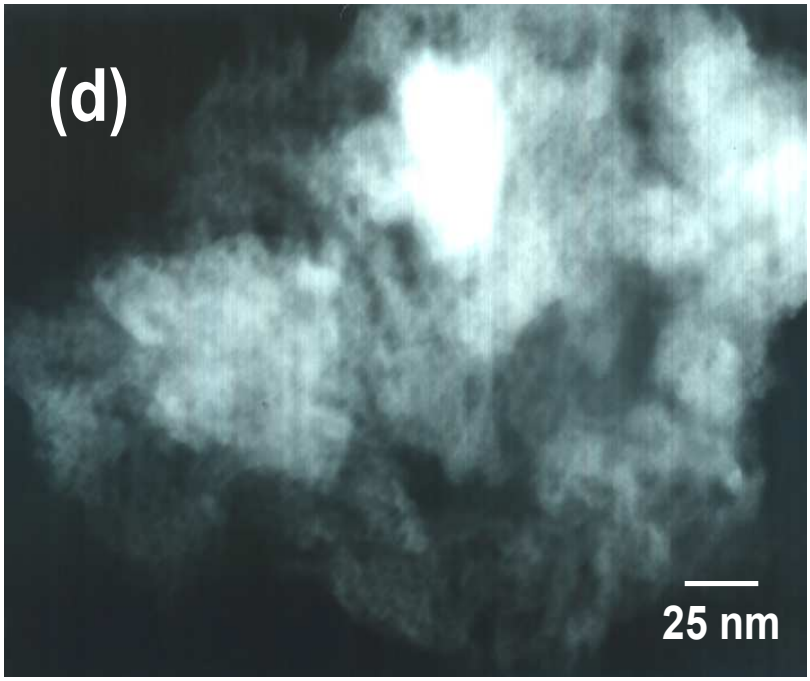

Figure 4.2 continued

4.2.2 XPS characterization of iron (III) oxide synthesized from propylene oxide

X-ray photoelectron spectroscopy was utilized to evaluate the composition of the surface of the iron (III) oxide-based material synthesized from the weak base propylene oxide. Figure 4.3(a) shows the general survey spectrum of the material. Further analysis of the XPS spectrum was performed by high-resolution scans of the C(1s), Fe(2p), and O(1s) regions. Figure 4.3(b) shows the high-resolution C(1s) region after the data was adjusted to a C(1s) peak at 285.0 eV, as a result of differential charging of the insulating material shifting photoelectron lines to higher binding energies.[86] The C(1s) region can be deconvoluted into 2 separate peaks: (1) at a binding energy (BE) of 285.0 eV corresponding to aliphatic C–C bonding arising from the diol in Equation 4 as well as residual ethanol and (2) the more electronegative C–O bond at a higher binding energy of 288.1 eV from the same diol. To support the statement that the sample contains residual

organics, elemental analysis of the material was performed. The results show the sample to possess 29.3% carbon, showing that more one-quarter of the sample by weight is carbon-based. Important to note is the absence of an epoxide peak within the C(1s) high resolution scan. This is due to the fact that propylene oxide is a key component in the reaction and unlike a traditional catalyst, it actually gets consumed in the reaction.[39] The sample Fe($2p_{3/2}$) peak is located at a binding energy of 711.4 eV and the Fe($2p_{1/2}$) peak is located at a BE of 725.8 eV, as shown in Figures 4.3(c) and 4.3(d). The corresponding Fe($2p_{3/2}$) and Fe($2p_{1/2}$) binding energy peaks of elemental iron are 710 eV and 723 eV, respectively. It is known that non-equivalent atoms of the same element in a solid give rise to peaks with different BE with increasing BE for increasing oxidation state.[87] This is demonstrated by the experimental values, and, along with the published values of the Fe($2p_{3/2}$) peak for α-Fe_2O_3 corresponding to a BE of 711.6 eV and for FeO(OH) at a BE of 711.5 eV[88] and the corresponding Fe_2O_3 Fe($2p_{1/2}$) peak at a BE of 725.1, it can be concluded that the Fe($2p_{1/2}$) and Fe($2p_{3/2}$) peaks correspond to Fe(III).[89]

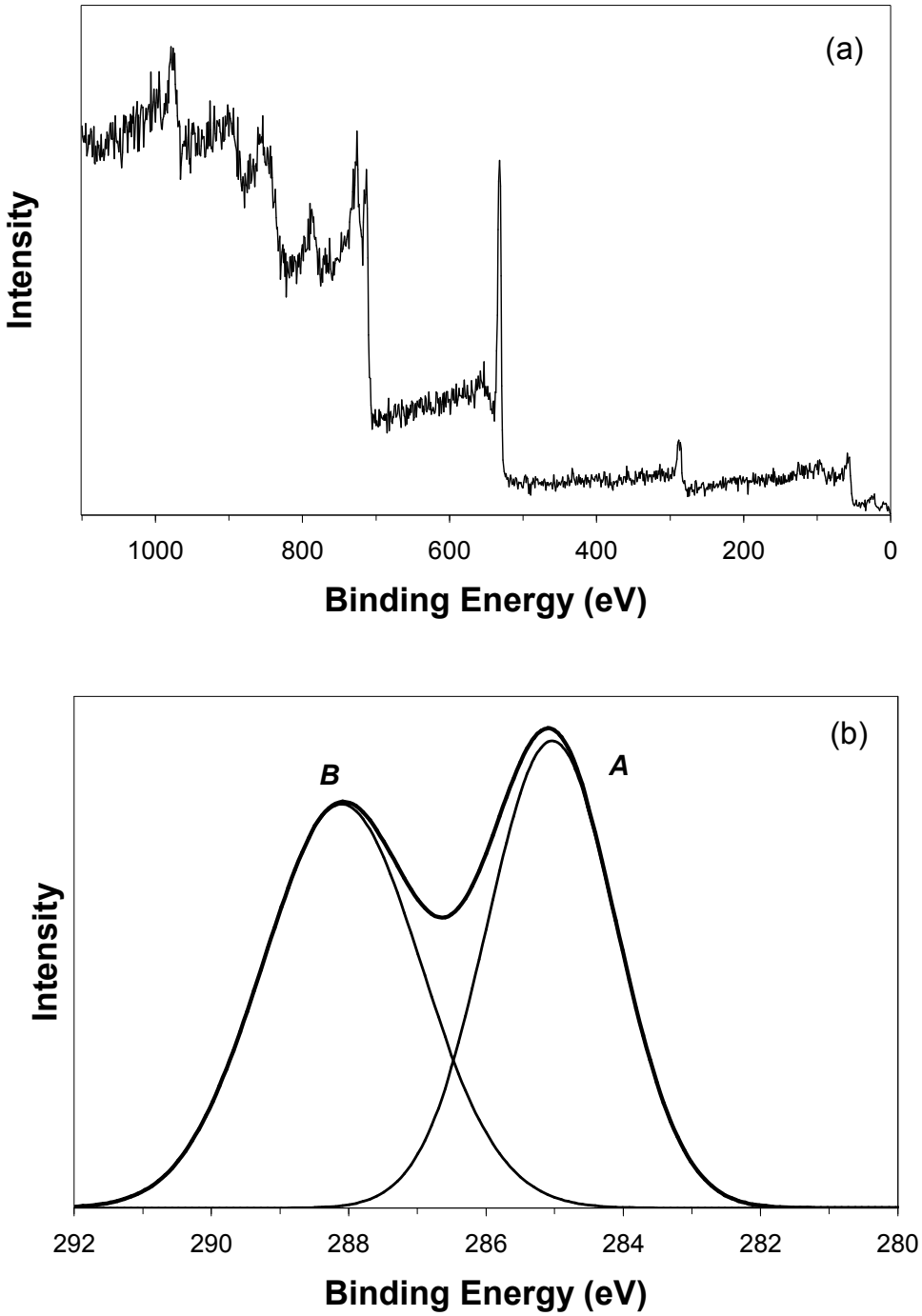

Figure 4.3: The photoemission spectra of a sol-gel synthesized iron (III) oxide/hydroxide from the weak base propylene oxide. (a) The general scan of the oxide material. (b) The high resolution C 1s core level electrons and its deconvolution into three peaks. (c) The Fe $2p_{3/2}$ scan of the material, note the increase in binding energy of the peak from that of elemental iron, corresponding to an oxide material. (d) The Fe $2p_{1/2}$ scan of the material, again a higher binding energy peak in relation to that of elemental iron. (e) The O 1s core level emission spectrum.

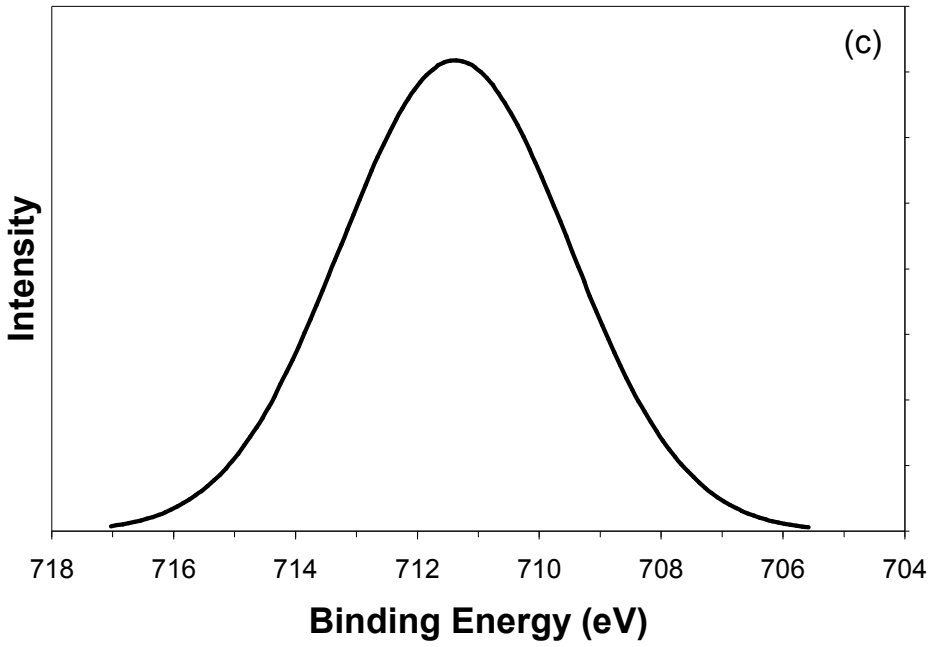

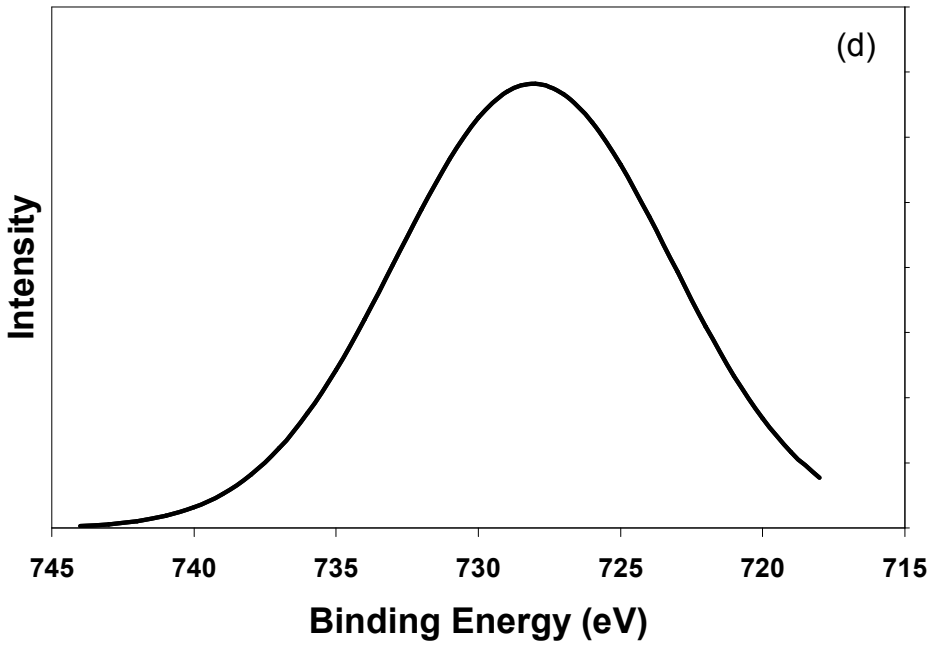

Figure 4.3 continued

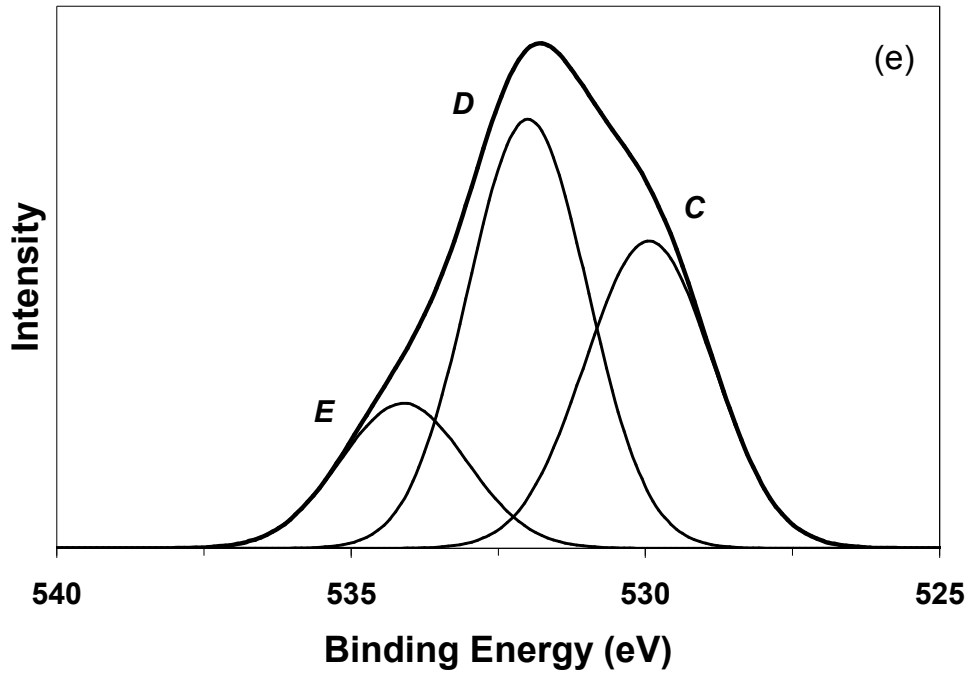

Figure 4.3 continued

Table 4.1: The binding energies, full-width half-maximum values, percentage of total peak area, and assignment of atoms of the x-ray photoemission spectrum (XPS) of the O(1s) and C(1s) core electron regions for a sol-gel synthesized iron (III) oxide/hydroxide from propylene oxide corresponding to Figure 4.3.

Peak Label	BE (eV)	FWHM (eV)	% of Total Area	Assignment of Atoms
		C 1s		
A	285.0	2.26	50.7%	aliphatic
B	288.1	2.20	49.3%	**C**-O
		O 1s		
C	529.9	2.55	36.1%	$Fe_2\mathbf{O}_3$
D	531.9	2.38	47.1%	FeO(**O**H)
E	532.0	2.51	16.8%	**O**-C

The O(1s) region can be deconvoluted into three peaks: 529.9 eV corresponding to the oxygen within α-Fe_2O_3; 531.9 eV corresponding to the oxygen within the iron hydroxyl compound FeO(OH), a product of the reaction of Fe_2O_3 with water as well as an intermediate in the proposed propylene oxide 'proton scavenging' mechanism; and 534.0 eV corresponding to the oxygen-carbon bonding of the residual organic diol species from the synthesis as well as residual ethanol.[90] The relative ratios between the three experimental O(1s) peaks corresponding to Fe_2O_3, FeO(OH), and O–C are 37.1:47.1:16.8, respectively. This indicates that the majority of the synthesized product (~84.2%) is an iron oxide or iron hydroxide material, with the balance of the sample oxygen originating from residual organic species. The reported O(1s) peak location for α-Fe_2O_3 is 529.9 eV, which is the value reported in the synthesized material here,

whereas the O(1s) peak of elemental oxygen is centered at 532.0 eV, again proving the existence of an iron (III) material,[89] supporting an empirical formula of $Fe^{(III)}_xO_yH_z$. The O(1s) region is shown in Figure 4.3(e). The XPS data for propylene oxide as the gelation agent is summarized in Table 4.1.

4.2.3 XPS characterization of iron (III) oxide synthesized from pyridine

The survey XPS spectrum of the newly synthesized material in Figure 4.4(a) clearly shows the C(1s), O(1s), Fe($2p_{3/2}$), Fe($2p_{1/2}$) and N(1s) peaks. High resolution scans of the C(1s) peak, seen in Figure 4.4(b), show the deconvolution of five distinct peaks. The peak at 285.0 eV corresponds to the double-bonded carbon within the pyridine molecule, 286.5 eV corresponds to the remaining aliphatic bonds arising from the ethanol solvent as well as single-bonded carbon-carbon bonds remaining from the pyridine molecule, 287.7 eV corresponds to the C–N=C bond of the pyridine molecule, 289.0 eV corresponds to the $C–N^+=C$ bond, which arises from the possible protonation of the pyridine molecule during the sol to gel reaction, and 290.3 eV corresponds to the C–OH alcohol bonding of residual ethanol. The proposed $C–N^+=$ bond as well as examination of the N(1s) peak will be discussed within the section on pH studies of gel formation. High resolution scans of the Fe($2p_{3/2}$) and Fe($2p_{1/2}$) peaks are shown in Figure 4.4(c) and 4.4(d). The Fe($2p_{3/2}$) peak appears at a binding energy of 711.1 eV and the Fe($2p_{1/2}$) peak appears at a BE of 725.1 eV. This gives a Fe($2p_{1/2}$) to Fe($2p_{3/2}$) peak maximum to peak maximum difference of 14.0 eV, significantly larger than the same peak-to-peak difference for elemental Fe of 13.2 eV and similar to that of Fe_2O_3, which has a similar reported difference of 13.6 eV.[91] As with the sample synthesized from the

addition of propylene oxide, the material obtained from the addition of pyridine as the gelation agent exhibits a chemical shift to higher binding energies for the Fe(2p) peaks which is indicative of the formation of an iron (III) oxide/hydroxide material.

High resolution scans of the O(1s) peak are shown in Figure 4.4(e). The peak can be deconvoluted into three distinct peaks: 530.1 eV corresponding to the oxygen within the iron (III) oxide material, 532.5 eV corresponding to the oxygen within the iron hydroxyl compound FeO(OH), a product of the reaction of Fe_2O_3 with water, and 534.8 eV corresponding to the O–C corresponding to the oxygen bonding within residual organic species from the ethanol.[25] The relative peak ratios for the oxygen corresponding to Fe_2O_3, FeO(OH), and O–C are 51.5:35.9:12.5, respectively. Again, in the case of pyridine being used as the weak base gelation chemical, there is a large (87.5%) presence of iron oxide/hydroxide product in the material with the balance corresponding to residual solvents. The XPS data for pyridine as the gelation agent is summarized in Table 4.2.

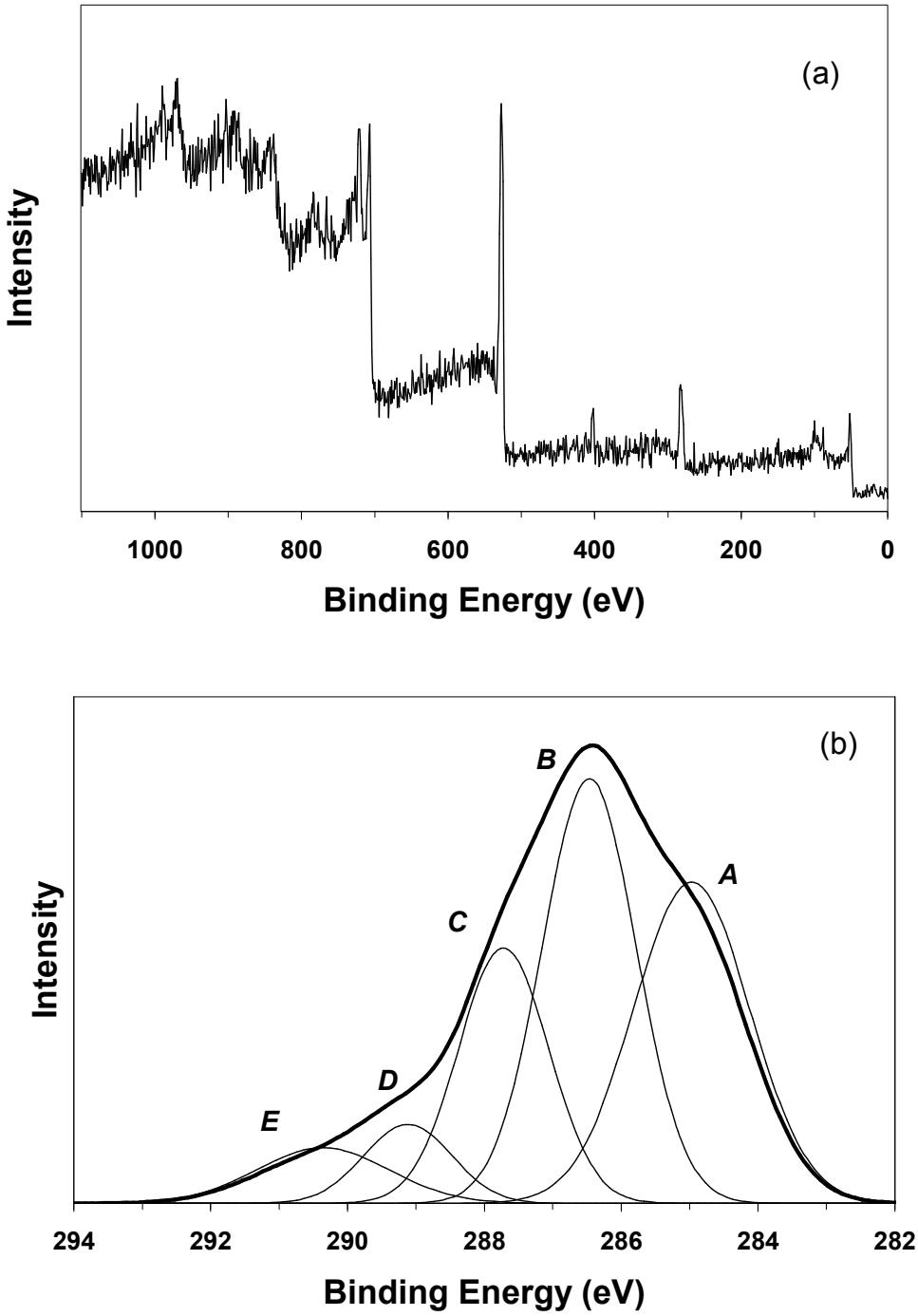

Figure 4.4: The photoemission spectra of a sol-gel synthesized iron (III) oxide/hydroxide from the weak base pyridine. (a) The general scan of the oxide material. (b) The high resolution C 1s core level electrons and its deconvolution into five peaks. (c) The Fe $2p_{3/2}$ scan of the material, note the increase in binding energy of the peak from that of elemental iron, corresponding to an iron (III) oxide material. (d) The Fe $2p_{1/2}$ scan of the material, again a higher binding energy peak in relation to that of elemental iron. (e) The O 1s core level emission spectrum, deconvoluted into three distinct peaks.

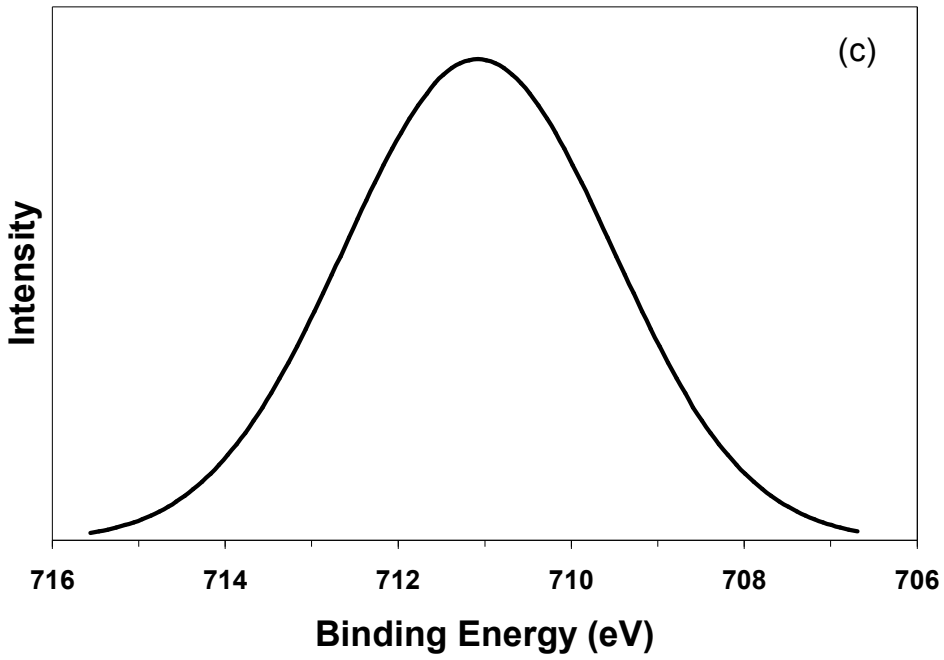

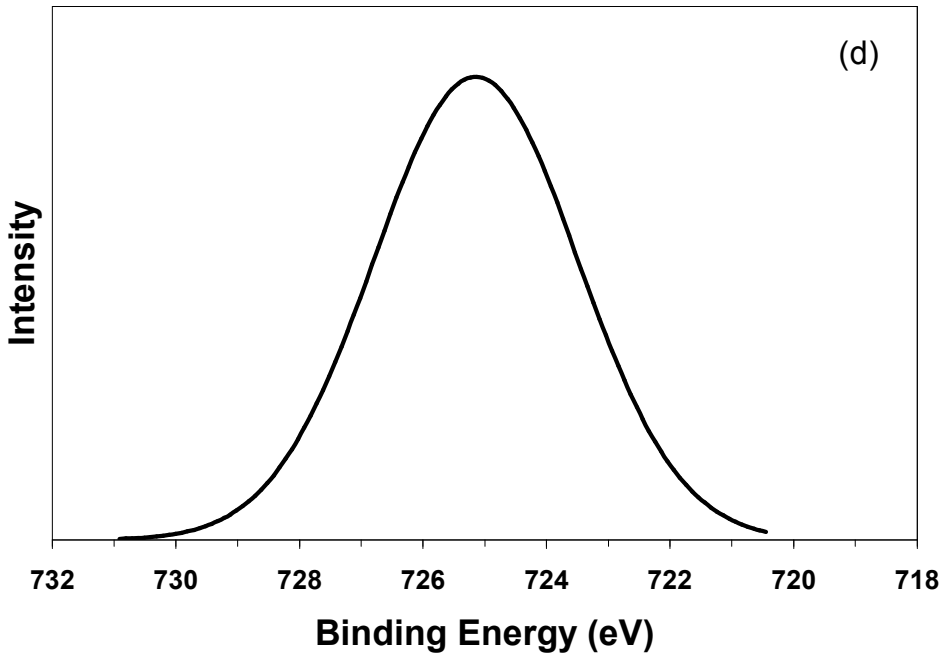

Figure 4.4 continued

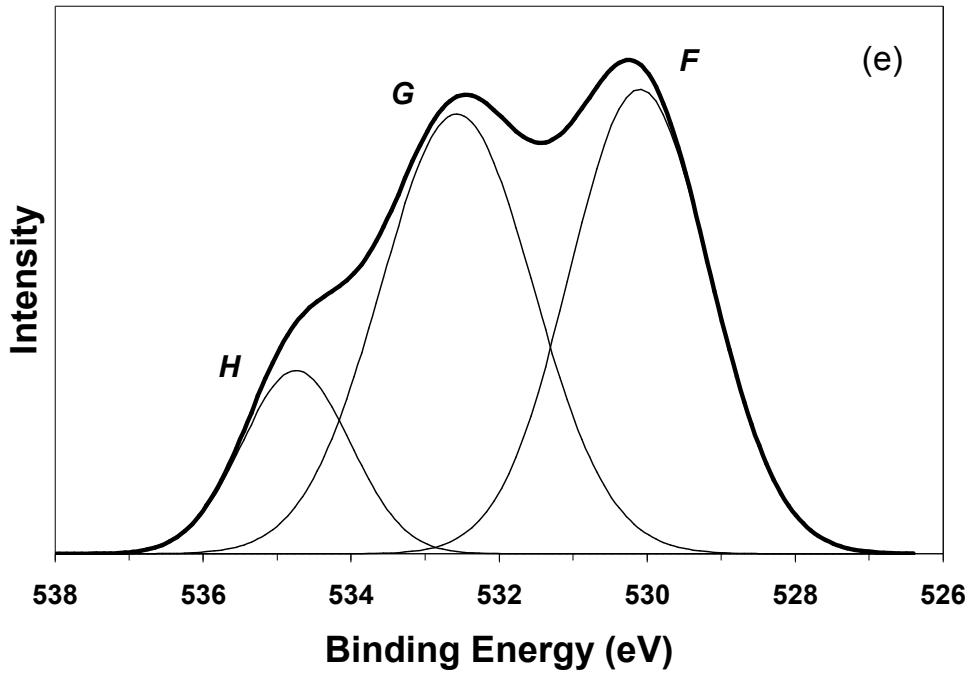

Figure 4.4 continued

Table 4.2: The binding energies, full-width half-maximum values, percentage of total peak area, and assignment of atoms of the x-ray photoemission spectrum (XPS) of the O(1s) and C(1s) core electron regions for a sol-gel synthesized iron (III) oxide/hydroxide from the weak base pyridine corresponding to Figure 4.4.

Peak Label	BE (eV)	FWHM (eV)	% of Total Area	Assignment of Atoms
		C 1s		
A	285.0	1.58	20.9%	**C**=C
B	286.5	1.77	48.1%	**C**-C
C	287.7	1.62	23.6%	**C**-N=C
D	289.0	1.26	5.2%	**C**-N^{+}=C
E	290.3	1.18	2.2%	**C**-O
		O 1s		
F	530.1	2.48	51.5%	Fe_2**O_3**
G	532.5	2.07	35.9%	FeO(**O**H)
H	534.8	1.69	12.5%	**O**-C

4.2.4 XPS characterization of iron (III) oxide synthesized from tetrahydrofuran

An XPS survey spectrum of the material is shown in Figure 4.5(a). Figure 4.5(b) shows the C(1s) high resolution scan can be deconvoluted into 2 peaks. The peak at a BE of 285.0 eV corresponds to the C–C bonding of the residual organic species from the ethanol solvent as well as the aliphatic bonding within the diol product of the reaction mechanism, and the peak at 288.8 can be attributed to the residual C–O bonding from residual ethanol as well as from the diol mechanism product. High resolution Fe($2p_{3/2}$) and Fe($2p_{1/2}$) scans are shown in Figure 4.5(c) and 4.5(d). The Fe($2p_{3/2}$) peak appears at a

BE of 710.7 eV and the Fe($2p_{1/2}$) peak is found at a BE of 724.7, resulting in a peak to peak distance of 14.0 eV. This is similar to the sample synthesized using propylene oxide. From the Fe(2p) peaks, the higher binding energies than elemental Fe confirm the existence of an Fe(III) material. A high resolution O(1s) scan is shown in Figure 4.5(e). The peak at a BE of 529.7 corresponds to the oxygen bonding within Fe_2O_3, the peak at 531.3 eV corresponds to the oxygen within the iron hydroxyl compound FeO(OH), and the peak at 532.5 eV corresponds to the O–C bonding from the residual solvents. The relative peak area ratios of the Fe_2O_3, FeO(OH), and O–C peaks are 44.1:33.5:22.4, respectively. The XPS data for tetrahydrofuran as the gelation agent is summarized in Table 4.3.

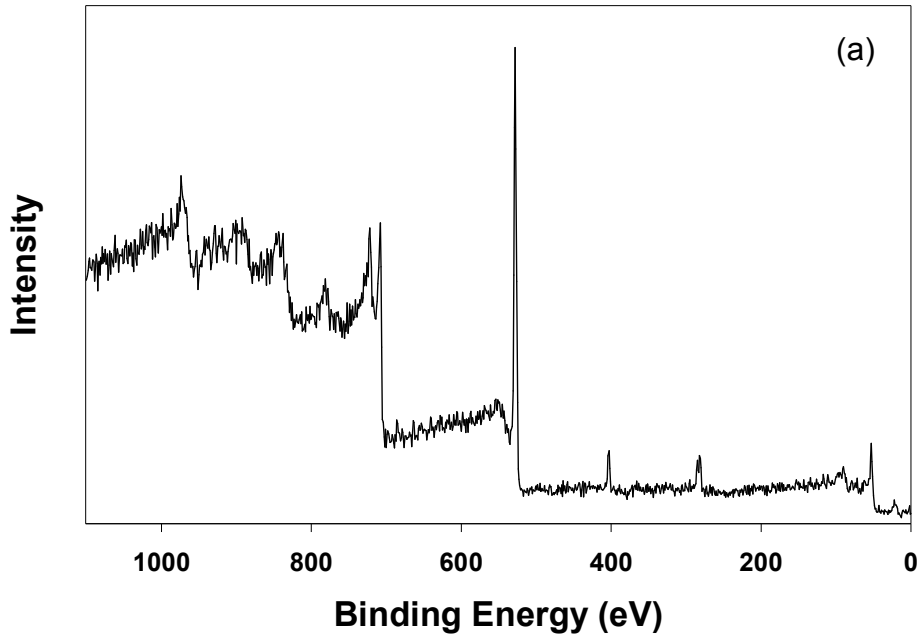

Figure 4.5: The photoemission spectra of a sol-gel synthesized iron (III) oxide/hydroxide from the weak base epoxide, tetrahydrofuran. (a) The general scan of the oxide material. (b) The high resolution C 1s core level electrons and its deconvolution into two peaks. (c) The Fe $2p_{3/2}$ scan of the material, note the increase in binding energy of the peak from that of elemental iron, corresponding to an iron (III) oxide material. (d) The Fe $2p_{1/2}$ scan of the material, also a higher binding energy peak in relation to that of elemental iron. (e) The O 1s core level emission spectrum, deconvoluted into three distinct peaks.

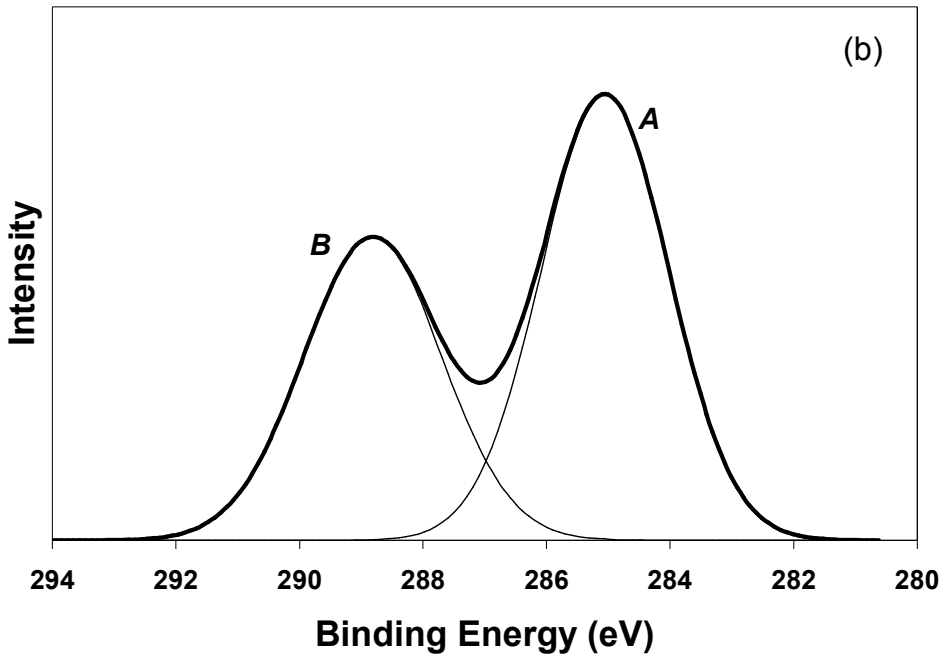

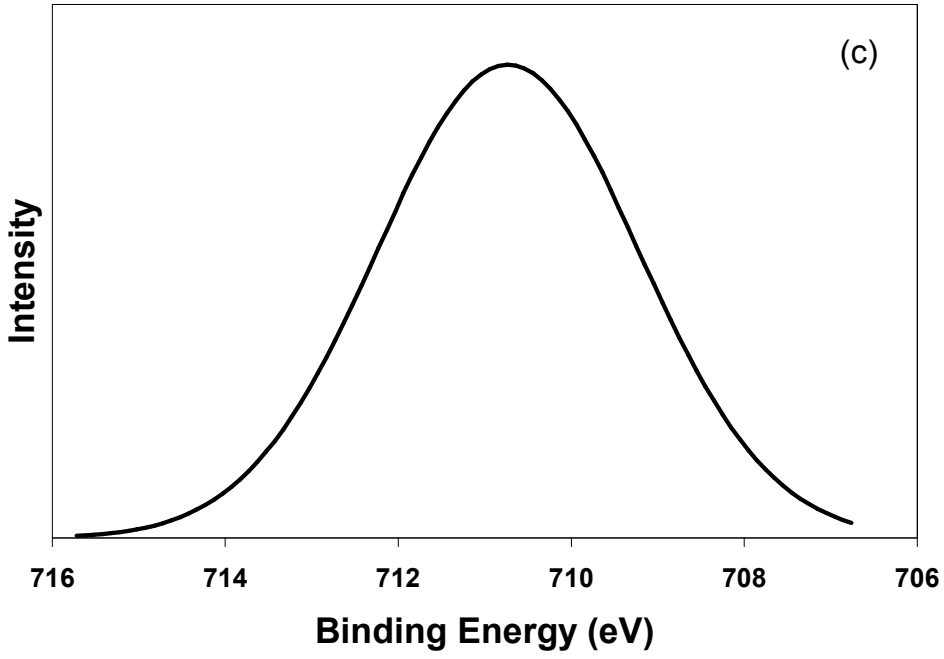

Figure 4.5 continued

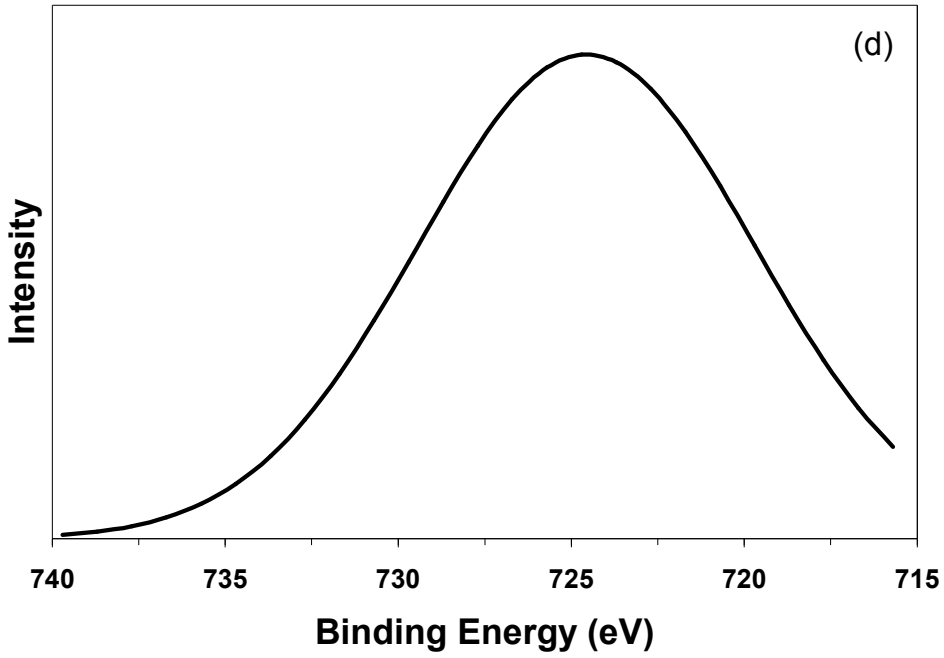

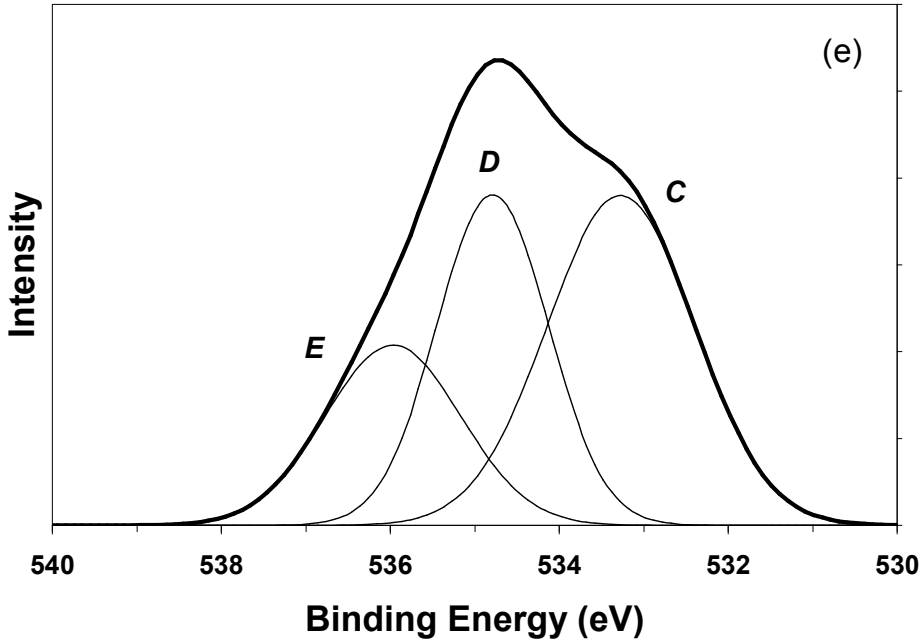

Figure 4.5 continued

Table 4.3: The binding energies, full-width half-maximum values, percentage of total peak area, and assignment of atoms of the x-ray photoemission spectrum (XPS) of the O(1s) and C(1s) core electron regions for a sol-gel synthesized iron (III) oxide/hydroxide from the epoxide tetrahydrofuran corresponding to Figure 4.5.

Peak Label	BE (eV)	FWHM (eV)	% of Total Area	Assignment of Atoms
		C 1s		
A	285.0	2.64	42.4%	aliphatic
B	288.8	2.44	57.6%	**C**-O
		O 1s		
C	529.7	2.05	44.1%	$Fe_2\mathbf{O}_3$
D	531.3	1.55	33.5%	FeO(**O**H)
E	532.5	1.90	22.3%	**O**-C

A general note on all three synthesized samples is that while the majority of the oxygen within the sample originates from an iron oxide or hydroxyl material, drying the samples under ambient conditions permits a substantial percentage of residual organic species to remain in the final material. Given the intended use of these materials in highly exothermic reactions with potential inclusion in projectile casing, residual organic materials in the nanonetwork matrix may prove important in the overall energetic efficiency of the oxidative/reductive process. Table 4.4 summarizes the XPS binding energies of the Fe($2p_{1/2}$), Fe($2p_{3/2}$), and O(1s) photoelectron binding energy peaks for the three samples, showing very similar results for all three gelation systems.

Table 4.4: Summary of binding energies (eV) of the x-ray photoemission spectra (XPS) in formation of $Fe^{III}_xO_yH_z$ xerogels for the three systems presented for $Fe(2p_{3/2})$, $Fe(2p_{1/2})$, and O(1s).

			O 1s		
Sample	**Fe($2p_{3/2}$)**	**Fe($2p_{1/2}$)**	$Fe_2\mathbf{O}_3$	FeO(**O**H)	**O**-C
Propylene Oxide	711.4	725.8	529.9	531.9	532.0
Pyridine	711.1	725.1	530.1	532.5	534.8
THF	710.7	724.7	529.7	531.3	532.5

4.3 Mechanistic studies of gel formation

The pH of the reacting solution using propylene oxide as the gelation agent has been shown to increase with time. This is explained due to the addition of a weak base to an acidic precursor solution and disappearance of the hydronium ions from solution as they recombine with the anions from the original salt (i.e. nitrate ions). In order to study the mechanism of the gelation processes using propylene oxide, pyridine, and tetrahydrofuran as gelation agents, pH data was collected for all three reactions. Figure 4.6 shows the pH profile of the three systems as a function of reaction time. Clearly, there is an increase in reaction pH with time for each of the three systems. This supports the hypothesis shown in Equations 3 and 4, where the weak base reacts with the hydrated metal complex producing a protonated conjugated weak acid molecule resulting in further release of hydronium ions into solution.

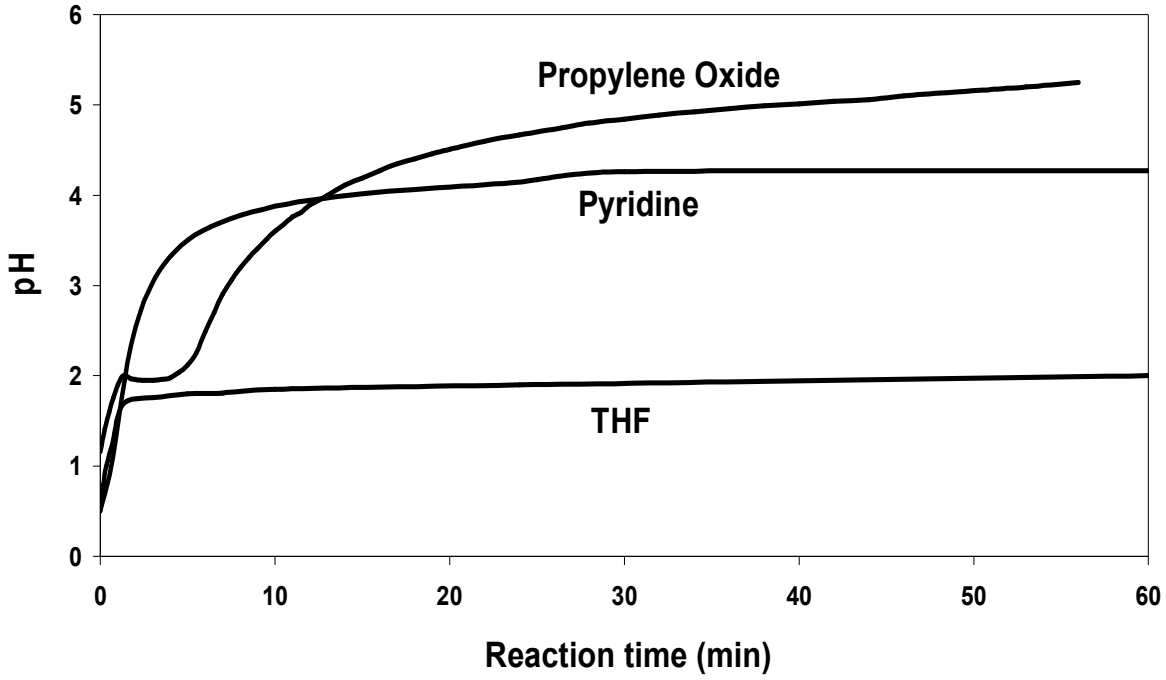

Figure 4.6: pH profile of reaction study of gels formed using propylene oxide, pyridine, and THF as gelation agents. Notice the increase in pH with increasing reaction time for all three systems.

From the pH studies and the previously hypothesized mechanism involving propylene oxide, the following reaction mechanisms are proposed for the sol-gel reactions involving the weak base gelation agents pyridine and tetrahydrofuran. In the case of pyridine as the gelation agent, a pyridine molecule is capable of extracting a proton from the water molecules in the coordination sphere of the hydrated iron cation to form a pyridinium ion, as shown in Equation 5. The 'proton scavenging' cascade will subsequently lead to the formation of Fe_2O_3.

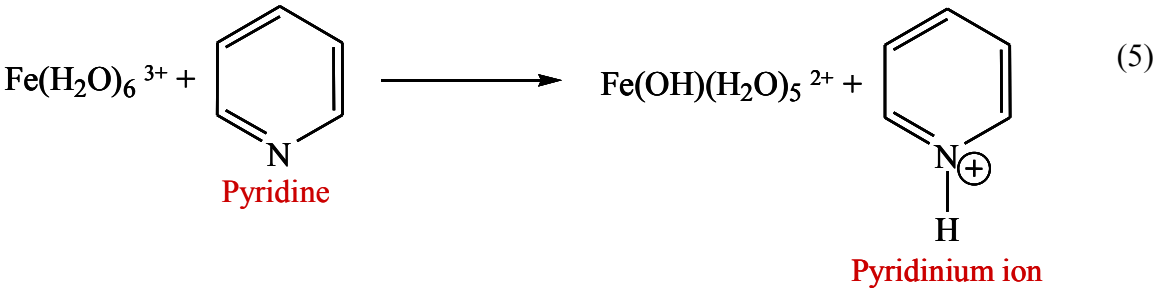

(5)

When propylene oxide is used as the gelation agent, the protonated epoxide undergoes an irreversible ring-opening reaction due to the high strain energy associated with the three-membered ring. In the case of pyridine, the pyridinium ion is a six-membered ring with aromatic character, which is highly stable and has low associated ring strain. Therefore, whereas with the systems involving propylene oxide and THF, XPS results demonstrate the existence of a diol species, which is the result of the ring-opening reaction, the pyridinium ion is relatively stable, especially in the presence of the anionic species present in the system.

Additional evidence of the proposed mechanism in the formation of the pyridinium ion is demonstrated by Fourier-transform infrared spectroscopy (FTIR). Figure 4.7 shows an FTIR spectrum of a $Fe^{(III)}{}_xO_yH_z$ xerogel synthesized using pyridine as the gelation agent. In contrast to pure pyridine, a peak at 3428 cm^{-1} from the gel material corresponds to the asymmetric stretching vibration of the quaternary protonated amine bond present in the pyridinium ion as a result of the proton extraction from the coordinated water molecules.[92] This is echoed by the corresponding symmetric stretching vibration at ~2380 cm^{-1} and the in-plane deformation vibrations of the pyridinium internal modes at ~1630 cm^{-1}.[93-96] It is important to note that the FTIR characterization of the xerogel powder was performed using the Nujol mull sample preparation technique, and hence, the spectrum shown, is a result of the subtraction of

pure Nujol (a heavy paraffin oil with a relatively uncomplicated infrared spectrum, with major peaks between 2950-2800, 1465-1450, and 1380-1370 cm^{-1}) form the raw spectrum of the sample. This ensured that the spectrum of the pyridinium moiety could be presented without being obscured by the Nujol reference.

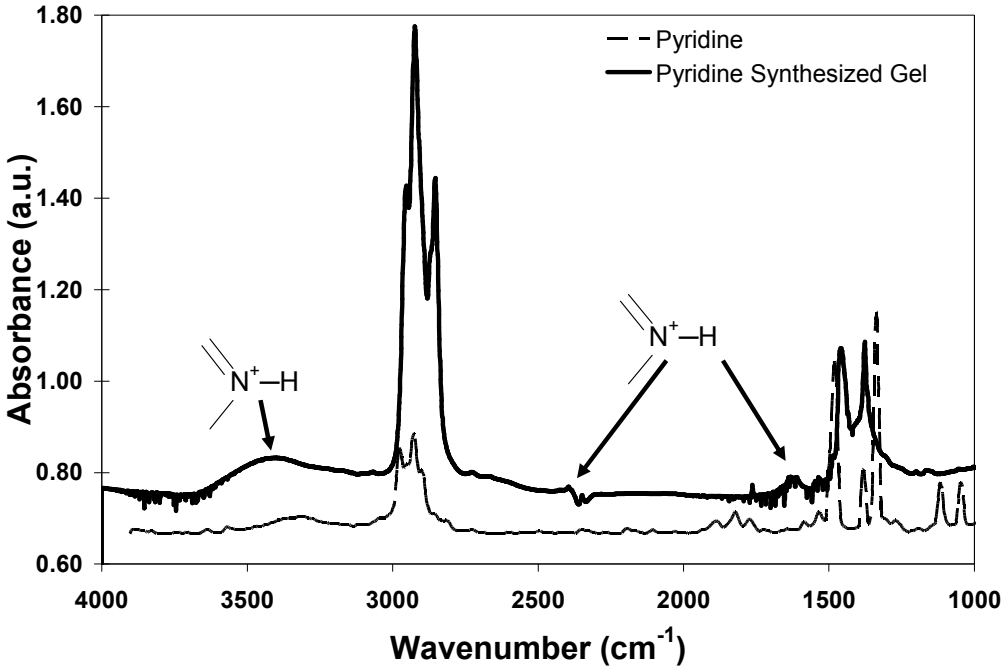

Figure 4.7: IR spectra displaying presence of N^{+}─H bond at 3428, 2380, and 1630 cm^{-1} involved in the mechanism of formation of iron oxide xerogel from pyridine as the gelation agent.

Further evidence of this proposed mechanism and the existence of the pyridinium ion is seen in the high resolution XPS scans of the N(1s) region of the material synthesized in the presence of the pyridine as the gelation agent, shown in Figure 4.8. Three peaks are deconvoluted from the high resolution spectrum: One peak at 399.0 eV corresponding to the C–N=C bonding arising from the aromatic pyridine molecule, a second peak at 403.9 eV corresponding to the C–N^{+}=C aromatic bonding representative of the pyridinium ion, as protonated forms of N atoms in pyridine are shifted to higher

binding energies,[97] and a third peak at 405.9 eV, corresponding to the N–O bond originating from the remaining nitrate anions originating in the initial iron nitrate precursor. Table 4.5 summarizes this data.

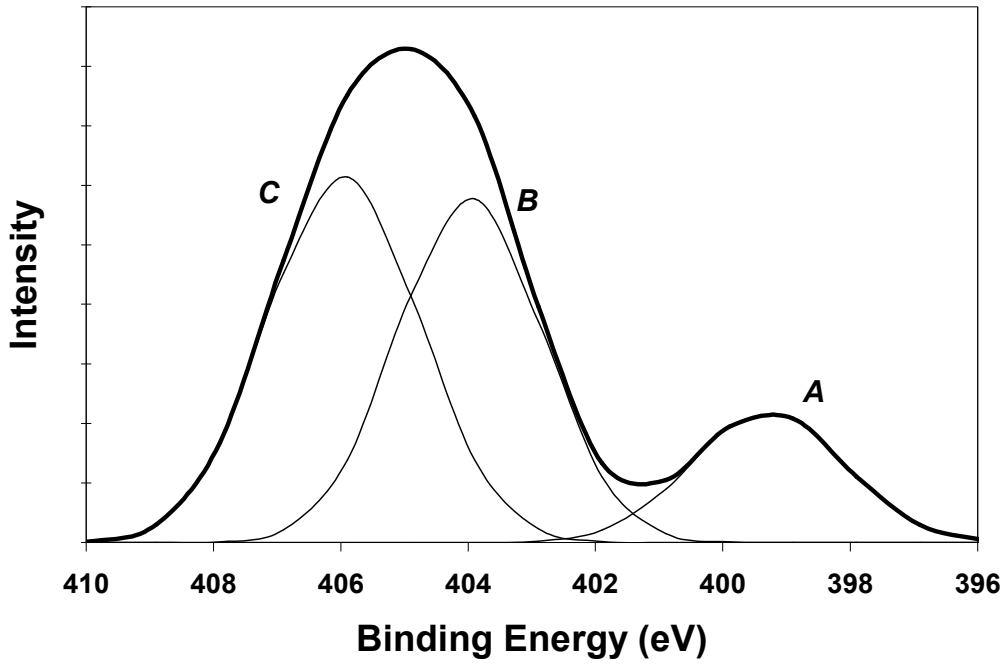

Figure 4.8: N 1s photoemission spectrum of a sol-gel synthesized material using the weak base pyridine. The region is deconvoluted into three peaks corresponding to the C-N bonding representative of pyridine, the C-N^+ bonding representative of a pyridinium ion as well as an N-O peak.

Table 4.5: The binding energies, full-width half-maximum values, percentage of total peak area, and assignment of atoms of the x-ray photoemission spectrum (XPS) of the N(1s) core electron region for a sol-gel synthesized iron (III) oxide/hydroxide from the epoxide pyridine corresponding to Figure 4.8.

Peak Label	BE (eV)	FWHM (eV)	% of Total Area	Assignment of Atoms
		N1s		
A	399.0	1.74	13.4%	**N**-C
B	403.9	2.01	39.8%	**N^+**-C
C	405.9	2.64	46.8%	**N**-O

The material synthesized using the epoxide THF as the gelation agent seems to follow a similar reaction mechanism as that of propylene oxide. The THF molecule is capable of extracting a proton from the coordination sphere of a hydrated iron complex, producing a protonated 1,4 epoxide and the hydroxo ligand, $Fe(OH)(H_2O)^{2+}$. Then, a nucleophile can attack the protonated 1,4 epoxide molecule in an irreversible ring-opening reaction creating a protonated diol, which can deprotonate and form a diol as well as extract hydronium ions into solution, as shown in Equations 6 and 7.

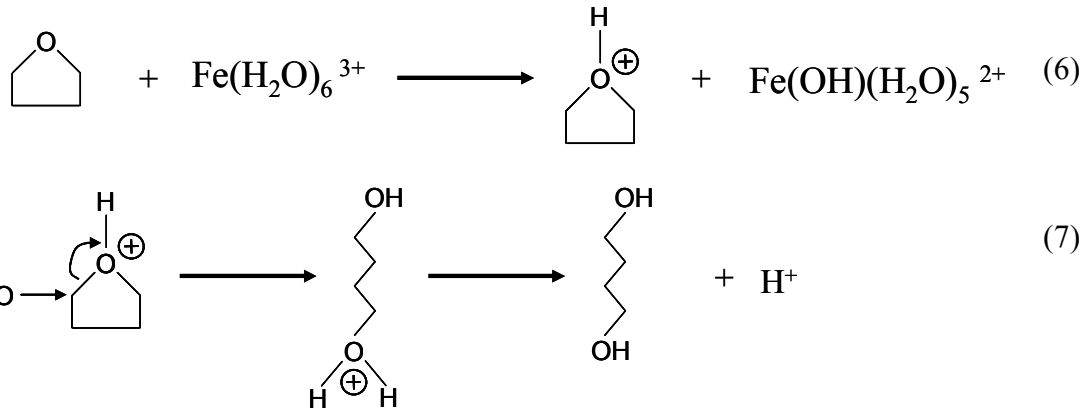

4.4 Summary of elucidation of 'proton scavenging' mechanism

This work deals with the synthesis of iron (III) oxide/hydroxide xerogels from a hydrated ferric nitrate precursor salt ($Fe(NO_3)_3 \cdot 9H_2O$) through the addition of different weak base chemicals, e.g. propylene oxide, pyridine, and tetrahydrofuran, as gelation agents. The dried xerogel samples were characterized by x-ray photoelectron spectroscopy (XPS), x-ray diffraction (XRD), transmission electron microscopy (TEM), and atomic force microscopy (AFM). XPS and x-ray diffraction data show $Fe(2p_{3/2})$ and $Fe(2p_{1/2})$ peaks at values corresponding to that of an amorphous $Fe_2O_3/FeO(OH)$

material. The morphology of the iron oxide/hydroxide xerogels obtained from TEM and AFM images indicates the formation of a "nanonetwork" assembly, with base particles of ~5 nm in diameter aggregated into a network of clusters of ~30 nm in size. In addition to sample characterization, a mechanistic study was performed to probe the formation of the iron oxide/hydroxide xerogel using the three different weak-base gelation agents. Previous work, in which propylene oxide was used as the gelation agent, has proposed that a "proton scavenging" mechanism was responsible for the formation of the xerogel. In the current study, this mechanistic view has been further investigated and generalized to encompass a broader class of weak bases, through pH studies, XPS and infrared spectroscopy.

CHAPTER 5

IRON (III) OXIDE/ALUMINUM NANOENERGETIC MATERIALS SYSTEMS

5.1 Overview

This chapter details the synthesis and characterization of iron (III) oxide/aluminum nanoenergetic materials synthesized by sol-gel chemistry from the gelation chemicals propylene oxide (PO), trimethylene oxide (TMO), and 3,3 dimethyl oxetane (DMO). Section 5.2 outlines the synthesis parameters and results in creating the iron (III) oxide matrices from the different gelation chemicals. Section 5.3 describes the characterization of the energetic (aluminum-containing) systems. Finally, Section 5.4 summarizes the overall trends in the iron (III) oxide/aluminum nanoenergetic materials systems.

5.2 Synthesis of Fe_2O_3/Al xerogels

The addition of PO to a hydrated iron (III) nitrate metal salt precursor and aluminum powder solution results in a heat-releasing reaction with the formation of a monolithic wet gel within 4 minutes. This exothermic reaction corresponds to the sol to gel reaction of the iron oxide material and not to the energetic thermite reaction. This material will be described as Fe_2O_3(PO)/Al where the PO in parentheses designates the

iron (III) oxide/aluminum composite material formed from propylene oxide. The same addition of TMO to an equivalent hydrated iron nitrate metal salt precursor and aluminum powder also results in the formation of a monolithic wet gel overnight. This material will similarly be described as Fe_2O_3(TMO)/Al. The addition of DMO to an equivalent hydrated iron nitrate metal salt precursor and aluminum powder also results in the formation of a monolithic wet gel within 3 days. This material will similarly be described as Fe_2O_3(DMO)/Al. Similar syntheses were performed without the addition of aluminum powder and resulted in equal gelation times. These samples will furthermore be referred to as Fe_2O_3(PO), Fe_2O_3(TMO), and Fe_2O_3(DMO). For all syntheses, a dry, porous xerogel forms after heating the samples in an oven for 7 days at 60°C as solvents are allowed to evaporate.

5.3 Characterization of Fe_2O_3/Al nanoenergetic systems

5.3.1 Characterization of the iron (III) oxide/nano-scaled aluminum systems synthesized from PO, TMO, and DMO

The high-resolution transmission election microscopy image in Figure 5.1(a) shows the Al particles to be circular and approximately 30-40 nm in diameter. Imaging by HRTEM of the Fe_2O_3(PO)/Al sample reveals individual Fe_2O_3 particles on the order of 3-5 nm in direct contact with the Al particles, as shown in Figure 5.1(b). This corresponds well to previously published images of a similar composite. Imaging by TEM of the Fe_2O_3(TMO)/Al sample reveals Fe_2O_3 particles forming clusters on the order of 5-10 nm, as seen in Figure 5.1(c). This is in contrast to the previously published description of fibrous-like particles and can be explained due to post-synthesis processing.[40] The fibrous-like particle morphology was attained by super-critical drying

of the sample to form an aerogel which is more capable of retaining its original synthesized morphology due to less densification. Here, a much higher level of densification is seen due to the drying procedure which could possibly make imaging of these fibers impossible. This phenomenon can also explain the lack of presence of fibers in the Fe_2O_3(DMO)/Al sample. Figure 5.1(d) shows this sample to have Al particles in contact with Fe_2O_3 clusters that are approximately 10-15 nm in diameter.

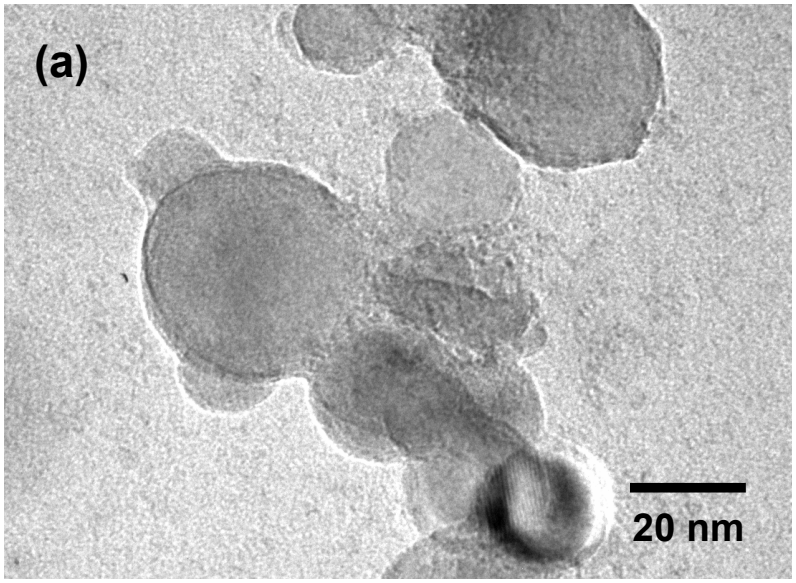

Figure 5.1: HRTEM images of (a) Nanocrystalline Al, (b) Fe_2O_3(PO)/Al, (c) Fe_2O_3(TMO)/Al, and (d) Fe_2O_3(DMO)/Al. The circular particles 30-40 nm in diameter are the Al particles.

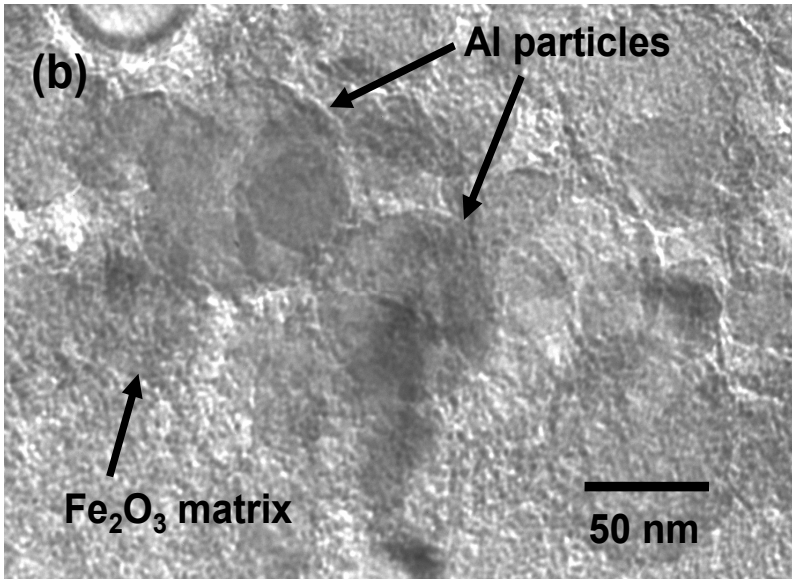

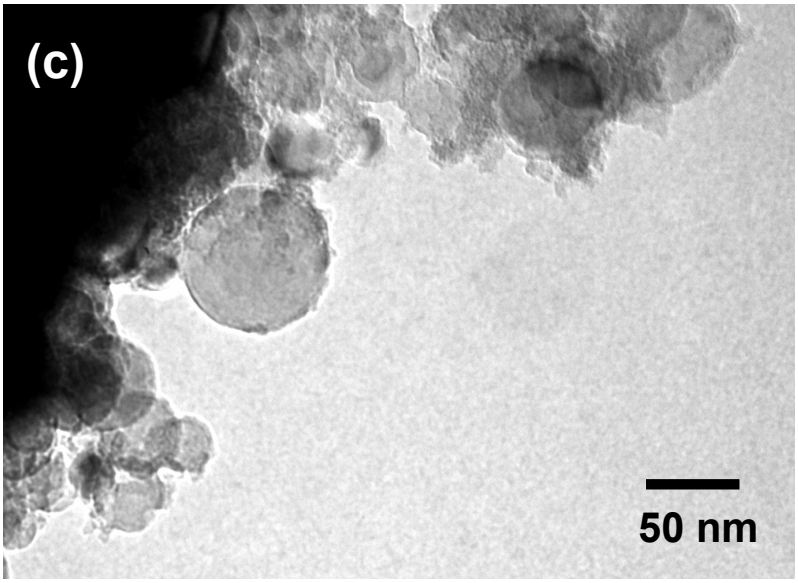

Figure 5.1 continued

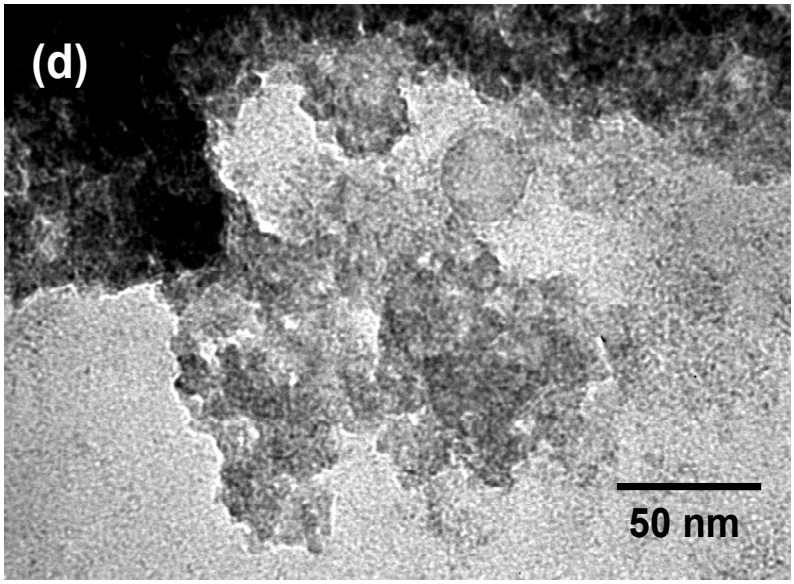

Figure 5.1 continued

Figure 5.2 shows the XRD pattern for the nano-scaled Al powder. The four peaks over the scanned range correspond directly to that of zero-valent aluminum, $Al^{(0)}$. The major diffraction peaks were found at Bragg diffraction angles of 38.5°, 44.7°, 65.2°, and 78.3° which correspond to the (1 1 1), (2 0 0), (2 2 0), and (3 1 1) planes of $Al^{(0)}$, respectively. The diffraction pattern does not show evidence of alumina, Al_2O_3. This is important due to the fact that while Al_2O_3 is the thermodynamically stable form of Al in atmospheric conditions arising from a large and negative free energy of formation for its oxide.[98] It should be assumed, though, that at least a fraction of the aluminum sample has oxidized to form alumina, but it is undetectable by x-ray. This is important due to the fact that Fe_2O_3 will not react with Al_2O_3 in an exothermic thermite-type reaction.

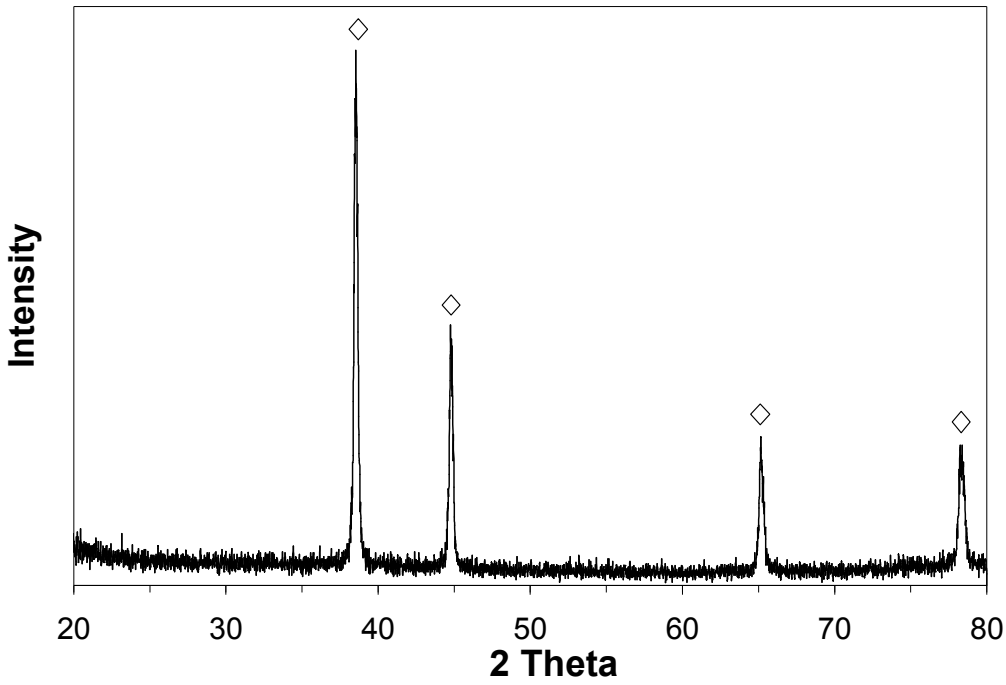

Figure 5.2: X-ray diffraction pattern for nano-scaled aluminum powder. Aluminum peaks are represented by a diamond (◊).

Figures 5.3(a)-5.3(c) show XRD patterns for the as-synthesized Fe_2O_3(PO)/Al, Fe_2O_3(TMO)/Al, and Fe_2O_3(DMO)/Al samples, respectively. The diffraction data confirms the presence of crystalline $Al^{(0)}$ powder as well as the synthesis of an amorphous solid in each of the patterns, as seen with the samples synthesized from the gelation chemicals THF and pyridine. Due to the amorphous character of these solids, evident from the existence of broad peaks representing highly amorphous, slightly crystalline samples, the x-ray diffraction patterns should be analyzed on a more qualitative scale as well as the fact that diffraction peaks broaden in the nano-scale.[34] As also discussed in Section 4.2.1, Figure 5.3(d) shows the diffraction patterns for different iron (III) oxide, hydroxide, and oxyhydroxide phases: γ-Fe_2O_3; $Fe(OH)_3$; FeO(OH), ferrihydrite; α-Fe_2O_3; α-FeO(OH); and β-FeO(OH). It is again shown here that the most

intense peaks from many of these iron (III) phases fall within the broad peaks of the sample diffraction patterns. Due to the overlapping of many of the diffraction patterns of iron oxide and iron hydroxyl phases, definitive XRD identification of the samples is impossible and should be considered a mixture of phases. Duraes et al. has previously analyzed an equivalent Fe_2O_3(PO) gel using XRD and has published a diffraction pattern for the material which was identified as a possible mixture of $Fe(OH)_3$, γ-Fe_2O_3, Fe_3O_4, α-Fe_2O_3, and/or α-FeO(OH).[99] Previous work in our lab has characterized the as-synthesized Fe_2O_3(PO) material using x-ray photoelectron spectroscopy. Deconvolution of the hi-res scans of the O(1s) region also confirms that the material is not a single iron (III) phase, but contains α-Fe_2O_3 and FeO(OH), as well as organic contaminants from the original precursors. Therefore, as the synthesized material contains both hydroxyl and oxyhydroxyl groups in addition to stoichiometric Fe_2O_3, the as-synthesized materials will furthermore be described as $Fe^{(III)}{}_xO_yH_z$, or again using the term "iron (III) oxide." However, the as-synthesized gel, when heated to temperatures of 515°C, completely phase transforms into a single phase, α-Fe_2O_3.[40]

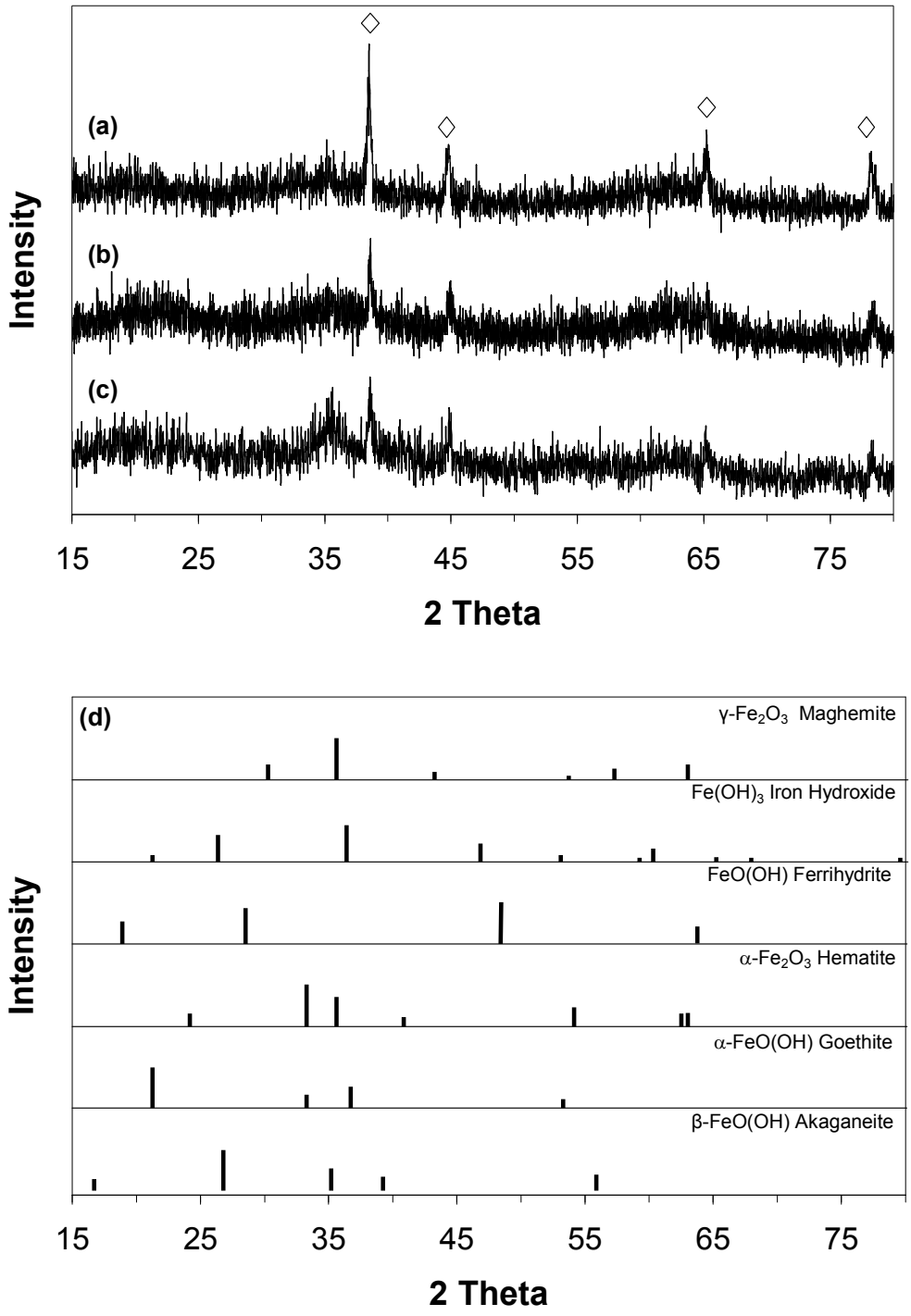

Figure 5.3: X-ray diffraction patterns for the sol-gel synthesized: (a) Fe_2O_3(PO)/Al, (b) Fe_2O_3(TMO)/Al, (c) Fe_2O_3(DMO)/Al xerogel samples after heating for 7 days at 60°C, and (d) theoretical patterns for various iron (III) oxide/oxyhydroxide phases: γ-Fe_2O_3, $Fe(OH)_3$, FeO(OH) (ferrihydrite), α-Fe_2O_3, α-FeO(OH), and β-FeO(OH). The diamond (◊) represents the $Al^{(0)}$ peaks.

The samples were then submitted to a constant heat ramp of 10°C/min under argon purge using a DTA. Figure 5.4 shows the heat traces for the Fe_2O_3(PO)/Al, Fe_2O_3(TMO)/Al, and Fe_2O_3(DMO)/Al samples. Also shown in these graphs is the heat traces of the samples synthesized without aluminum for comparison and to be used as baselines. All samples show endotherms below 200°C which can be attributed to the loss of water[63] and residual organics not removed during the drying procedure. For the Fe_2O_3(PO)/Al sample, shown in Figure 4(a), small exotherms can be seen for both the fuel-containing energetic and non-fuel containing baseline runs at peak temperatures of 230°C and 340°C. These correspond to phase transitions of the amorphous $Fe^{(III)}{}_xO_yH_z$ material into a nanocrystalline material.[7, 34] However, then, a larger exotherm is seen at a peak of 567°C. This exotherm is not seen for the Fe_2O_3(PO) sample and corresponds to the thermite Fe_2O_3/Al reaction. The integrated heat of reaction is -864 J/g using integration limits of 420°C and 670°C. A previous report on a similarly synthesized Fe_2O_3(PO)/Al sample using aluminum particles with a diameter of approximately 25 nm had an integrated heat of reaction of -1.5 kJ/g.[5] This directly demonstrates that the interfacial surface area contact between the Fe_2O_3 and Al particles has a dramatic effect on the heat of reaction of the system. The decrease in the size of the $Al^{(0)}$ particles by 38%, 40 nm to 25 nm, increases the heat of reaction by over 80%.

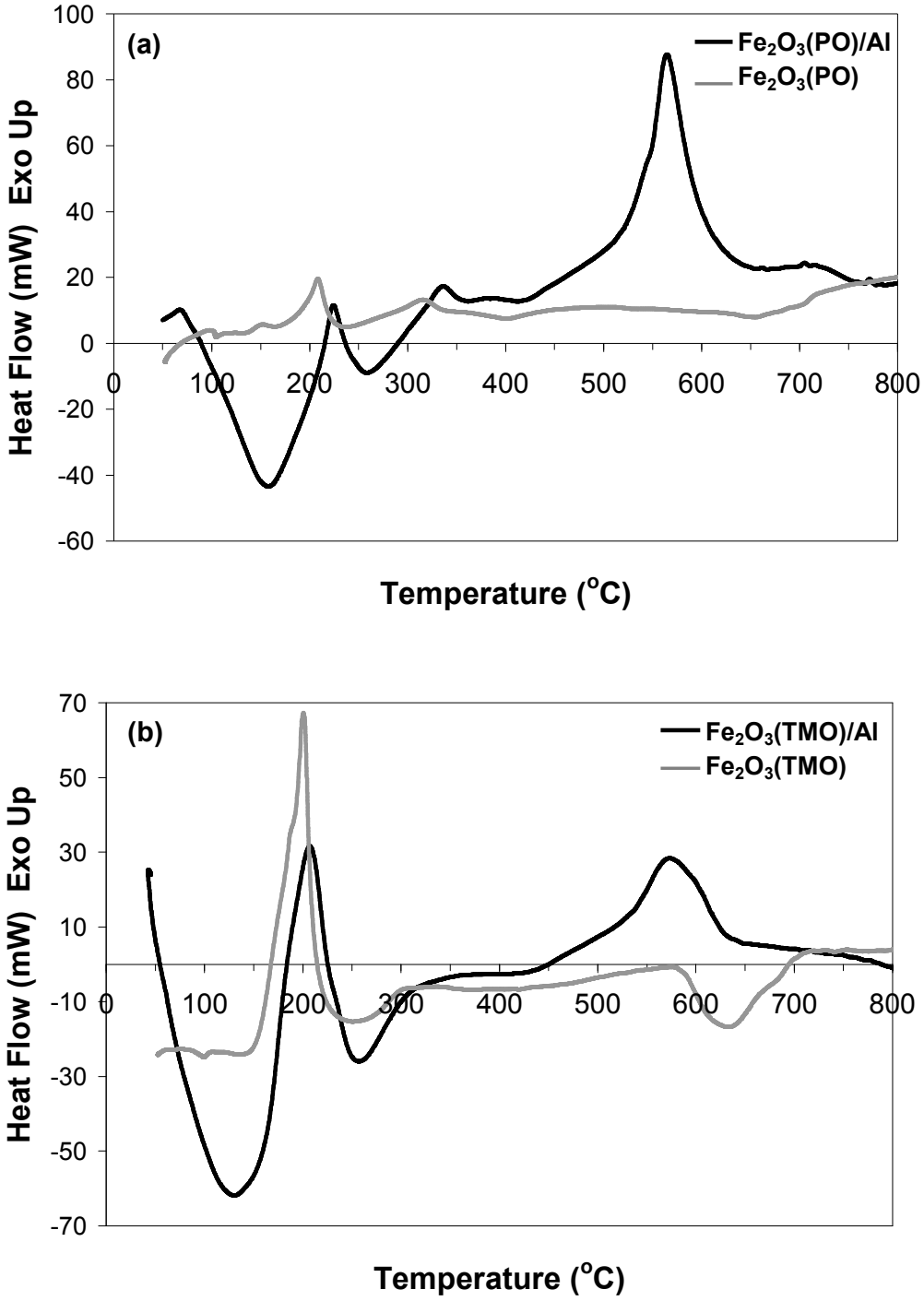

Figure 5.4: DTA trace for the (a) Fe_2O_3(PO)/Al, (b) Fe_2O_3(TMO)/Al, and (c) Fe_2O_3(DMO)/Al samples. Exotherms below 400°C correspond to crystallization of the amorphous $Fe^{(III)}{}_xO_yH_z$ matrix while the exotherm above this temperature corresponds to the thermite reaction.

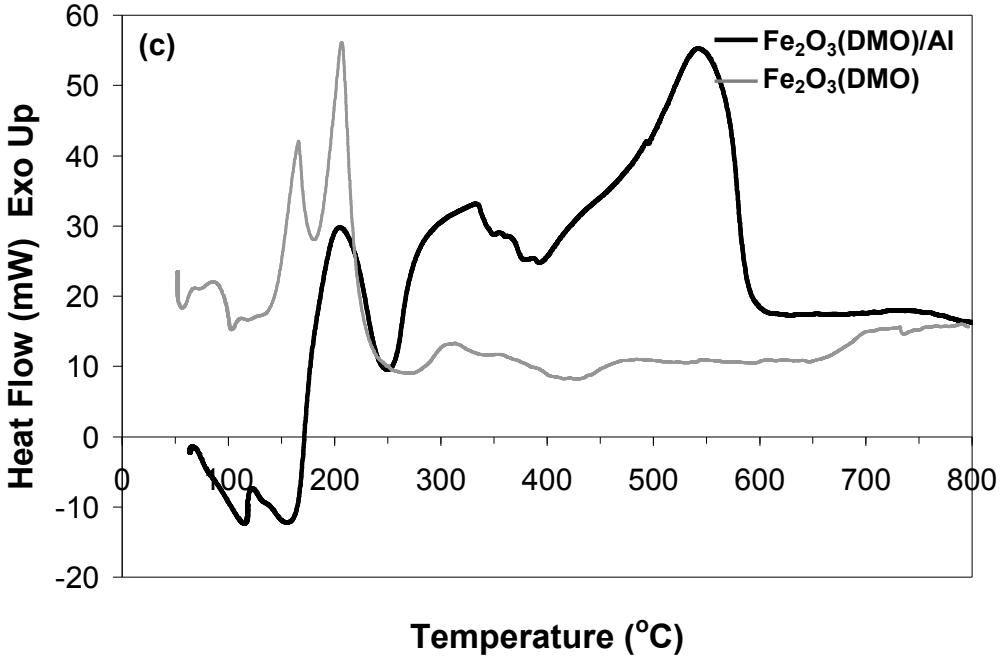

Figure 5.4 continued

Figure 5.4(b) shows the DTA trace of the Fe_2O_3(TMO)/Al sample where, again, exotherms can be seen at 210°C and 340°C, corresponding to phase transitions of the amorphous $Fe^{(III)}{}_xO_yH_z$ material into a crystalline material. The exotherm at 210°C is larger for this sample possibly due to the higher percentage of amorphous FeO(OH) in the as-synthesized material going through the phase transformation to the crystalline Fe_2O_3 phase as the pre-DTA x-ray diffraction pattern for the sample has a larger band than the Fe_2O_3(PO)/Al sample at a Bragg angle of approximately 21°, the most intense peak associated with α-FeO(OH), goethite. Then, another large exotherm is seen at a peak of 577°C. This exotherm corresponds to the thermite Fe_2O_3/Al reaction with a heat of reaction of -505.8 J/g using integration limits of 430°C and 630°C. Interestingly, the sample displays an endotherm at ~580°C, which, after post-DTA x-ray analysis,

corresponds to the reduction of iron (III) oxide to that of iron (II) oxide, wustite, an unstable form of iron oxide.

The Fe_2O_3(DMO)/Al sample follows the same pattern as the other two samples, as seen in Figure 5.4(c). Exotherms corresponding to the crystallization of the amorphous $Fe^{(III)}{}_xO_yH_z$ material are seen at peak temperatures of 200°C and 320°C. The thermite Fe_2O_3/Al reaction occurs at a peak temperature of 536°C with a heat of reaction of –779 J/g using integration endpoints of 390°C and 605°C.

To further analyze the DTA data for the thermite reaction, Figure 5.5 shows an overlay of the three samples in the temperature range of the thermite reaction demonstrating similarities in each heat trace. The exotherms for the Fe_2O_3(PO)/Al and Fe_2O_3(TMO)/Al samples start with a deviation from the baseline at ~420°C and return to the baseline at ~620°C. Fe_2O_3(DMO)/Al commences reaction slightly earlier, at ~400°C, with completion of the reaction also slightly earlier, at ~600°C. All samples have a reaction temperature interval of ~200°C. Fe_2O_3(PO)/Al and Fe_2O_3(TMO)/Al have similar reaction peak temperatures, 567°C and 577°C, respectively. Continuing the trend, Fe_2O_3(DMO)/Al has a peak temperature of 549°C, again slightly lower than the other two samples.

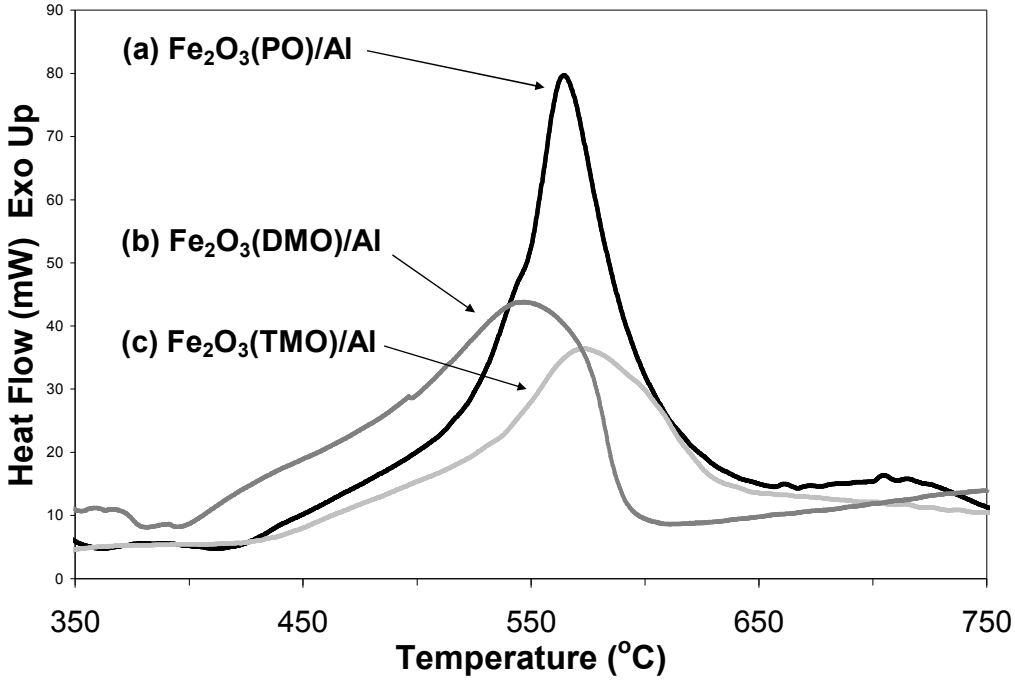

Figure 5.5: Overlay of the DTA traces for the (a) Fe_2O_3(PO)/Al, (b) Fe_2O_3(DMO)/Al and (c) Fe_2O_3(TMO)/Al samples in the temperature range of the exothermic thermite reaction.

It has been previously mentioned that there is a complete phase transformation of the amorphous $Fe^{(III)}_xO_yH_z$ matrix to α-Fe_2O_3 below 515°C, however, here all reactions occur roughly 100-120°C lower than this temperature. To verify that the thermite reaction corresponds only to stoichiometric iron (III) oxide and aluminum, the Fe_2O_3(PO) sample was heated in a DTA to 420°C, a temperature chosen to identify the phase of the $Fe^{(III)}_xO_yH_z$ matrix at the starting temperature of the thermite reactions. Figure 5.6(a) shows the XRD pattern for this sample after heating. The pattern matches very well to that of γ-Fe_2O_3, maghemite, as shown in Figure 5.6(b). Therefore, the thermite sample does correspond to a reaction between stoichiometric γ-Fe_2O_3 and Al, as required in the thermite reaction.

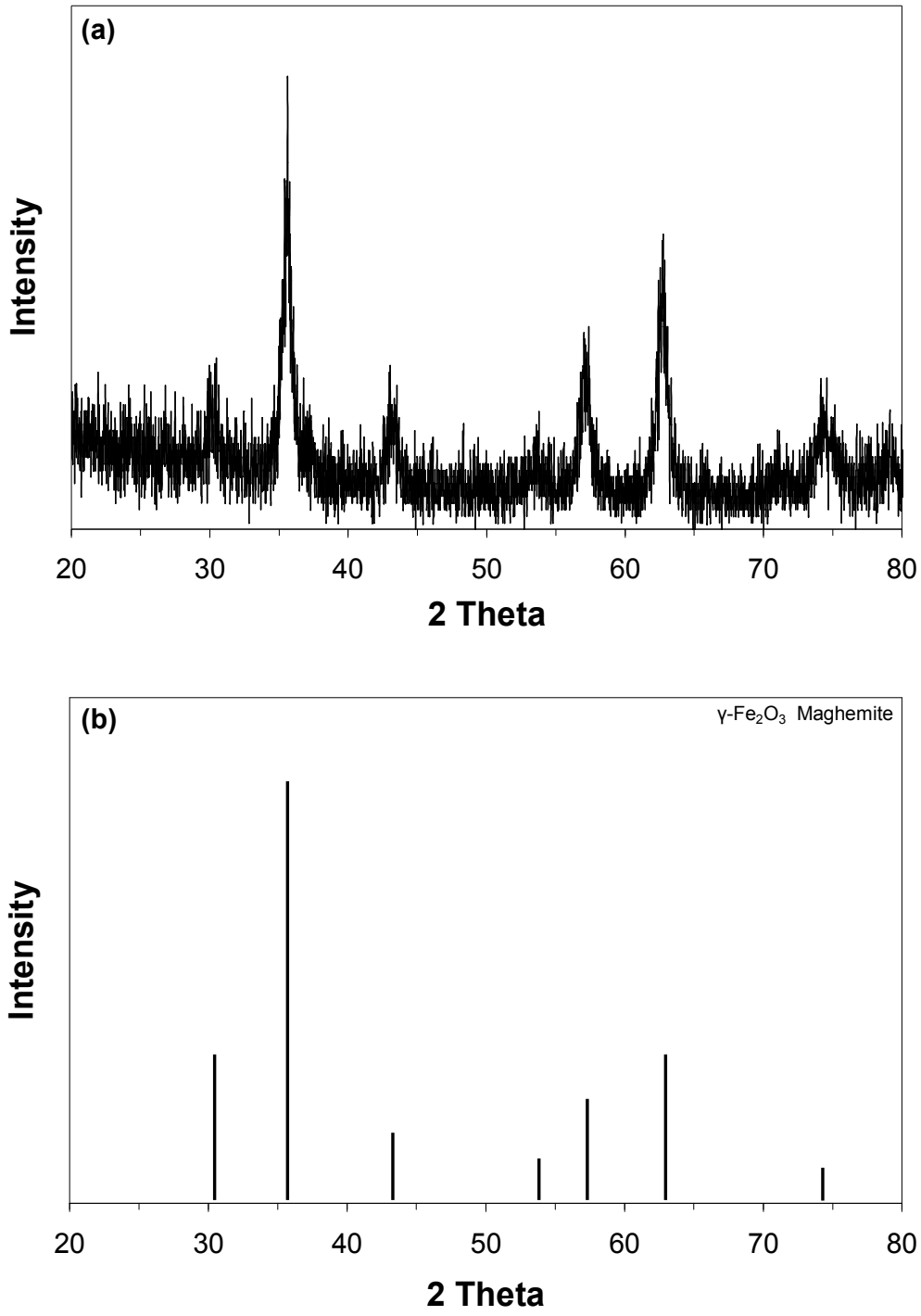

Figure 5.6: (a) XRD pattern for the Fe_2O_3(PO) heated to 420°C in a DTA. The sample pattern matches very well with the theoretical pattern of γ-Fe_2O_3, maghemite, as shown in (b).

In order to examine the differences in the heat of reactions values for the Fe_2O_3(PO)/Al, Fe_2O_3(TMO)/Al, and Fe_2O_3(DMO)/Al samples, Table 5.1 shows the experimental surface area values for the three $Fe^{(III)}_xO_yH_z$ materials synthesized without the addition of Al powder as well as the heat of reaction values for the energetic samples calculated from DTA data. The Fe_2O_3(PO) sample has a surface area of 521.6 m^2/g, the Fe_2O_3(TMO) sample has a surface area of 219.2 m^2/g, and the Fe_2O_3(DMO) sample has a surface area of 345.2 m^2/g. These values indicate that the $Fe^{(III)}_xO_yH_z$ matrix morphologies possess different quantities of accessible surface area available for the Al particles to contact. With the highest oxide matrix surface area, the Fe_2O_3(PO)/Al material should have the highest heat of reaction when reaction occurs due to the largest amount of interfacial contact area between the iron (III) oxide and Al phases. Conversely, the Fe_2O_3(TMO)/Al sample should have the lowest heat of reaction value. The DTA results confirm this assumption as well as the ability of sol-gel chemistry to synthesize Fe_2O_3/Al nanocomposites with different iron oxide matrix morphologies in order to tailor the heat of reaction of the system directly due to the amount of interfacial surface area contact between the iron oxide and aluminum particles.

Table 5.1: Surface area values for the three sol-gel synthesized $Fe^{(III)}_xO_yH_z$ materials and the integrated heat of reaction values for the corresponding Al containing energetic samples.

Material	Surface Area (m^2/g)	Heat of Reaction (J/g)
Fe_2O_3(PO)	**521.6**	**-821**
Fe_2O_3(TMO)	**219.2**	**-408**
Fe_2O_3(DMO)	**345.2**	**-575**

Important to note is the starting temperature of the reaction is well below that of the melting point of bulk Al, 660.5°C.[100] This phenomenon has been noted previously.[7] It has been thought that the initiation of the thermite reaction corresponds to the melting of the less refractory material, which, in this case, is the nanocrystalline Al powder.[101] Nanocrystalline Al has been shown to a have a lower melting temperature, sometimes up to 300K lower than the bulk material, due to the large fraction of atoms on the surface of each particle.[102] To examine this, bulk Al and the nano-scale Al powder used in the sol-gel syntheses of all samples were heated at 10°C/min in a DTA using argon as the purge gas. Figure 5.7 shows DTA traces of the bulk and nano-sized Al particles. Whereby bulk Al has a single, sharp melting endotherm which starts at 650°C with a peak maximum at 660°C, the nano-scale Al shows two endotherms. The first melting endotherm begins at 450°C with a peak maximum at 550°C, and the second, broader endotherm starts immediately after the first endotherm with a peak maximum at 660°C, corresponding to the melting point of bulk Al. Thermodynamically, the melting of the nano-sized Al particles, as displayed by the first endotherm, lowers the free energy necessary for the melting of any possible Al aggregates that form, as displayed by the second broad endotherm, up to the melting of aggregates which behave as bulk Al. The DTA trace in Figure 5.5 demonstrates that the exotherms occurring due to the thermitic reaction between Fe_2O_3 and Al species for all samples commences by 420°C, 30°C below the start of melting of the Al powder. Therefore it can be seen that the thermite reaction occurring here does not start simply due to the melting of the nano-sized Al powder, and another explanation for the onset of the reaction is necessary. A possible explanation for the start of the reaction can be extracted from the DTA heating of the Fe_2O_3(PO) sample,

as seen in Figure 5.8. A small exothermic transition can be seen starting at 420°C, the exact starting temperature of the thermite reaction for the Fe_2O_3(PO)/Al sample. Therefore, it can be deduced that this exotherm is able to lower the activation barrier for the start of the reaction to occur.

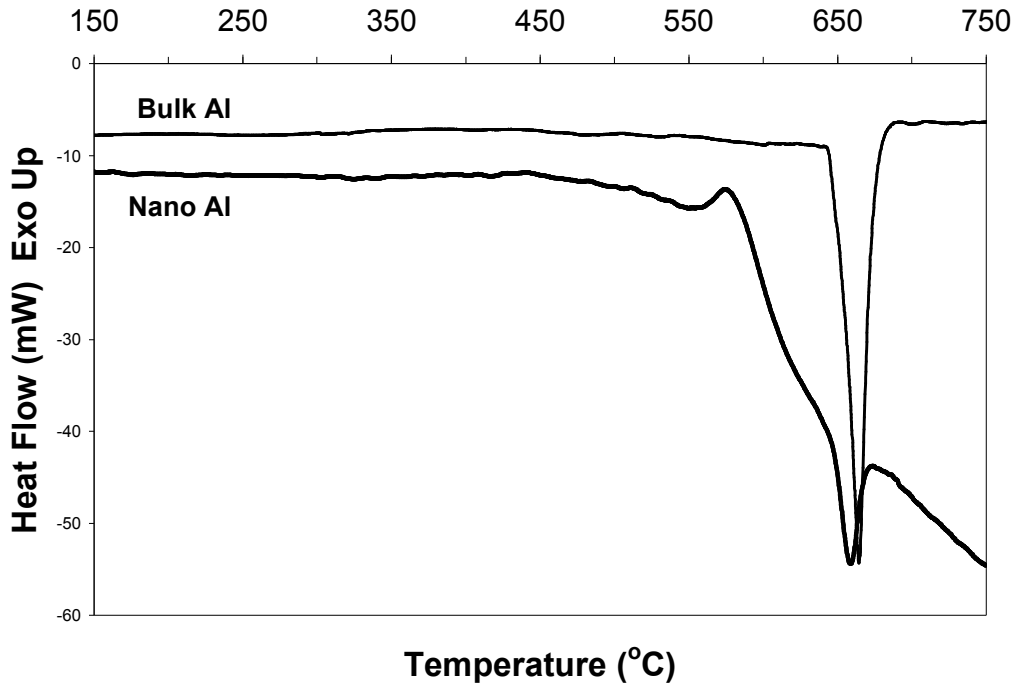

Figure 5.7: DTA traces showing melting of bulk and nano-scaled Al powder used in the described experiments. Bulk Al shows a single, sharp melting endotherm, while the nano-scaled Al displays two endotherms, a first, smaller endotherm corresponding to the melting of the nano-sized particles, while the second corresponds to the melting of larger Al aggregates.

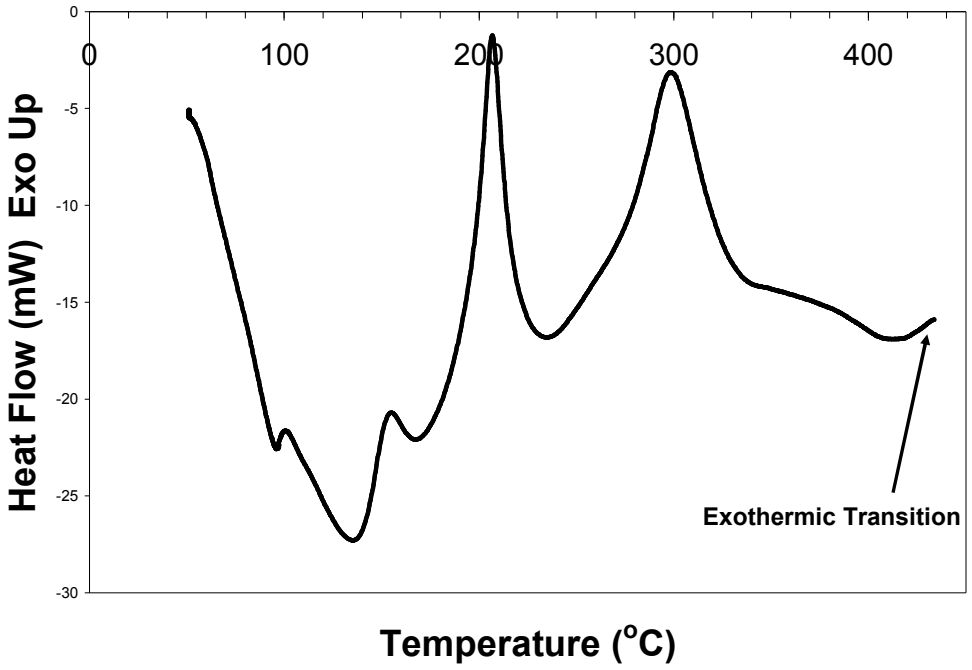

Figure 5.8: DTA trace of the Fe_2O_3(PO) sample to a temperature of 440°C at 10°C/min. An exothermic transition can be seen starting at 420°C.

All heat of reaction values quantified are significantly lower than the theoretical value of -3.9 kJ/g for a stochiometric Fe_2O_3/Al thermite reaction. There are numerous explanations for the lowered heats of reaction for the reaction between Fe_2O_3 and $Al^{(0)}$ in comparison to theoretical values for all samples. One reason is that the Al powder is prone to form a thin Al_2O_3 layer around each Al particle, as Al_2O_3 is the more thermodynamically stable form of Al in atmospheric conditions. This Al_2O_3 layer, small enough to where it is indiscernible in x-ray diffraction patterns, can account for a large percentage of the total volume of the nano-scaled Al particle, thereby reducing its reactivity.[5] Also, the theoretical value for the reaction between Fe_2O_3 and $Al^{(0)}$ accounts for complete interaction at the molecular scale. The individual Fe_2O_3 and Al particles, although on the nanometer scale, are unable to achieve absolute molecular interaction

thereby lowering the maximum possible heat of reaction. A third explanation for the lower heat of reaction value is that contaminants trapped in the solid network that are not purged during the post-synthesis drying process such as salt anion, solvent, and unreacted gelation agent reduce iron oxide content per weight so as to reduce the maximum possible heat of reaction for the sample materials.[99] Also, during the gelation stage of the synthesis, Al particles could settle through the $Fe^{(III)}_xO_yH_z$ matrix due to gravity, creating an Al concentration gradient within the iron oxide matrix. Then thermal analysis data depends greatly on which area of the energetic material the sample is taken. As all three samples were synthesized using the same procedure, we can assume these issues would apply to all systems equally and would not effect the relative heat of reaction values for the samples.

Post-DTA XRD runs were performed to determine the products of the reactions and to verify the existence of Al_2O_3 and Fe, the products of a successful thermite reaction. Figure 5.9(a) shows the XRD pattern of the post-DTA Fe_2O_3(PO)/Al sample. Whereas the pre-DTA x-ray diffraction patterns shows an amorphous iron oxide/hydroxide material, the post-DTA x-ray diffraction patterns show the formation of crystalline products which correspond directly to that of Al_2O_3 and Fe, the products of the thermite reaction between Fe_2O_3 and Al. Figures 5.9(b) and 5.9(c) also show the x-ray diffraction patterns for the post-DTA reaction of the Fe_2O_3(TMO)/Al and Fe_2O_3(DMO)/Al samples, respectively. Unfortunately, due to the sample preparation procedure of placing Al_2O_3 powder within the alumina crucibles used in the DTA, the post-DTA XRD patterns also include this quantity of Al_2O_3, thereby making it impossible to accurately perform quantitative extent of reaction analysis of the reaction products.

Therefore, in examining the post-reaction products to confirm the thermite reaction, it is more telling to examine the existence of Fe diffraction peaks at Bragg diffraction angles of 44.712°, 65.082°, and 82.416°, corresponding to the (1 1 0), (2 0 0), and (2 1 1) planes, respectively. These three Fe peaks are seen in each of the diffraction patterns of the three samples, verifying the thermite reaction. Also, these diffraction patterns do not show the reactant Al. As many of the reflections of zero-valent Al and Fe overlap, the absence of Al is evidenced by the omission of the most intense Al peak located at a Bragg angle of 38.5°.

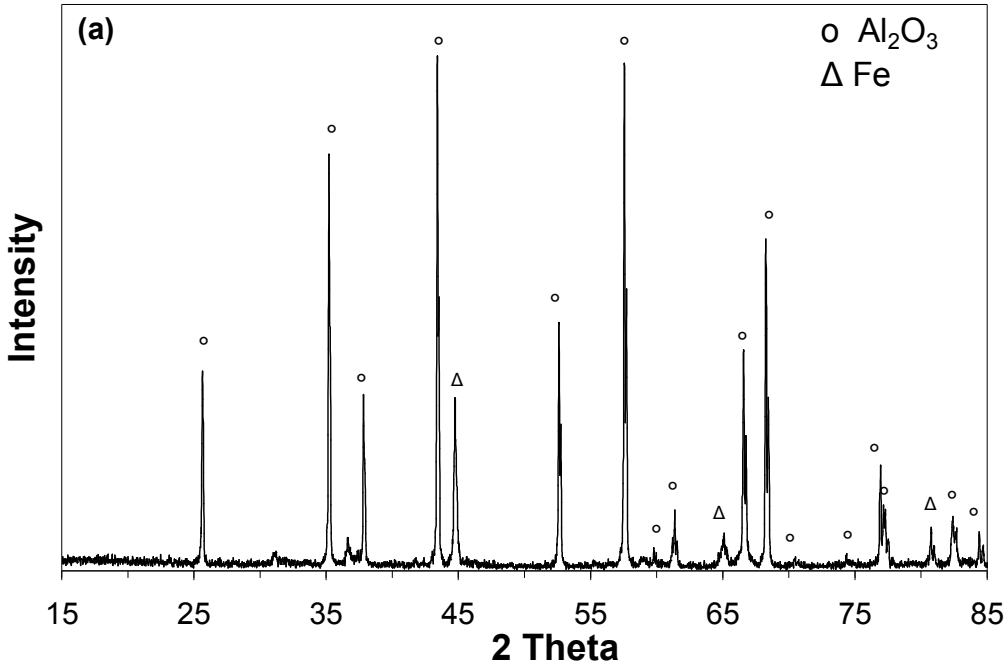

Figure 5.9: X-ray diffraction pattern for the (a) Fe_2O_3(PO)/Al, (b) Fe_2O_3(TMO)/Al and (c) Fe_2O_3(DMO)/Al samples post-DTA demonstrating the formation of the thermite reaction products, Al_2O_3 and Fe.

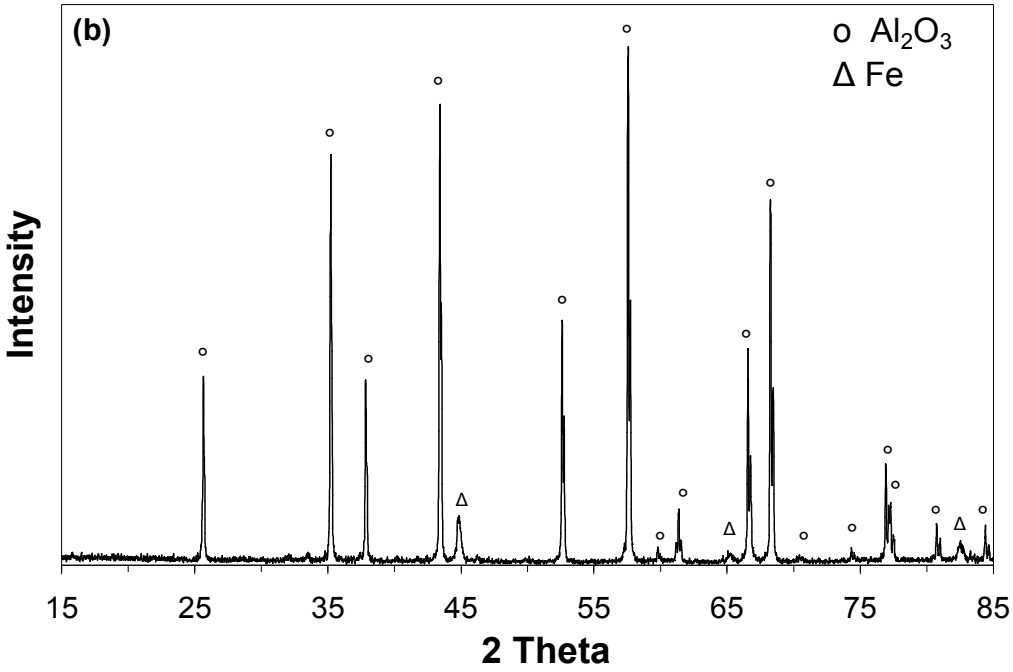

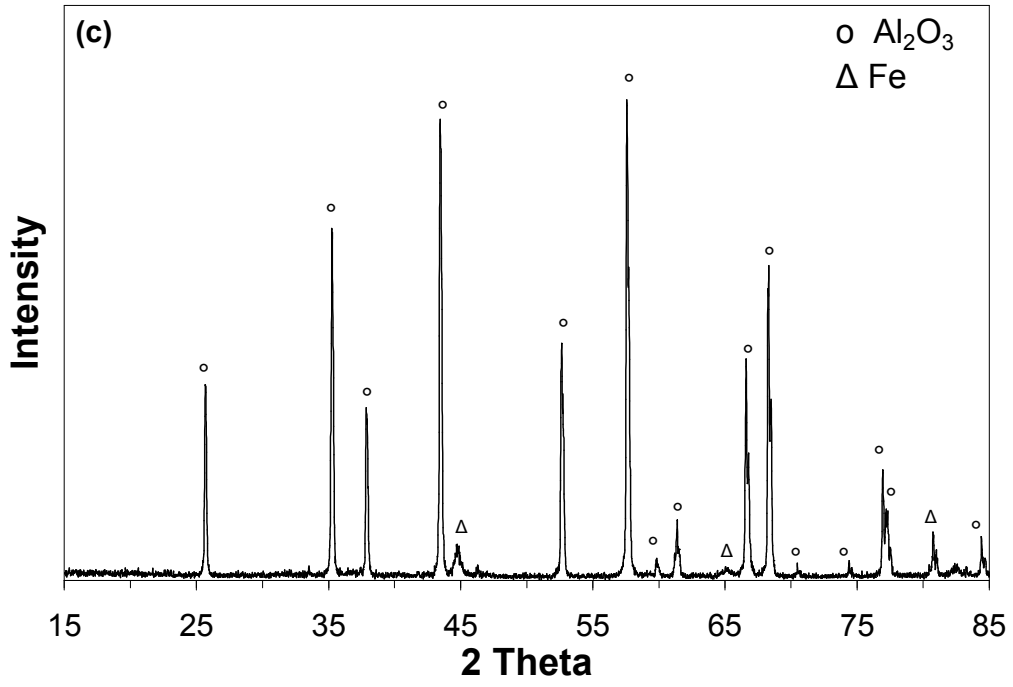

Figure 5.9 continued

5.3.2 Analysis of reactivity of other Fe_2O_3/Al nanoenergtic composite systems

5.3.2.1 Characterization of other systems prepared from propylene oxide

In addition to the samples synthesized with a 1:1 stoichiometric ratio of Fe:Al, other samples were prepared from the gelation chemicals PO, TMO, and DMO (see Table 3.1). These systems include the addition of 3x the stoichiometric ratio of nano Al powder and ½ the stoichiometric ratio of nano Al. These specific systems were chosen to study if the maximum achievable experimental heat of reaction is as it is in the balanced thermite reaction (1:1 Fe:Al). Also, systems were studied with the addition of micron Al in contrast to the nano Al. This study was designed to verify that the larger micron Al particles, with lower specific surface values, will result in lower heats of reaction due to less interfacial contact area between the iron (III) oxide and Al reaction species. Finally, systems were studied with the addition of carbon nanotubes (CNT). Carbon nanotubes are desired additives to nanoenergetic materials due to their ability to be aligned within the gel matrix to add structural integrity to the brittle synthesized gels. Figure 5.10 shows the XRD pattern of the CNT used in the studies. Due to their amorphous nature, the pre-DTA XRD patterns of the systems listed here are equivalent to the pattern shown in Figure 5.3.

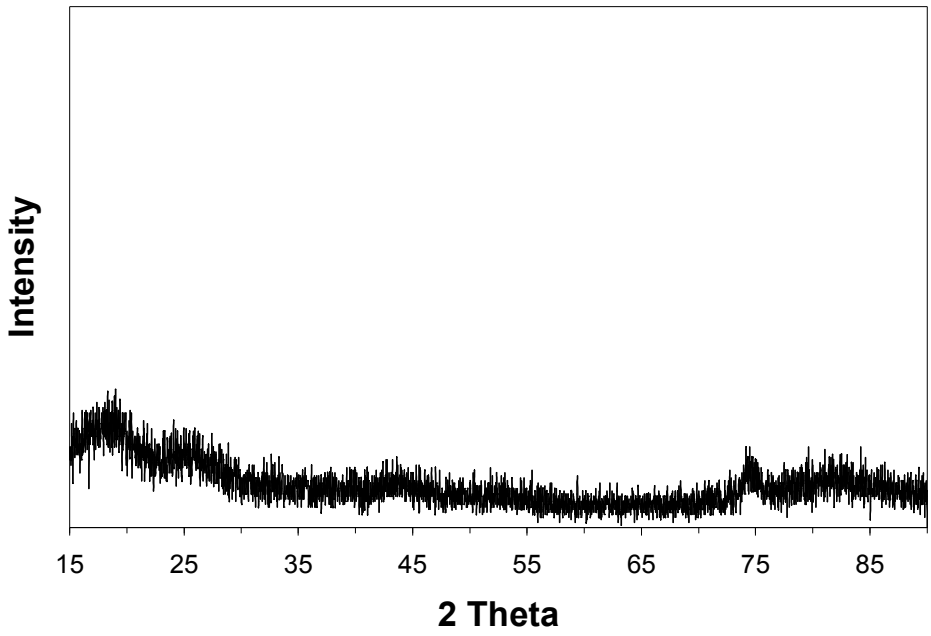

Figure 5.10: XRD pattern of the carbon nanotubes (CNT) used in the synthesis of iron (III) oxide materials.

Figure 5.11 shows a composite graph of the DTA traces of all the iron (III) oxide/aluminum systems studied from the gelation chemical propylene oxide, PO. The 1:1 Fe:nano Al sample has the overall highest heat of reaction at -864.4 J/g. Interestingly, the 3x stoichiometric nano Al sample displays two exotherms, one with an onset of 405°C, peak of 515°C, and integrated heat of reaction of -514.7 J/g and one exotherm starting at 650°C, peak of 668°C and an integrated heat of reaction of -33.3 J/g. The trace also displays an endotherm with an onset of 630°C and a peak maximum of 646°C corresponding to the melting of excess, unreacted Al aggregates from the original synthesis which here act more as a bulk scale material. This melting allows for an increase in diffusion of aluminum particles in the liquid state enabling the start of a second reaction between unreacted iron (III) oxide and aluminum species. The ½

stoichiometric quantity of nano Al sample also displays an exotherm before the bulk melting temperature of aluminum. The reaction starts at 426°C with a peak temperature of 551°C. The integrated heat of reaction is -554.7 J/g. Interestingly there is also a second exotherm here arising from the melting of aggregates of Al with a heat of reaction of -29.5 J/g. This implies that the initial reaction between iron (III) oxide and aluminum does not go to completion, and a second reaction, where there is an increase in diffusion of the aluminum particles in the liquid state, is able to occur. However, the magnitude of the second exotherm is considerably smaller than the primary reaction, less than 10% of the fraction of the overall magnitude. Finally, the sample synthesized with 1:1 Fe:nano Al plus CNT has an integrated heat of reaction of -689.7 J/g. The single exotherm starts at 427°C with a peak maximum of 561°C. Based on a per weight basis, CNT do not enhance the heat of reaction.

The samples synthesized with micron Al follow a different reaction sequence. Whereas samples synthesized with nano Al commence reaction at ~430°C, the samples synthesized with micron-scale Al commence reaction at much greater temperatures. The 1:1 Fe: micron Al sample commences reaction at 872°C with a peak reaction temperature of 968°C. The integrated heat of reaction for this sample is -395.6 J/g. For this sample, no exothermic reaction between the iron (III) oxide and aluminum particles occurs until after the micron Al particles melt, as is the traditional mechanism for the thermite reaction. The aluminum particles melt with a peak temperature of 661°C, corresponding to the melting point of bulk aluminum. The 1:1 Fe:micron Al plus CNT sample starts the iron (III) oxide/aluminum reaction at 756°C with a peak maximum at 822°C. The heat of reaction is -480.7 J/g.

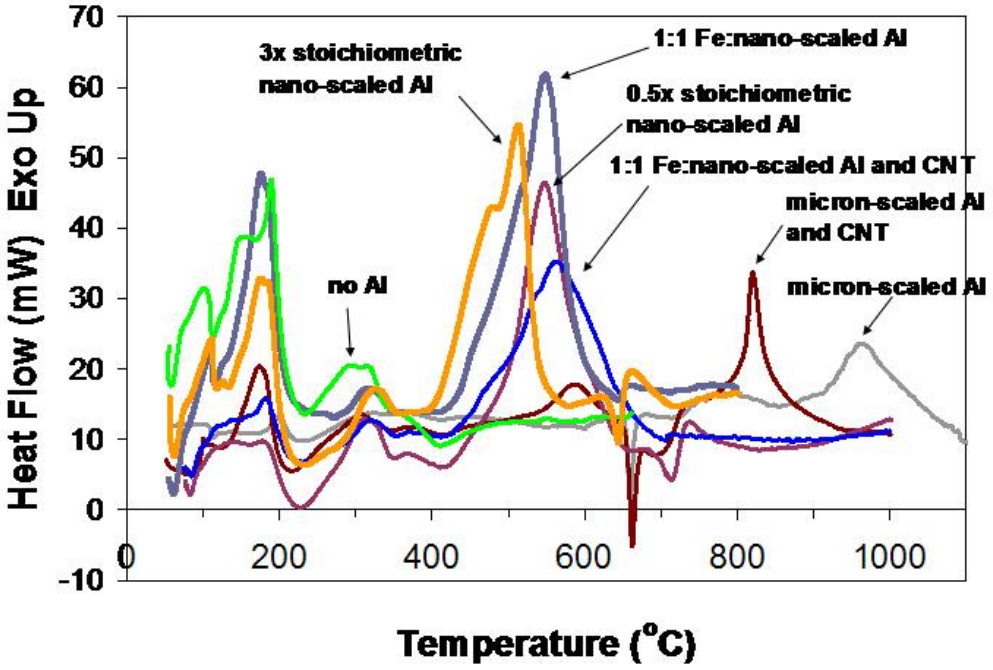

Figure 5.11: Composite figure of the DTA traces of the iron (III) oxide/aluminum systems synthesized from the gelation chemical propylene oxide (PO).

Post-DTA XRD patterns are shown in Figure 5.12. Whereas the pre-DTA x-ray diffraction patterns show an amorphous iron oxide/hydroxide material, the post-DTA x-ray diffraction patterns show the formation of crystalline products which correspond directly to that of Al_2O_3 and Fe, the products of the thermite reaction between Fe_2O_3 and Al. Again, unfortunately due to the sample preparation procedure of placing Al_2O_3 powder within the alumina crucibles used in the DTA, the post-DTA XRD patterns also include this excess quantity of Al_2O_3, thereby making it impossible to accurately perform quantitative extent of reaction analysis of the reaction products. Therefore, in examining the post-reaction products to confirm the thermite reaction, it is more telling to examine the existence of Fe diffraction peaks at Bragg diffraction angles of 44.712°, 65.082°, and

82.416°, corresponding to the (1 1 0), (2 0 0), and (2 1 1) planes, respectively. In Figure 5.12(a), the sample heated with 3x the stoichiometric Al quantity, peaks corresponding to unreacted Al are clearly visible. This indicates that the quantity of iron (III) oxide within the system was the limiting reaction factor. In addition, the most intense Fe peak is visible, confirming a successful thermite reaction. Figures 5.12(b)-5.12(e) all show the most intense Fe peak indicating a successful thermite reaction.

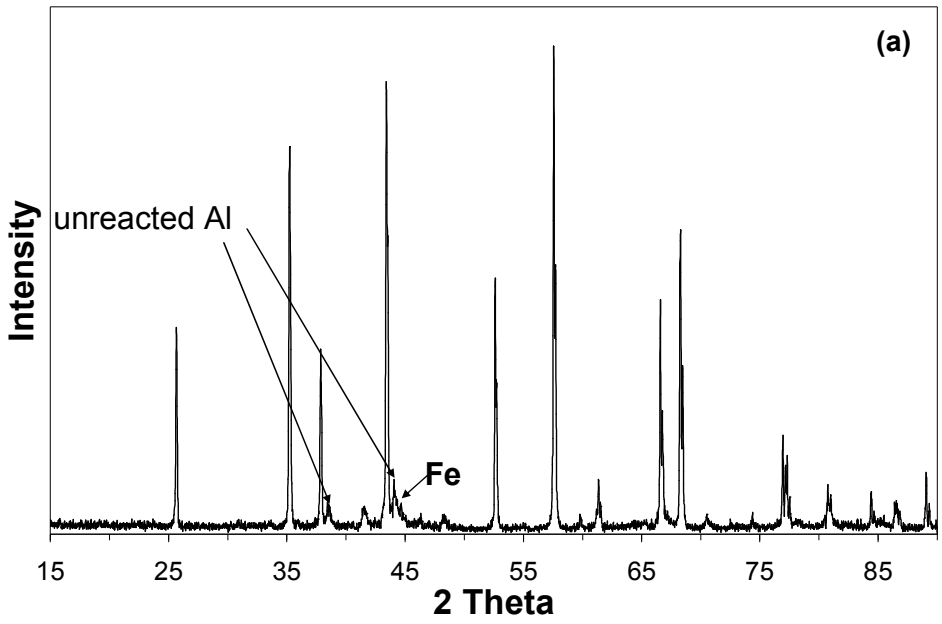

Figure 5.12: XRD patterns of other iron (III) oxide/aluminum systems heated in a DTA to 1000°C at 10°C/min using propylene oxide as the gelation chemical. (a) Fe_2O_3/3x stoichiometric ratio of Fe:nano Al (3 x 0.083 g = 0.249 g Al), (b) Fe_2O_3/½ stoichiometric ratio of nano Al (½ x 0.083 g = 0.0415 g), (c) Fe_2O_3/1:1 Fe nano Al plus CNT, (d) Fe_2O_3/1:1 Fe:micron Al, and (e) Fe_2O_3/1:1 Fe:micron Al plus CNT.

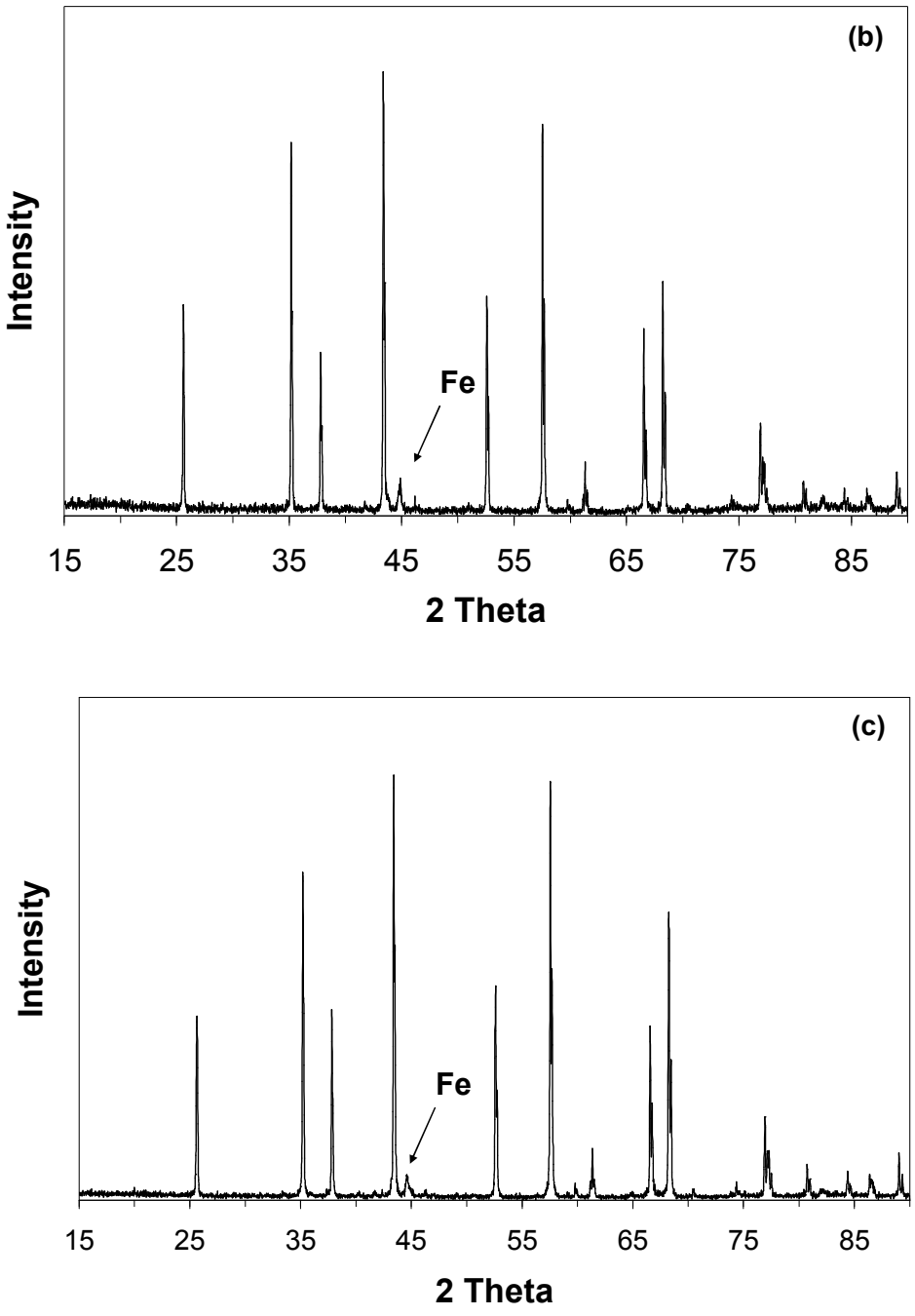

Figure 5.12 continued

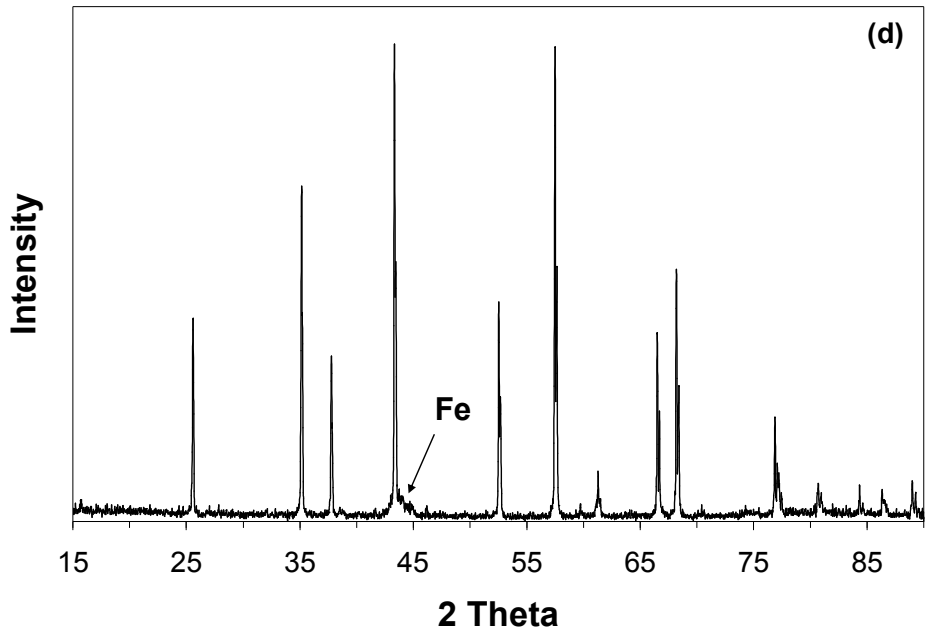

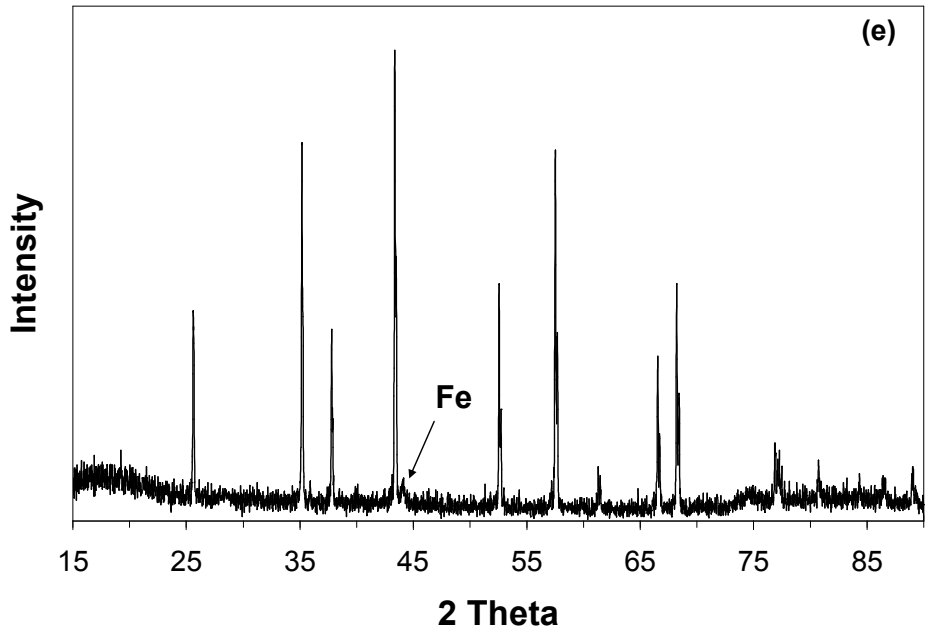

Figure 5.12 continued

5.3.2.2 Characterization of other systems prepared from trimethylene oxide

As with the gelation chemical propylene oxide, similar samples were prepared from the gelation chemical trimethylene oxide. Figure 5.13 shows a composite graph of the DTA traces of all the iron (III) oxide/aluminum systems studied from the gelation chemical trimethylene oxide (TMO). The 1:1 Fe:nano Al sample has the overall highest heat of reaction within the samples synthesized from TMO at -505.8 J/g. Again, the 3x stoichiometric nano Al sample displays two exotherms, one with an onset at 433°C, peak of 543°C, and integrated heat of reaction of -388.6 J/g and one exotherm starting at 650°C, peak of 667°C and an integrated heat of reaction of -31.6 J/g corresponding to the reaction initiated after the aluminum aggregates melt and commence a secondary reaction. The trace also displays an endotherm with an onset of 634°C and a peak maximum of 647°C corresponding to the melting of excess, unreacted Al aggregates from the original synthesis which here act more as a bulk scale material. The ½ stoichiometric quantity of nano Al sample also displays a small exotherm before the bulk melting temperature of aluminum. The reaction starts at 428°C with a peak temperature of 479°C. The integrated heat of reaction is -101.4 J/g. There is also a second exotherm here arising from the melting of aggregates of Al with a heat of reaction of -95.6 J/g. Interesting here is that the magnitude of the secondary endotherm is comparable to that of the primary reaction. This is the one exception to the assumption that the second endotherm accounts for less than 10% of the overall heat of the iron (III) oxide/aluminum reaction. Finally, the sample synthesized with 1:1 Fe:nano Al plus CNT has an integrated

heat of reaction of -483.1 J/g. The single exotherm starts at 426°C with a peak maximum of 559°C. Again, CNT do not appear to enhance the heats of reaction.

The TMO sample synthesized with micron Al again follows a different reaction sequence. The 1:1 Fe: micron Al sample commences reaction at 759°C with a sharp peak at a temperature of 810°C. This repeatable result differs from that of the same micron Al samples synthesized from PO and DMO where a sharp peak is seen as opposed to a broad exotherm. The integrated heat of reaction for this sample is -279.9 J/g. Again, no exothermic reaction between the iron (III) oxide and aluminum particles occurs until after the micron Al particles melt. The aluminum particles melt with a peak temperature of 662°C, corresponding to the melting point of bulk aluminum. In comparison to similar samples synthesized from PO and DMO, the TMO samples have the lowest heats of reaction due to the lowest accessible surface area for the aluminum particles to interact with the iron (III) oxide matrix.

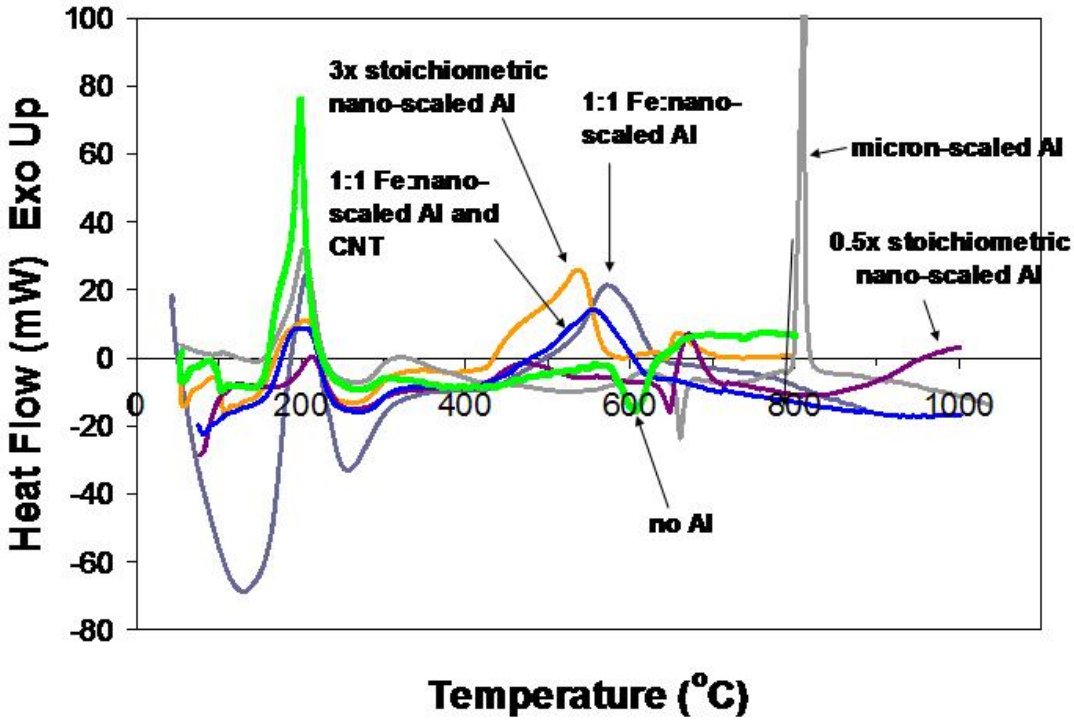

Figure 5.13: Composite figure of the DTA traces of the iron (III) oxide/aluminum systems synthesized from the gelation chemical trimethylene oxide (TMO).

Post-DTA XRD patterns again prove the existence of successful reactions as the most intense peak of elemental iron is visible. As the post-DTA XRD patterns of these samples are equivalent to the patterns for the samples synthesized from propylene oxide, the XRD patterns of the post-DTA samples are shown in Appendix A.

5.3.3.3 Characterization of other systems prepared from dimethyl oxetane

The samples synthesized from dimethyl oxetane (DMO) continue the trend of possessing heats of reaction less than those synthesized from PO, but greater than that of TMO. Figure 5.14 shows a composite graph of the DTA traces of the samples

synthesized from the gelation chemical DMO. Within the DMO system, the 1:1 Fe: nano Al sample has the highest heat of reaction at -779 J/g. The single exotherm starts at 390°C with a peak maximum of 537°C. The 3x stoichiometric quantity of Al sample again displays two exotherms, a lower temperature one that starts at 453°C with a peak maximum of 561°C and a heat of reaction of -387 J/g and a higher temperature exotherm which has a peak maximum of 690°C with a heat of reaction of -40.0 J/g. This second, higher temperature is a result of the melting of larger aggregates of aluminum particles. The one-half stoichiometric quantity of Al starts reaction at 462°C with a peak maximum at 627°C. The integrated heat of reaction for this sample is -488.6. The 1:1 Fe:nano Al sample containing carbon nanotubes has a single broad exotherm where deviation from the baseline starts at 467°C with a peak maximum at 583°C. The integrated heat of reaction for this sample is -544 J/g. The sample synthesized from DMO incorporating micron Al follow the same trend as PO. The 1:1 Fe: micron Al sample does not commence the exothermic reaction between iron (III) oxide and aluminum until 870°C with a peak maximum at 974°C. This reaction is a broad exotherm which does not start until after the micron scale aluminum particles melt with a peak temperature of 660°C.

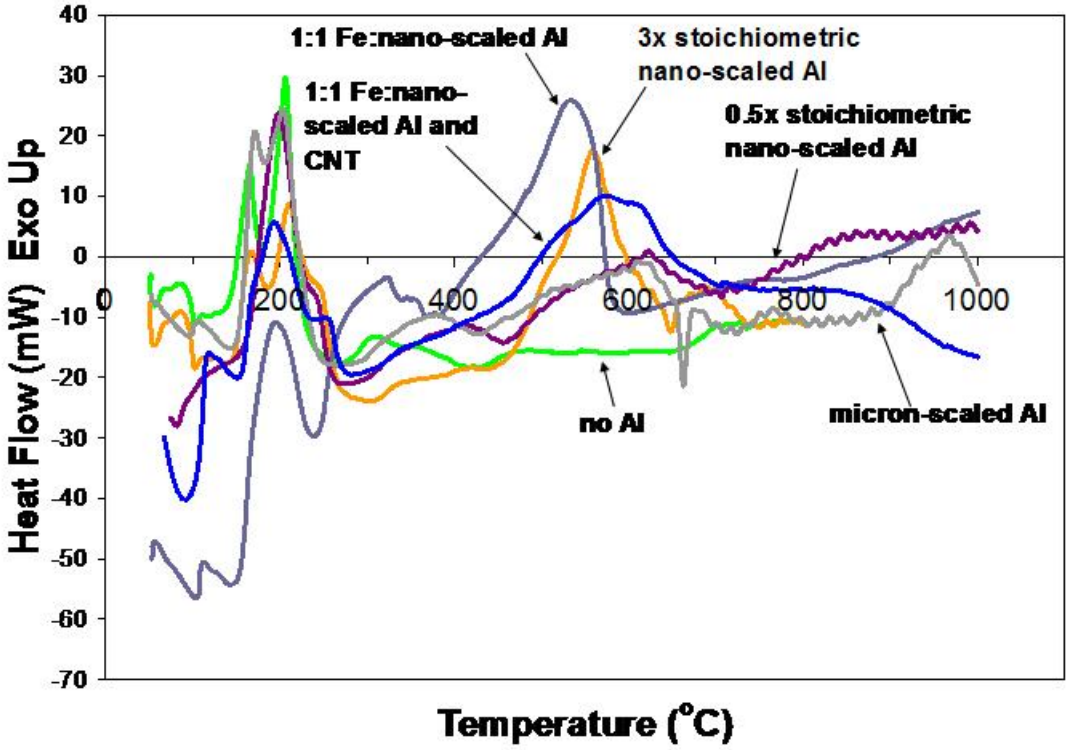

Figure 5.14: Composite figure of the DTA traces of the iron (III) oxide/aluminum systems synthesized from the gelation chemical 3,3 dimethyl oxetane (DMO).

Post-DTA XRD patterns again prove the existence of successful reactions as the most intense peak of elemental iron is visible. As the post-DTA XRD patterns of these samples are equivalent to the patterns for the samples synthesized from propylene oxide, the XRD patterns of the post-DTA samples are shown in Appendix B.

5.3.3.4 Overview of other systems prepared from PO, TMO, and DMO

The heats of reaction values are proportional to the measured surface areas of the iron (III) oxide matrices in all instances. This pertains to comparing samples with the same synthesis parameters (i.e., the Fe_2O_3(PO)/1:1 Fe:micron Al, Fe_2O_3(TMO)/1:1

Fe:micron Al, and Fe_2O_3(DMO)/1:1 Fe:micron Al). All exotherms from samples containing nano Al begin around 430°C, well below the melting point of bulk aluminum, 660°C. Within systems synthesized from the same gelation chemical, the 1:1 Fe:nano Al system has the highest heat of reaction value. The 3x stoichiometric quantity of nano Al samples have the second highest heats of reaction where these samples exhibit two exotherms, a first broad exotherm which starts around 430°C and a second exotherm which starts after aluminum aggregates melt. The micron Al containing samples do not begin reaction until after the melting point of bulk aluminum. These samples also possess much lower heat of reaction values due to the smaller interfacial surface area contact between the iron (III) oxide and aluminum particles. The addition of carbon nanotubes to the samples does not enhance heat of reaction values, but does appear to lower the activation barrier for the thermite reaction to start as the CNT containing samples customarily have slightly lower start of reaction temperatures.

5.4 Summary of Fe_2O_3/Al energetic systems

The sol-gel synthesis of Fe_2O_3/Al nanoenergetic composite materials using different epoxides as gelation agents, a 1,2 epoxide, propylene oxide, and two 1,3 epoxides, trimethylene oxide and 3,3-dimethyloxetane was studied. The sol-gel method creates a porous iron (III) oxide/hydroxide matrix in which Al particles are able to reside within those pores, creating direct interfacial contact between the Fe_2O_3 and Al particles and allowing for successful initiation of a thermitic reaction. Using the three different epoxides results in different $Fe^{(III)}{}_xO_yH_z$ matrix morphologies which directly affect the surface area contact between particles, as evidenced by surface area analysis results of the

iron (III) matrix. Transmission electron microscopy and x-ray diffraction were used to characterize the materials revealing the synthesis of an amorphous $Fe^{(III)}_xO_yH_z$ material in direct contact with crystalline Al particles for all samples which after heating in a DTA results in a successful thermite reaction with reaction products Al_2O_3 and $Fe^{(0)}$. Differential thermal analysis was used to quantify the heats of reaction for the samples showing that surface area of the Fe_2O_3 matrix is proportional to the exothermic heat of reaction for the samples due to the higher interfacial surface area contact between the Fe_2O_3 and Al particles. DTA also revealed that the onset of the thermite reaction begins before the Al particles commence melting.

Also, reactivities of other energetic systems were synthesized from PO, TMO, and DMO, including: 3x the stoichiometric quantity of nano Al, one-half the stoichiometric quantity of nano Al, 1:1 Fe:nano Al along with carbon nanotubes, 1:1 Fe:micron Al, and 1:1 Fe:micron Al containing carbon nanotubes. Overall, the heat of reaction values of the systems were proportional to measured surface area of the iron (III) oxide matrices. The 1:1 Fe:nano Al samples possessed the highest heat of reaction values, where the addition of the carbon nanotubes do not enhance the heat of reaction. The 3x Fe:nano Al and ½ Fe:nano Al samples undergo a secondary reaction after the melting of the aggregates of aluminum particles. The reactions of systems containing micron Al do not start until after the aluminum particles undergo melting. Table 5.2 summarizes the heats of reaction for the systems studied.

Table 5.2: Summary of the heat of reaction values for iron (III) oxide systems studied from gelation chemicals propylene oxide, trimethylene oxide, and 3,3 dimethyloxetane.

Sample	*Heat of Reaction (J/g)*	*Secondary Heat of Reaction (J/g)*
Fe_2O_3(PO)/1:1 nano Al	864.4	
Fe_2O_3(TMO)/1:1 nano Al	505.8	
Fe_2O_3(DMO)/1:1 nano Al	779.0	
Fe_2O_3(PO)/0.5x nano Al	554.5	29.5
Fe_2O_3(TMO)/0.5x nano Al	101.4	95.6
Fe_2O_3(DMO)/0.5x nano Al	488.6	48.8
Fe_2O_3(PO)/3x nano Al	514.7	33.3
Fe_2O_3(TMO)/3x nano Al	388.6	31.6
Fe_2O_3(DMO)/3x nano Al	387.0	40.0
Fe_2O_3(PO)/1:1 micron Al	395.6	
Fe_2O_3(TMO)/1:1 micron Al	279.9	
Fe_2O_3(DMO)/1:1 micron Al	350.3	
Fe_2O_3(PO)/1:1 nano Al CNT	689.7	
Fe_2O_3(TMO)/1:1 nano Al CNT	483.1	
Fe_2O_3(DMO)/1:1 nano Al CNT	544.0	
Fe_2O_3(PO)/1:1 micron Al CNT	470.7	

CHAPTER 6

RUTHENIUM (IV) OXIDE/ALUMINUM NANOENERGETIC MATERIALS SYSTEMS

6.1 Overview

This chapter outlines the synthesis and characterization of nanoenergetic materials synthesized from hydrous ruthenium (IV) oxide and aluminum. Section 6.2 details the synthesis and characterization of the hydrous ruthenium (IV) gels from the addition of propylene oxide to hydrated ruthenium (III) chloride solutions. Section 6.3 describes the energetic reactions of hydrous ruthenium (IV) oxide with aluminum in different atmospheres, air and argon. In conclusion, Section 6.4 summarizes the ruthenium (IV)/aluminum energetic system.

6.2 Synthesis and characterization of hydrous ruthenium (IV) oxide gels

In addition to the synthesis of iron (III) oxide materials, the sol-gel synthesis of hydrous ruthenium oxide from the addition of an epoxide, e.g. propylene oxide, to a hydrated ruthenium chloride precursor solution to generate a porous ruthenium oxide xerogel with nanoscale dimensions of the oxide particles has been studied. Despite the fact that the electronic configuration of Ru is similar to that of Fe (for example, both $Ru^{(0)}$ and $Fe^{(0)}$ have a d^8 configuration with a coordination number of 5), the chemistry of its oxides bears little resemblance to that of iron. While there is extensive chemistry

associated with the M_xO_y (M = Fe or Ru) species for both elements, the higher oxidation states of Ru are much more easily obtained than for iron.

The addition of propylene oxide to a hydrated ruthenium chloride precursor solution results in a heat-releasing reaction with the formation of a blue-black monolithic wet gel in 4 h, as compared to 25 min for the formation of an iron oxide gel from the $FeCl_3{\cdot}6H_2O$ precursor hydrous salt.[39] The slower kinetics in the formation of the ruthenium oxide nanonetwork as compared to those of iron oxide nanonetworks may result from two main differences between the chloride salts of Fe and Ru: (1) There are fewer water molecules in the coordination sphere of the ruthenium halide salt precursor, and (2) Ru(III) in the $RuCl_{3.37}{\cdot}2.5H_2O$ precursor is reduced much easier to Ru(II) in the presence of ethanol than its iron counterpart (where no such reduction takes place). Hence, the side reactions involving the Ru(III)/Ru(II) transformations have the effect of slowing down the formation of the oxide nanonetwork.

A porous xerogel of hydrous ruthenium oxide ($RuO_2{\cdot}xH_2O$) forms after residual solvents in the gel are allowed to evaporate in ambient conditions. Figure 6.1 shows a HRTEM image of the synthesized material, which reveals a porous microstructure having clusters with diameters ranging from 40-80 nm.

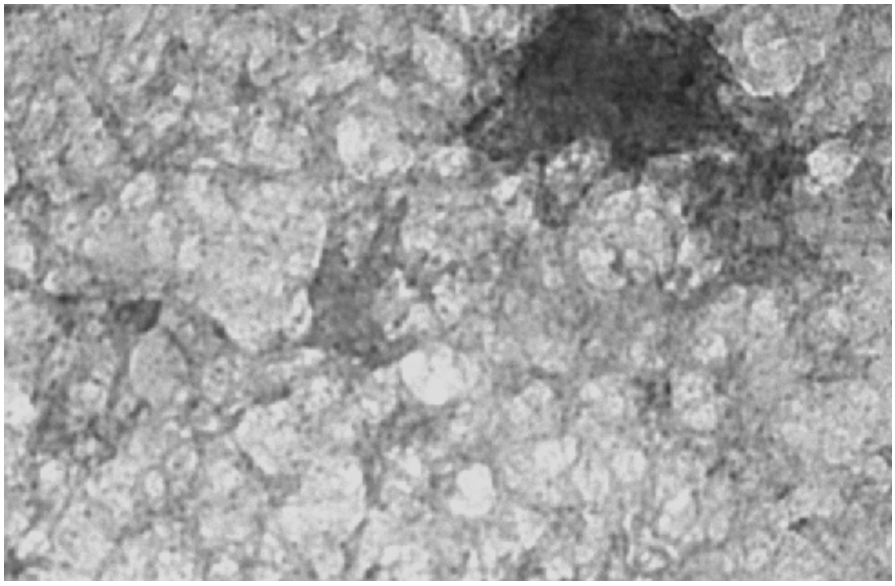

Figure 6.1: High resolution transmission electrom microscopy (HRTEM) image of the as-synthesized hydrous ruthenium oxide gel, exhibiting the presence of clusters on the order of 40-80 nm.

X-ray photoelectron spectroscopy was utilized to evaluate the composition of the ruthenium oxide material synthesized from the weak base propylene oxide. Figure 6.2(a) shows the general survey spectrum of the material. Further analysis of the XPS spectrum was performed by high-resolution scans of the C(1s)/Ru(3d) and O(1s) regions. Figure 6.2(b) shows the high-resolution C(1s)/Ru(3d) region having adjusted the C(1s) peak to 285.0 eV to compensate for the presence of charging effects in the material.[86] This region can be deconvoluted into five separate peaks, three related to the C(1s) photoelectrons and two associated with the Ru($3d_{5/2}$) and Ru($3d_{3/2}$) peaks: (A) at a binding energy (BE) of 281.7 eV corresponding to the Ru($3d_{5/2}$) peak of the material, (B) at a BE of 285.0 eV corresponding to aliphatic C–C bonding arising from residual ethanol as well as the chloropropanol and propanediol intermediates resulting from the sol-gel formation process,[39] (C) at a BE of 286.3 eV corresponding to the Ru($3d_{3/2}$) peak of the material, (D) the more electronegative C–Cl species at a binding energy of 287.5

eV originating from the chloropropanol species, and (E) at a BE of 288.7 corresponding to the C–O bonding from the same organic compounds mentioned in (A). (E) is located at the highest BE due to the highest electronegativity of oxygen. It is important to note the absence of an epoxide peak in the C(1s)/Ru(3d) high resolution scan. This is due to the fact that propylene oxide is a key component in the reaction and, unlike a traditional catalyst, it actually gets consumed during the reaction. The Ru($3d_{5/2}$) peak of the material is located at a binding energy of 281.7 eV whereas the related Ru($3d_{5/2}$) binding energy peak of elemental ruthenium is at 280.0 eV.[73] It is known that non-equivalent atoms of the same element in a solid give rise to peaks with different BE with increasing BE for increasing oxidation state.[87] The Ru($3d_{5/2}$) peak of the material is located at a higher BE than the same peak for anhydrous RuO_2, i.e. 280.7-281.0 eV,[103] due to the presence of –OH functional groups on Ru.[104] In this context, it has been reported that the Ru($3d_{5/2}$) peak for a hydrous ruthenium oxide is located at a BE of 281.4-281.8 eV.[105] Therefore, based on the analysis of the deconvolution of the Ru($3d_{5/2}$) region, it is possible to identify the synthesized material as a hydrous ruthenium oxide, $RuO_2 \cdot xH_2O$.

The O(1s) region can be deconvoluted into three peaks: (F) 529.5 eV corresponding to the lattice oxygen within the ruthenium oxide; (G) 530.8 eV corresponding to the oxygen within the chemisorbed water in $RuO_2 \cdot xH_2O$ (34); and (H) 532.5 eV corresponding to the oxygen-carbon bonding of the residual organic diol species from the synthesis as well as residual ethanol. The relative ratios between the three experimental O(1s) peaks corresponding to RuO_2, $RuO_2 \cdot xH_2O$, and O–C are 31.1:50.6:18.3, respectively. This indicates that the majority of the synthesized product (~81.7%) is a hydrated ruthenium oxide, with the balance of the sample oxygen

originating from residual organic species. The reported O(1s) peak location for a hydrated ruthenium oxide is 529.3 eV for the oxide and 530.5 for the oxygen within the adsorbed H_2O.[73] These O(1s) values are comparable to the values reported in the synthesized material here. Whereas the O(1s) peak of elemental oxygen is centered at 532.0 eV, the BE of the oxygen peak of an oxide is lower than pure oxygen – again proving the existence of a ruthenium oxide material.[90] The O(1s) region is shown in Figure 6.2(c). Also observed in the general scan of the material is the existence of the Cl(2s) and Cl(2p) peaks originating from the chloride species of the initial precursor and the chloropropanol species at BE of 269.7 eV and 199.3 eV, respectively, and the Al($2s_{1/2}$), Al($2p_{1/2}$) and Al($2p_{3/2}$) peaks originating from the Al foil used to house the powder sample in the XPS instrument. The XPS data for the as-synthesized material is summarized in Table 6.1.

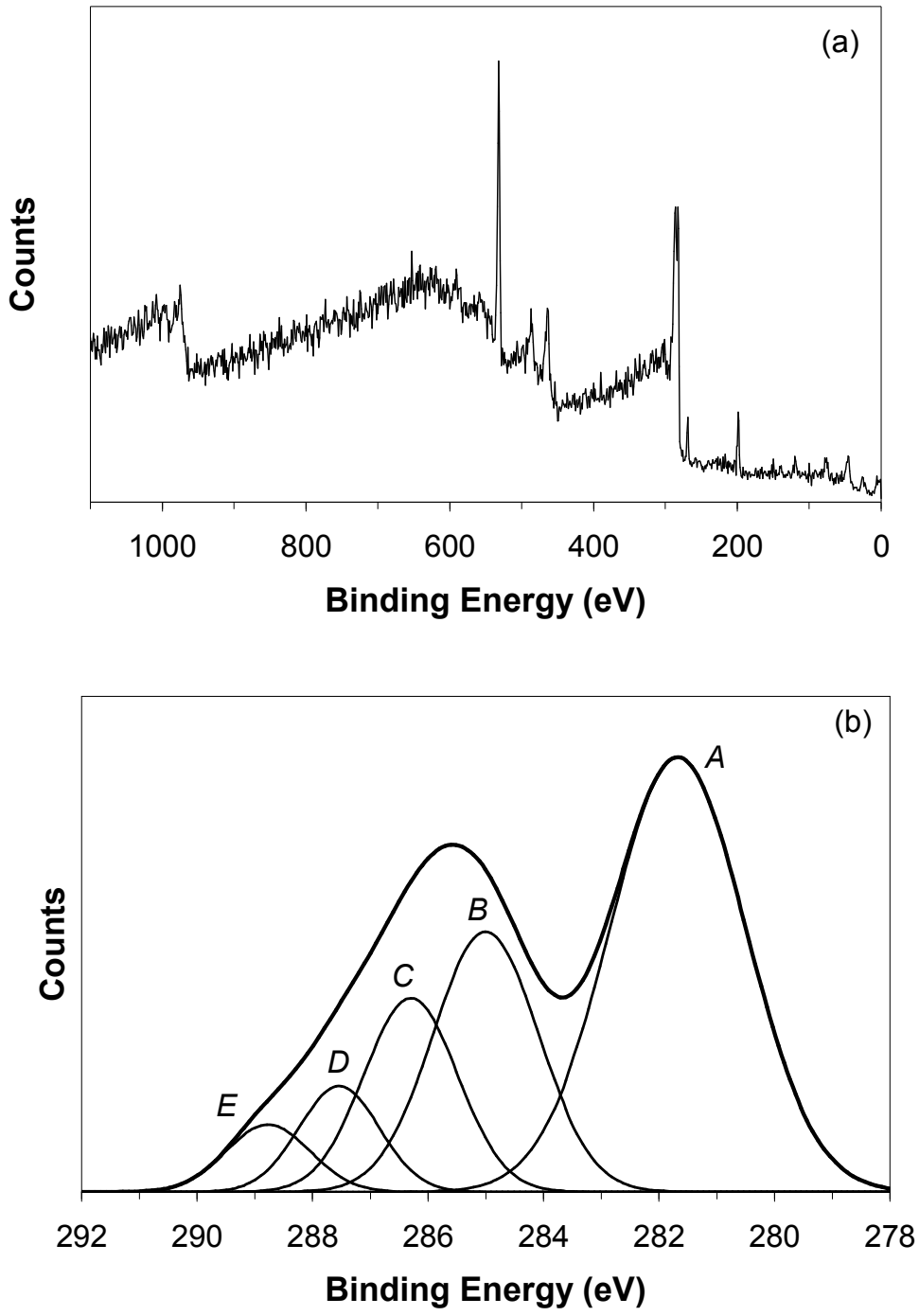

Figure 6.2**:** The x-ray photoelectron spectra (XPS) of a sol-gel synthesized hydrated ruthenium oxide from the weak base propylene oxide. (a) The general scan of the oxide material. (b) The high resolution C(1s)/Ru(3d) core level electrons and its deconvolution into five peaks. (c) The O(1s) core level emission spectrum and its deconvolution into three peaks.

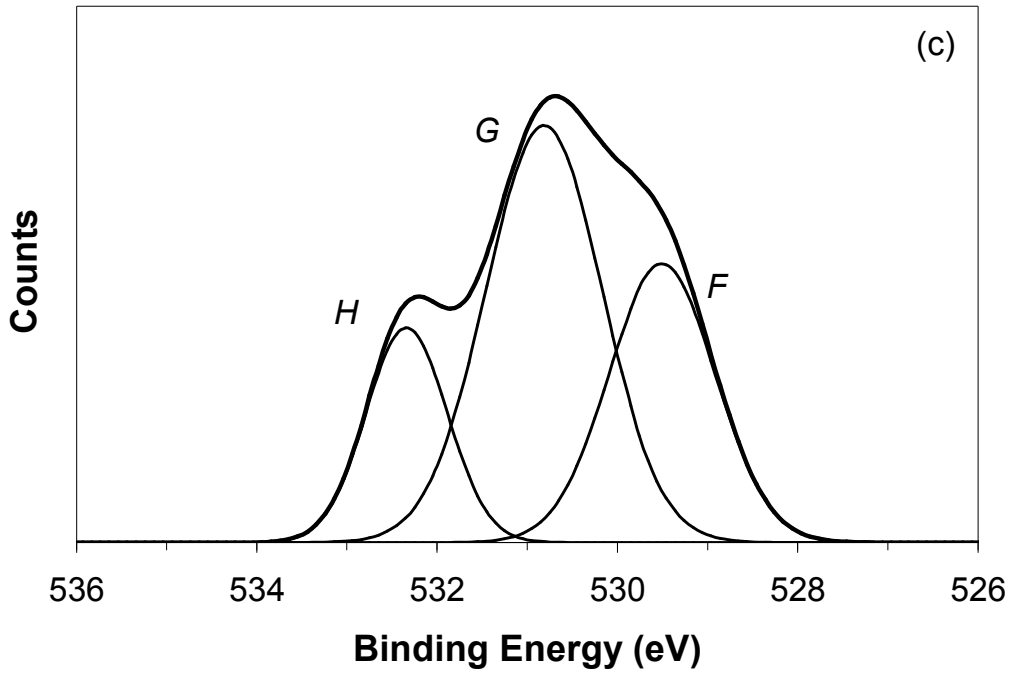

Figure 6.2 continued

Table 6.1: The binding energies, full-width half-maximum values, percentage of total peak area, and assignment of atoms of the x-ray photoemission spectrum (XPS) of the O(1s) and C(1s)/Ru(3d) core electron regions for a hydrous ruthenium oxide sample synthesized by the sol-gel process from propylene oxide, corresponding to Figure 6.2.

Peak Label	BE (eV)	FWHM (eV)	% of Total Area	Assignment of Atoms
		C 1s/Ru 3d		
A	281.7	2.77	49.7%	**Ru $3d_{5/2}$**
B	285.0	2.15	23.1%	**C**-C
C	286.3	1.91	15.2%	**Ru $3d_{3/2}$**
D	287.5	1.64	7.2%	**C**-Cl
E	288.7	1.71	4.7%	**C**-O
		O 1s		
F	529.5	1.39	31.1%	Ru**O_2**
G	530.8	1.51	50.6%	$RuO_2 \cdot x\,H_2$**O**
H	532.5	1.06	18.3%	**O**-C

Figures 6.3 and 6.4 show x-ray diffraction data for the as-synthesized sample as well as patterns for the sample after various heat treatments. Figures 6.3(a) and 6.3(b) display the diffraction pattern of the as-prepared gel and the gel heated to 125°C for 2 hours under nitrogen, respectively. These patterns show that the synthesized material is amorphous with crystallization not occurring until temperatures greater than 125°C. Figure 6.3(c) shows the diffraction pattern of a gel specimen heated to 250°C and held for 2 hours under nitrogen. The onset of low levels of crystallinity may be observed at this temperature, generating broad peaks in the vicinity of Bragg angles of 38°, 44°, and 70°. Figure 6.3(d) shows the XRD pattern of a sample heated to 550°C at 10°C/min under nitrogen using a DSC. At this temperature, the material exhibits a higher degree of crystallinity with peaks at 38.43°, 42.21°, 44.11°, 58.52°, 69.48°, 78.53°, and 84.75°. The broad peaks in Figures 6.3(c) and 6.3(d) are indicative of the presence of zero-valent ruthenium metal, while the peaks listed in Figure 6.3(d) correspond directly and unequivocally to the (1 0 0), (0 0 2), (1 0 1), (1 0 2), (1 1 0), (1 0 3), (1 1 2), and (2 0 1) planes of $Ru^{(0)}$, respectively. Figure 6.3(e) shows the continued trend of the complete reduction process of the hydrated ruthenium oxide material to ruthenium metal in an inert atmosphere when heated to 1400°C. Figures 6.3(f) and 6.3(g) show the diffraction patterns for $Ru^{(0)}$ and RuO_2. Ji et al. have stated that the reduction of hydrous ruthenium oxide to ruthenium metal is due to the presence and affinity of chloride ions, which are generated from the ruthenium chloride precursor salt involved in the sol-gel reaction, to act as intramolecular reducing agents, as shown in Equation 8.[105]

$$Ru^{IV}O_2 \cdot xH_2O + 4Cl^- \xrightarrow{\Delta, InertGas} Ru^{(0)} + 2Cl_2 + 2O^{-2} \qquad (8)$$

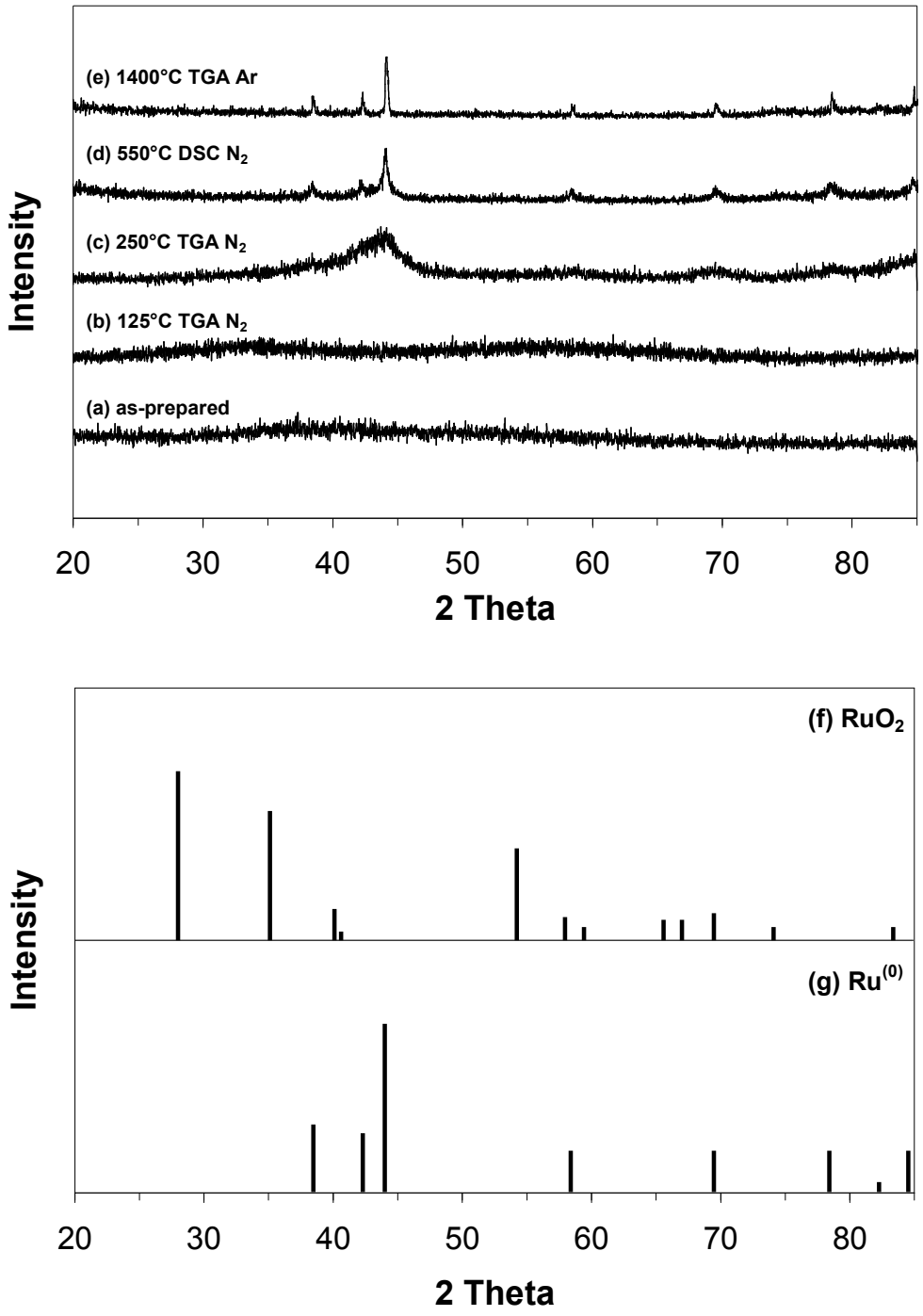

Figure 6.3: X-ray diffraction (XRD) patterns of the sol-gel synthesized hydrous ruthenium oxide samples heated in inert atmospheres to (a) room temperature, (b) 125°C, (c) 250°C, (d) 550°C, and (e) 1400°C and published diffraction patterns for (f) anhydrous RuO_2 and (g) $Ru^{(0)}$.

Pagnaer et al. have postulated also the possibility that the organic matrix, stemming from the organic solvent and gelation agent, is oxidized during heating, forming carbon monoxide, which is another potential reducing agent, as shown in Equation 9.[106]

$$Ru^{IV}O_2 \cdot xH_2O + 2CO \xrightarrow{\Delta, InertGas} Ru^{(0)} + 2CO_2 \qquad (9)$$

The reduction of the ruthenium oxide that ensues at temperatures below 250°C is most likely due to the thermodynamically-driven propensity of ruthenium oxide to decompose to the zero-valent state under low oxygen partial pressure, as is the case within the instrument housings of the TGA and DSC under inert gas purging. Hence, a possible reaction sequence that could account for the products observed in this sol-gel reaction is as follows:

$$4Ru^{III}Cl_3 \cdot xH_2O \xrightarrow{EtOH, \mathrm{Pr}opyleneOxide, Air} Ru^{(0)} + 3Ru^{IV}O_2 \cdot xH_2O \qquad (10)$$

$$RuO_2 \cdot xH_2O(s) \xrightarrow{\Delta, InertGas} Ru^{(0)}(s) + O_2(g)\uparrow \qquad (11)$$

As shown in Equation 10, Ru^{III} undergoes disproportionation to $Ru^{(0)}$ and Ru^{IV}. The absence of oxygen, or the low oxygen partial pressure during heating cycles under inert atmosphere, destabilizes the ruthenium oxide compound and drives the reduction reaction shown in Equation 11. The presence of $Ru^{(0)}$ immediately upon the completion of the sol-gel reaction, as indicated by Equation 10, cannot be confirmed because of three main reasons: (1) the ambiguity in the assignment of the XPS peaks, due to the overlap of

the $Ru(3d_{5/2})$ and $Ru(3d_{3/2})$ regions with those of C(1s), (2) the very large FWHM of the 281.7 eV band assigned to $Ru(3d_{5/2})$, which could also be deconvoluted into an additional band in the vicinity of 280.0 eV corresponding to $Ru^{(0)}$, and (3) the amorphous character of the product that does not afford any conclusion based on the x-ray diffraction below 125 °C.

Indirect evidence of the initial formation of $Ru^{(0)}$ from the sol-gel reaction may be obtained when examining the behavior of the product mixture upon heating in air. Whereas heating the sample in an inert environment results in the complete reduction of the hydrated ruthenium oxide to the zero-valent state, heating the sample in air results in the formation of an anhydrous ruthenium oxide material. However, the presence of zero-valent Ru upon heating is still observed under certain conditions. Figure 6.4(a) shows the XRD pattern of the as-prepared amorphous material and Figure 6.4(b) shows the sample heated to 300°C for 20 hours in air, where the peaks corresponding to anhydrous ruthenium oxide begin to emerge. Broad peaks can be seen at Bragg angles of 28.4°, 35.3°, 44.2°, 54.4°, and 69.7°. The first three of these peaks match the most intense peaks of anhydrous RuO_2 corresponding to the (1 1 0), (1 0 1), and (2 1 1) planes. Figure 6.4(c) shows an XRD pattern of the material heated at 600°C for 20 hours in air showing a more crystalline RuO_2. However, peaks related to zero-valent ruthenium clearly remain in these patterns. Figure 6.4(d) displays the XRD pattern of the sample heated at 10°C/min under air to a temperature of 1400°C. It is not until this temperature that the complete oxidation of all ruthenium within the sample occurs resulting in a pure anhydrous ruthenium oxide, shown in Equation 12:

$$Ru^{(0)} \xrightarrow{O_2} Ru^{IV}O_2 \qquad (12)$$

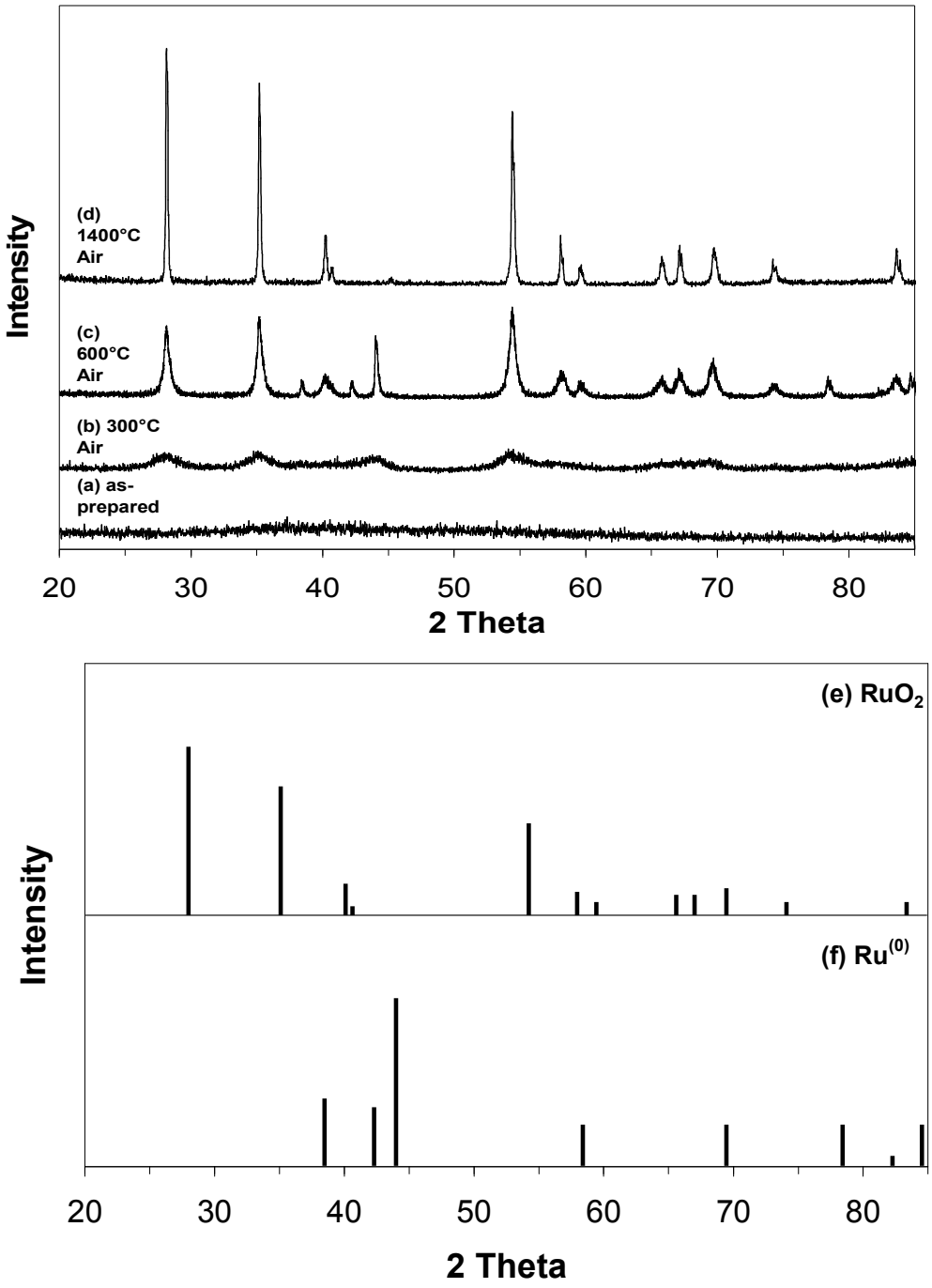

Figure 6.4: X-ray diffraction (XRD) patterns of the sol-gel synthesized hydrous ruthenium oxide samples heated in air at (a) room temperature, (b) 300°C, (c) 600°C, and (d) 1400°C and published diffraction patterns for (e) anhydrous RuO_2 and (f) $Ru^{(0)}$.

Another possible explanation for the presence of $Ru^{(0)}$ in the samples is that some of the surface oxygen atoms in the samples heated in air to 300°C and 600°C, generated by the thermodynamic instability of the ruthenium oxide with increased temperature, may have desorbed due to the lack of a sufficient supply of atmospheric oxygen to replenish the lost oxygen. This decomposition results in a $Ru^{(0)}$ surface and bulk anhydrous RuO_2, resulting in the presence of both phases in the XRD patterns. However, the sample heated to 1400°C in the TGA is able to replenish the surface oxygen liberated from this high-temperature thermal decomposition due to a continuous source of oxygen flowing over the sample surface, maintaining a high oxygen partial pressure and prohibiting this spontaneous decomposition, thus resulting in a single phase material, anhydrous RuO_2, as seen in the XRD pattern.

This change in material composition after heating the sample to different temperatures under different atmospheres can be further evaluated using thermo-gravimetric analysis (TGA) profiles. Figure 6.5 shows the changes in the mass fraction of the two samples as they are heated under two different atmospheres, air and argon. Both samples lose a substantial fraction of their mass up to ~270°C. The sample heated in air loses ~45% and the sample heated in argon loses ~55% of their respective total weights. This loss is attributed to loss of adsorbed water in the material as well as the loss of residual organics remaining from the initial ambient drying procedure. For the sample heated in an inert atmosphere, weight loss essentially ceases at this temperature until 1400°C. Similarly to XPS and XRD data, the TGA results also confirm that the as-prepared hydrous ruthenium oxide is reduced to the zero-valent state when heated in an

inert atmosphere. If the weight loss data in both atmospheres, air and argon, is normalized between the temperatures 300°C and 1000°C (the temperature range where almost no weight loss is observed), a simple weight ratio of Ru metal to RuO_2 (0.76) is equal to the normalized ratio of the weights of the samples heated in argon and air (0.77). This value shows that the sample heated in argon does not have the associated weight of the two oxygens in RuO_2 and the additional 10% weight loss below 300°C can be considered a result of the liberation of oxygen formerly coordinated with the oxide. Also, at 1400°C, the total remaining weight percent is 37.8%. This corresponds well to the total weight percent of 35.5% of ruthenium of the synthesized material found by elemental analysis. Therefore, the sample heated in argon can be considered $Ru^{(0)}$ and the sample heated in air RuO_2.

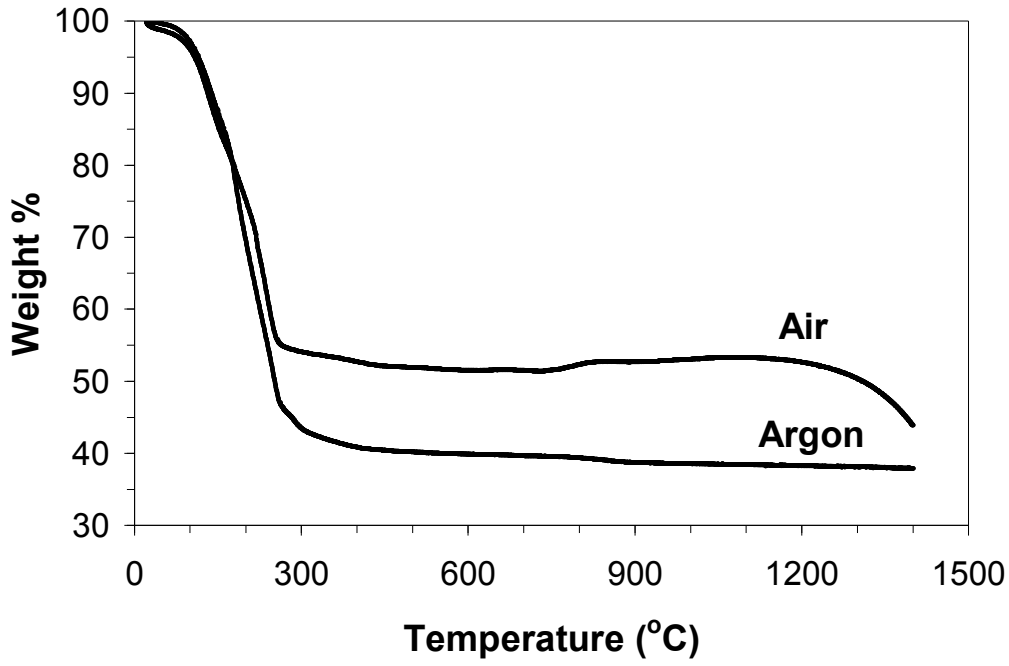

Figure 6.5: Thermogravimetric analysis (TGA) thermal profile for the decomposition of hydrated ruthenium oxide samples heated to 1400°C at a heating rate of 10°C/min in two different atmospheres, air and argon.

Above 300°C, the weight loss of the sample heated in air is minimal until 1000°C, at which point a drastic drop in weight is seen. This weight loss can be explained as spontaneous decomposition of the oxide at a temperature greater than 600°C as the ruthenium-oxygen bonds break, and the oxygen is liberated as O_2.[107] This decomposition may also explain the existence of $Ru^{(0)}$ in the XRD patterns of the samples heated in air, but not in the TGA, due to a deficiency of a continuous flow of oxygen that could drive the thermodynamic equilibrium towards the oxide, as shown in Equation 13:

$$RuO_2 \xrightarrow{T > 600^oC} Ru(s) + O_2(g)\uparrow \qquad (13)$$

This high temperature weight loss can also be explained by the reactions that occur when RuO_2 is heated in the presence of oxygen, as shown in Equations 14 and 15:[73]

$$RuO_2(s) + O_2(g) \xrightarrow{T \approx 800^o C} RuO_4(g) \qquad (14)$$

$$RuO_2(s) + \frac{1}{2}O_2(g) \xrightarrow{T > 1000^o C} RuO_3(g) \qquad (15)$$

In these reactions, higher valency gaseous ruthenium oxide species form on the surface of the sample and are eventually purged from the sample, resulting in a decrease in sample weight at high temperatures. $RuO_3(g)$ is the dominant species found at temperatures greater than 1000°C and $RuO_4(g)$ is dominant around 800°C.[73] As the sample heated in argon does not show a decrease in sample weight above 1000°C, neither

the ruthenium-oxygen bond decomposition nor the high temperature formation of higher valency gaseous ruthenium oxide species occurs, indicating a complete absence of oxygen in the system and, therefore, the sole existence of $Ru^{(0)}$.

Figure 6.6 shows the differential thermal analysis (DTA) data of the samples heated in air and argon from room temperature to 1400°C. Both samples display small endotherms below 150°C resulting from the loss of water.[63] The sample heated in air displays a sharp exotherm at 250°C due to crystallization of the as-synthesized amorphous material and a broad exotherm starting at 300°C due to a continued increase in crystallinity of the sample over the entire temperature range. The sample heated in argon displays a smaller exotherm at 235°C due to the competing endothermic decomposition of the hydrous oxide to $Ru^{(0)}$ with the exothermic crystallization of these zero-valent atoms in this temperature range. As with the sample heated in air, a broad exotherm beginning at 300°C can be seen. Its magnitude is smaller due to an overall lower level of crystallization. This relative increase in crystallinity for samples in both atmospheres is confirmed by the corresponding XRD patterns.

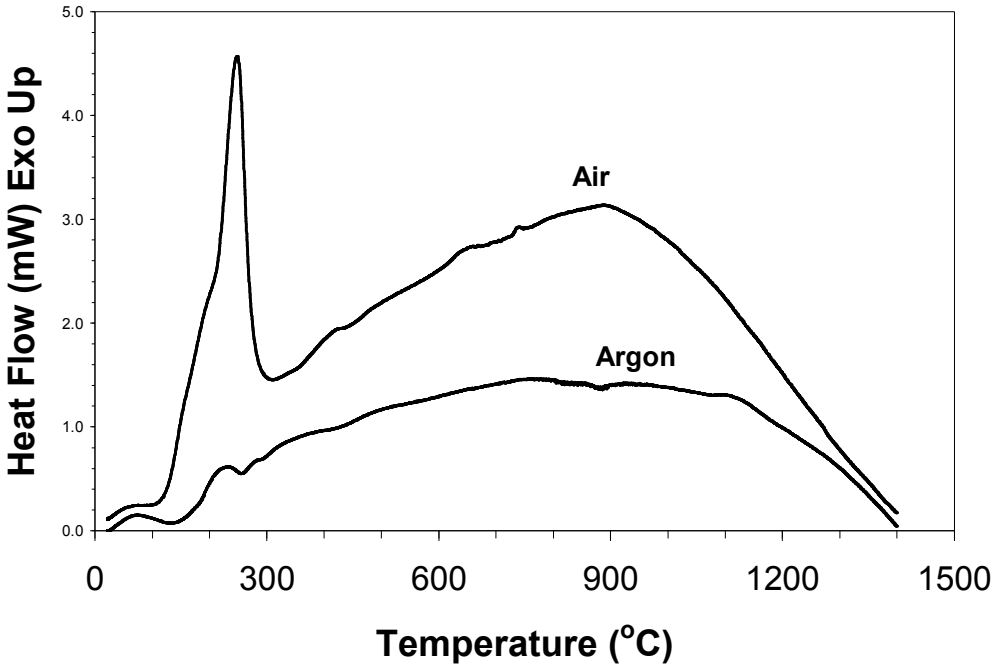

Figure 6.6: Differential thermal analysis (DTA) data for the synthesized hydrous ruthenium oxide heated at 10°C/min to 1400°C in two different atmospheres, air and argon.

6.3 Characterization of hydrous ruthenium (IV) oxide/aluminum energetic systems

6.3.1 Synthesis Results

The addition of propylene oxide to a hydrated ruthenium chloride and nano-scale aluminum precursor solution results in a heat-releasing reaction with the formation of a blue-black monolithic wet gel in 4 hours. Figure 6.7 shows a representative HRTEM image of the $RuO_2 \cdot xH_2O$/Al synthesized material. The image reveals an interconnected microstructure of individual ruthenium oxide particles of 3-5 nm forming clusters with diameters ranging from 40-80 nm in direct contact to spherical Al particles with diameter of 25-60 nm.

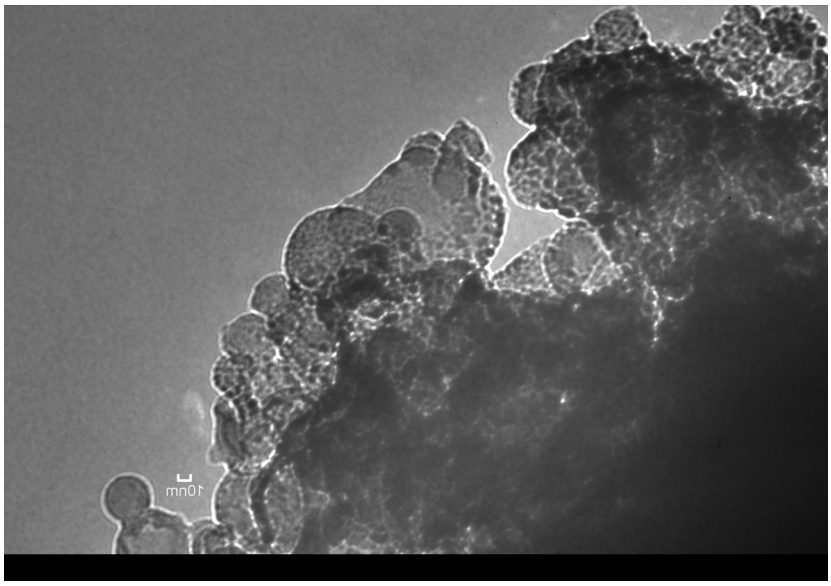

Figure 6.7: HRTEM image showing interconnected individual hydrous RuO_2 particles (3-5 nm) in direct contact with spherical Al particles (25-60 nm).

Figure 6.8 shows the XRD pattern of the sample synthesized with 0.083 g Al. Peaks can be found at Bragg angles of 38.56°, 44.80°, 65.22°, and 78.50°. These peaks directly correspond to elemental aluminum, and the (1 1 1), (2 0 0), (2 2 0), and (3 1 1) planes, respectively. The absence of additional peaks demonstrates the amorphous character of the hydrous ruthenium oxide, which has been previously examined. Also, the absence of Al_2O_3 peaks shows the Al particles did not appreciably oxidize during synthesis or processing.

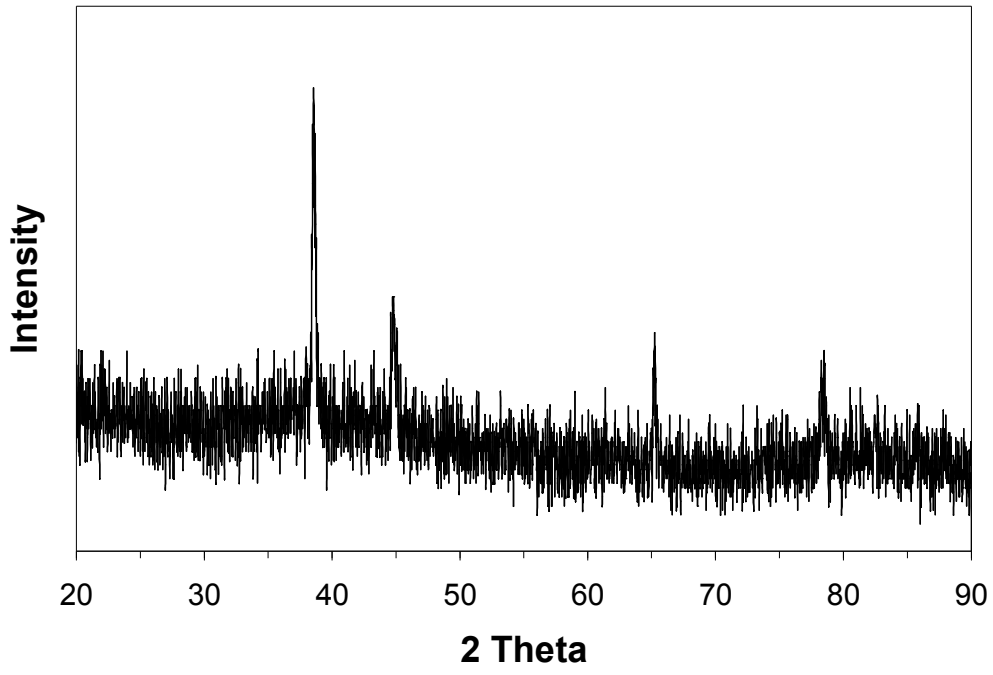

Figure 6.8: XRD pattern of the synthesized hydrous RuO_2/Al material using sol-gel chemistry. Peaks are located at Bragg angles of 38.56°, 44.80°, 65.22°, and 78.50°, corresponding to elemental Al. The lack of additional peaks demonstrates the amorphous character of the hydrous ruthenium oxide.

6.3.2 Heating the hydrous ruthenium oxide/Al gels under inert conditions

The four synthesized gels with varying Al concentrations (0.083 g, 0.064 g, 0.027 g, and no Al) were heated in a DTA at 10°C/min using argon as the purge gas at a flow rate of 20.00 mL/min. Figure 6.9 shows the DTA traces for the samples. In general, each trace is similar with small endotherms around 100°C corresponding to the loss of water. Exotherms around 200°C correspond to the crystallization of the amorphous ruthenium oxide. Endotherms around 300°C show the decomposition of the oxide into elemental Ru, as previously discussed in section 6.2. Finally, there is the existence of exotherms in the range of 450°C to 625°C for the three Al-containing samples. As there is no exotherm in this vicinity for the non-Al containing sample, this indicates that this corresponds to

the exothermic reaction of the Ru and Al particles.[108] This exotherm is the result of a solid-state reaction as the reaction occurs below the melting point of both constituents.[109] The melting point of Al is 660.5°C and the melting point of Ru is 2334°C.[100] The integrated heats of reaction for the three samples containing Al were calculated: (a) -500 J/g for the $RuO_2 \cdot xH_2O$/0.083 g Al sample, (b) -288 J/g for the $RuO_2 \cdot xH_2O$/0.064 g Al sample, and (c) -25.5 J/g for the $RuO_2 \cdot xH_2O$/0.027 g Al sample. Here it can be seen that the heat of reaction is proportional to the initial concentration of Al within the samples. Figure 6.10 displays this exotherm in greater detail.

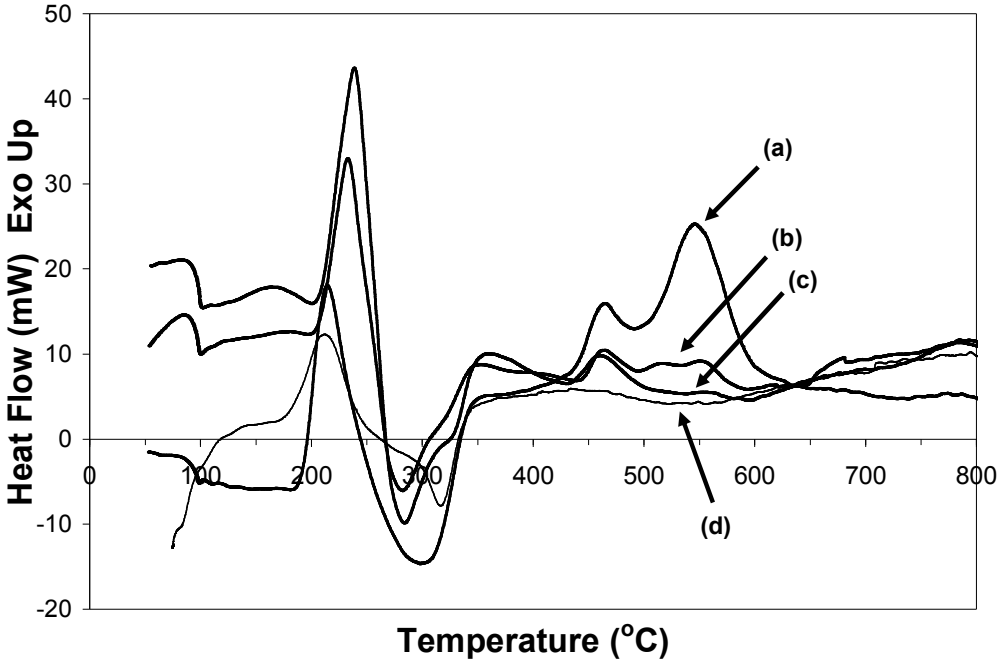

Figure 6.9: DTA traces of the synthesized $RuO_2 \cdot xH_2O$/Al gels heated at 10°C/min using argon as the purge gas. Note the crystallization exotherms around 200°C, the endothermic decomposition around 300°C, and the exotherms in the range of 450°C-625°C for the samples (a) $RuO_2 \cdot xH_2O$/0.083g Al, (b) $RuO_2 \cdot xH_2O$/0.064 g Al, (c) $RuO_2 \cdot xH_2O$/0.027 g Al, and (d) no Al.

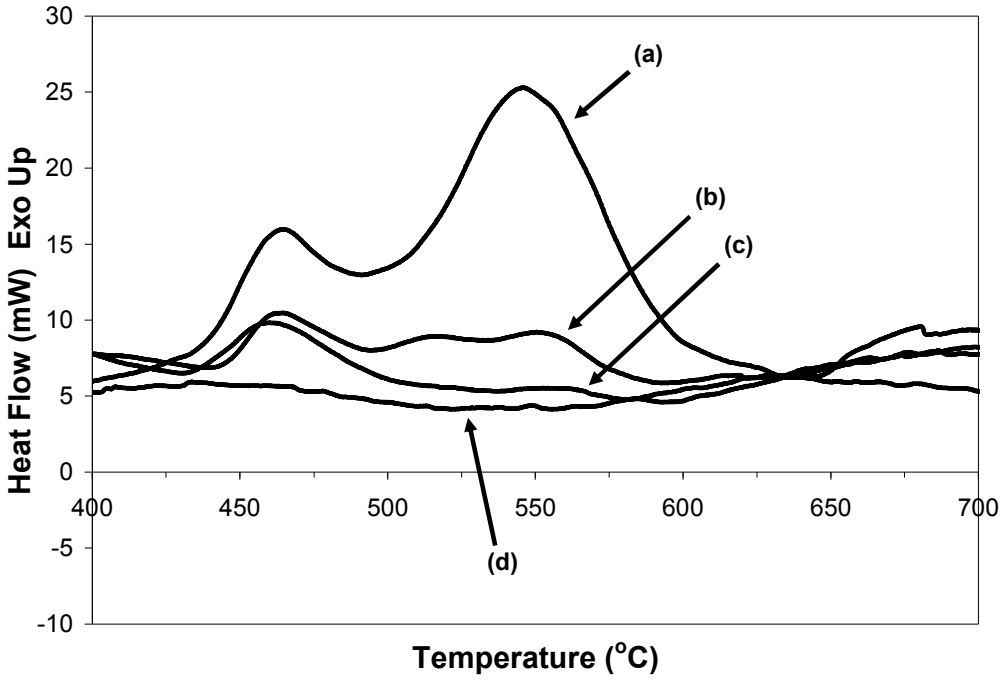

Figure 6.10: Expanded view of the DTA exotherm for the samples heated under argon in the vicinity of 450°C-625°C of (a) $RuO_2 \cdot xH_2O$/0.083g Al, (b) $RuO_2 \cdot xH_2O$/0.064 g Al, (c) $RuO_2 \cdot xH_2O$/0.027 g Al, and (d) $RuO_2 \cdot xH_2O$/no Al.

To analyze the products formed after the samples were heated to 1000°C under argon, x-ray diffraction patterns were taken of the samples after the heat treatment. Previous studies have shown that heating the $RuO_2 \cdot xH_2O$ sample without Al under argon to 1000°C results in the complete reduction of the original hydrous ruthenium oxide material to elemental ruthenium, $Ru^{(0)}$. Figure 6.11(a) shows the pattern of the $RuO_2 \cdot xH_2O$/0.083g Al sample where the amorphous character of the as-synthesized material has transformed into a material of higher crystallinity. Analysis of the diffraction pattern reveals the formation of the intermetallic $RuAl_2$ as well as the most intense reflection of elemental Ru. The formation of the intermetallic establishes that the original hydrous RuO_2 has been completely reduced to Ru metal before reaction with the Al particles, as seen in the DTA trace. Also, the specific formation of the intermetallic

$RuAl_2$ is expected, as the atomic fraction of Ru to Al from the original precursors is 33% (again this value was calculated using the elemental analysis data of the as-purchased Ru (III) chloride salt which has an exact molecular weight of 265.6 g/mol). From a published Ru/Al phase diagram, this ratio of Ru to Al will result in the formation of the intermetallic phase $RuAl_2$.[83] This phase diagram is seen in Figure 6.12. Also, due to non-stoichiometric concentrations of Ru to Al, a small quantity of unreacted Ru is seen in the diffraction pattern. Figure 6.11(b) shows the diffraction pattern of the $RuO_2 \cdot xH_2O$/0.064g Al sample after heating in argon to 1000°C in a DTA. Here, the diffraction pattern can be seen to contain the phases $RuAl_2$, Ru_2Al_3, and Ru. The atomic fraction of Ru to Al in this sample is 40%. This fraction on the experimentally constructed Ru/Al phase diagram corresponds to Ru_2Al_3, however here we report the formation of the intermetallics Ru_2Al_3 and $RuAl_2$, neighboring phases on the phase diagram. Again, excess elemental Ru can be seen in the diffraction pattern. Figure 6.11(c) shows the diffraction pattern of the $RuO_2 \cdot xH_2O$/0.027g Al sample. Here, the most intense peaks of the intermetallic RuAl can be seen along with excess elemental Ru. The atomic fraction of Ru to Al for this sample is 61%, which corresponds well to phase diagram information. Figures 6.11(d)-6.11(h) show the theoretical diffraction patterns for $RuAl_2$, Ru_2Al_3, RuAl, $Ru^{(0)}$, and RuO_2, respectively.

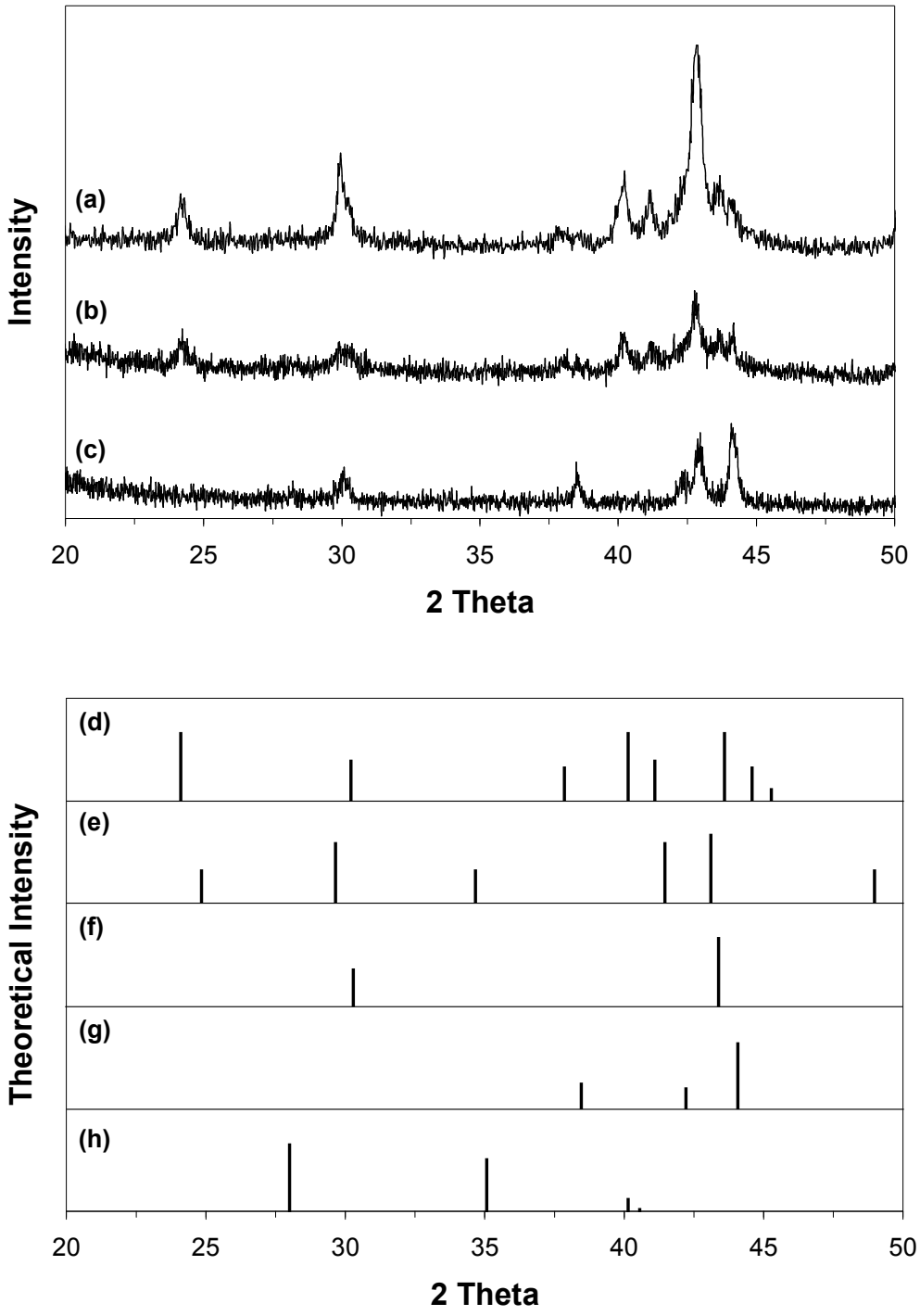

Figure 6.11: XRD patterns of post-DTA $RuO_2 \cdot xH_2O$/Al samples heated to 1000°C under argon at 10°C/min for (a) $RuO_2 \cdot xH_2O$/0.083 g Al, (b) $RuO_2 \cdot xH_2O$/0.064 g Al, and (c) $RuO_2 \cdot xH_2O$/0.027 g Al. Also, the theoretical diffraction patterns are shown for (d) $RuAl_2$, (e) Ru_2Al_3, (f) RuAl, (g) $Ru^{(0)}$, and (h) anhydrous RuO_2.

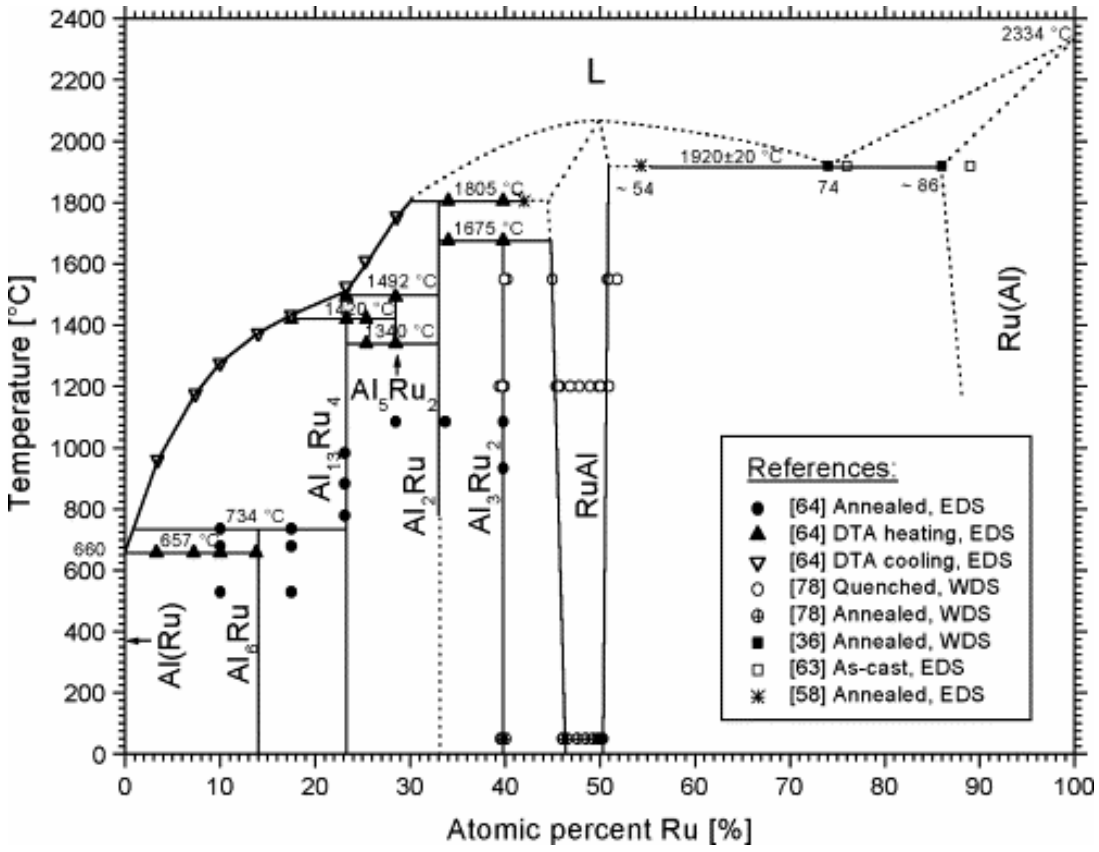

Figure 6.12: Phase diagram of the Ru/Al system.[83]

The heating of $RuO_2 \cdot xH_2O$/Al samples within the chamber of a DTA using argon as the purge gas results in the formation of Ru_xAl_y intermetallics of varying stoichiometries. The stoichiometry is directly related to the ratio of Ru atoms from the original hydrated ruthenium chloride salt to the number of Al atoms added to the solution. Also, the intensity of the (1 0 1) plane for Ru, the most intense peak, increases as the quantity of Al decreases. It should be noted that none of the samples containing Al match the diffraction pattern of anhydrous RuO_2.

6.3.3 Heating the hydrous ruthenium (IV) oxide/Al gels in air

The three samples containing Al ($RuO_2 \cdot xH_2O$/0.083 g Al, $RuO_2 \cdot xH_2O$/0.064 g Al, and $RuO_2 \cdot xH_2O$/0.027 g Al), as well as the sample not containing Al were heated in a DTA at 10°C/min using an air purge at 20.00 mL/min. Figure 6.13 shows the DTA traces of these samples. Again, general statements can be made for the samples. Small endotherms around 100°C can be seen corresponding to the loss of water; large, broad exotherms in the range of 100°C to 300°C correspond to crystallization of the amorphous material; and small exotherms around 400°C again correspond to crystallization. Yet again, exotherms of varying intensities in the range of 450°C-625°C can be seen for the aluminum containing samples where the sample without Al does not show this exotherm, thus indicating a reaction with the Al particles. There is a direct relationship between the amount of Al in the sample and the related integrated heat of reaction of this exotherm. The $RuO_2 \cdot xH_2O$/0.083g Al sample possesses an integrated heat of reaction of -1,199 J/g, the $RuO_2 \cdot xH_2O$/0.064g Al sample has a heat of reaction of -1,059 J/g, and the $RuO_2 \cdot xH_2O$/0.027g Al sample has a heat of reaction of -392 J/g. Figure 6.14 displays this region of the DTA trace in greater detail for the aluminum and non-aluminum containing samples.

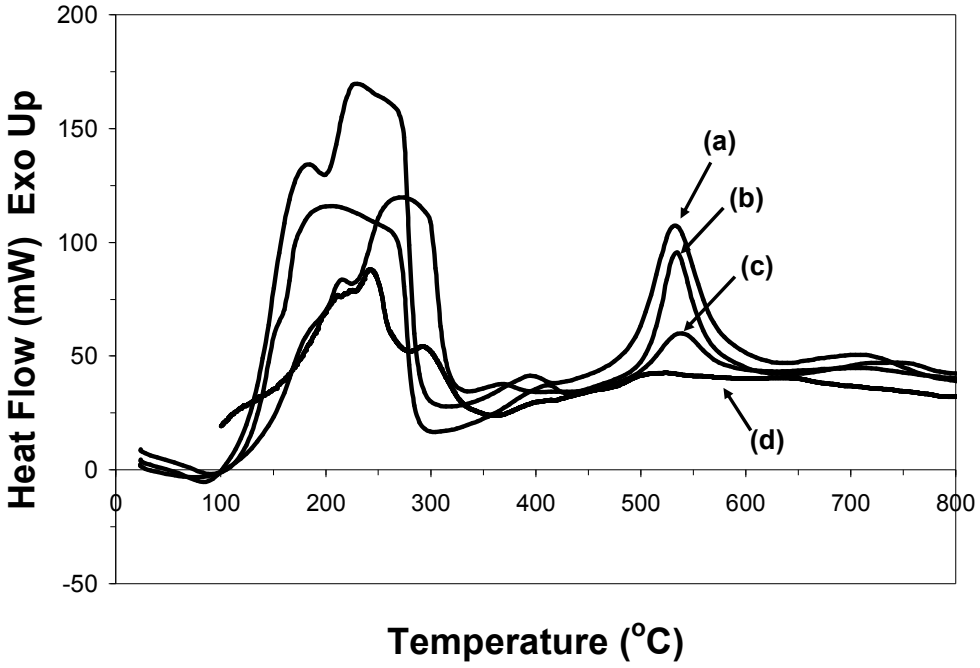

Figure 6.13: DTA trace of $RuO_2 \cdot xH_2O$ samples synthesized from sol-gel chemistry heated to 1000°C at 10°C/min in air containing different concentrations of Al particles: (a) 0.083 g Al, (b) 0.064 g Al, (c) 0.027g Al, and (d) no Al.

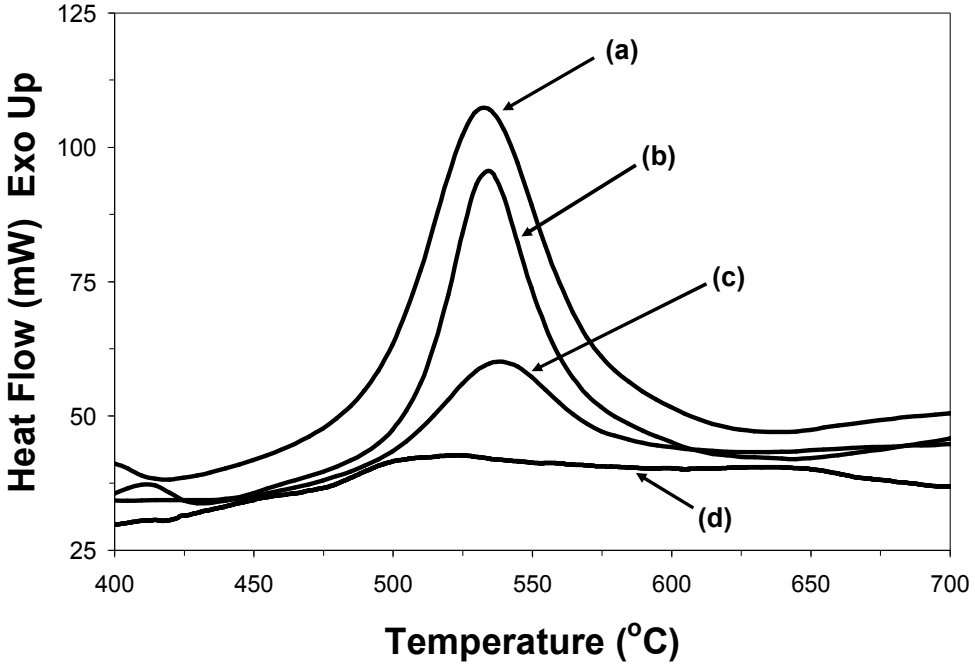

Figure 6.14: Expanded view of the DTA exotherm for the samples heated in air in the vicinity of 450°C-625°C for (a) $RuO_2 \cdot xH_2O$/0.083g Al, (b) $RuO_2 \cdot xH_2O$/0.064 g Al, (c) $RuO_2 \cdot xH_2O$/0.027 g Al, and (d) $RuO_2 \cdot xH_2O$/no Al.

Figure 6.15 shows the post-DTA x-ray diffraction patterns for the samples. Previous work has shown that the sol-gel synthesized $RuO_2 \cdot xH_2O$ loses adsorbed water and transforms into crystalline RuO_2 when heated in air in a DTA to 1000°C. Figure 6.15(a) shows the XRD pattern for the $RuO_2 \cdot xH_2O$/0.083g Al sample. Analysis of the pattern reveals that after heating to 1000°C, the sample possesses increased crystallinity and can be identified as entirely anhydrous RuO_2. Figures 6.15(b) and 6.156(c) show that the other two Al containing post-DTA samples also reveal the sole existence of anyhydrous RuO_2 in their respective diffraction patterns. A similar loss of Al during reaction has been reported previously.[109] With the traditional Fe_2O_3/Al thermite reaction, the reaction products are Al_2O_3 and Fe arising from the oxidation-reduction reaction.

Here we are possibly witnessing an analogous thermite reaction. The RuO_2 and Al phases are reacting in such a manner that there is a complete disappearance of the Al phase from the sample. The combustion temperature is the maximum temperature reached during the exothermic reaction in the formation of intermetallics.[110] It was reported that the combustion temperature in the formation of RuAl increased as Ru particle size decreased in the micron-scale. If this trend continued, it is possible that the increased reduction in Ru particle size to the nano-scale could increase the combustion temperature to a value high enough to essentially vaporize the Al particles resulting in the sole existence of Ru based products. Also, a detailed analysis of the XRD patterns shows that the peaks are consistently shifted to higher diffraction angles indicating a possible formation of a solid solution in which the aluminum particles are imbedded within the RuO_2 matrix.

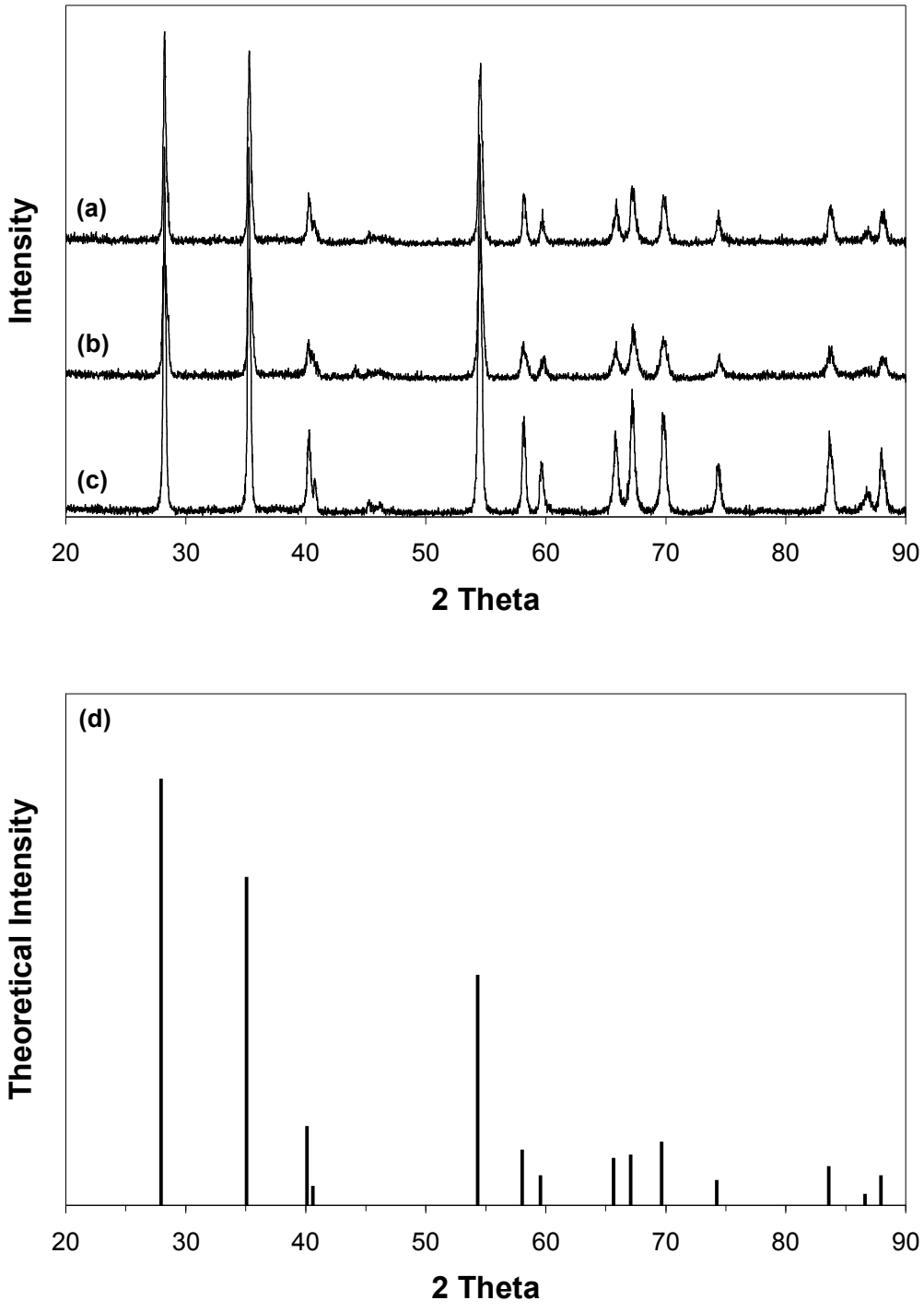

Figure 6.15: X-ray diffraction patterns of the (a) $RuO_2 \cdot xH_2O$/0.083g Al, (b) $RuO_2 \cdot xH_2O$/0.064g Al, and (c) $RuO_2 \cdot xH_2O$/0.027g Al samples heated at 10°C/min in air in a DTA. Phase analysis confirms all samples are anhydrous RuO_2, as demonstrated by the theoretical x-ray diffraction pattern of RuO_2 shown in (d).

To study the exotherm in the temperature range of 450°C to 625°C, the $RuO_2 \cdot xH_2O$/0.083g Al sample was heated in a DTA at 10°C/min in air to 430°C, a temperature slightly less than the temperature the exotherm commences. Figure 6.16(a) shows the resulting x-ray diffraction pattern of this sample. Analysis of this diffraction pattern reveals the existence of the most intense reflections of both anhydrous RuO_2 and Al, as shown by the theoretical diffraction patterns for these phases in Figures 6.16(b) and 6.16(c), respectively. The data confirms that this exotherm corresponds to the reaction of RuO_2 and Al, the two phases present just as the reaction starts.

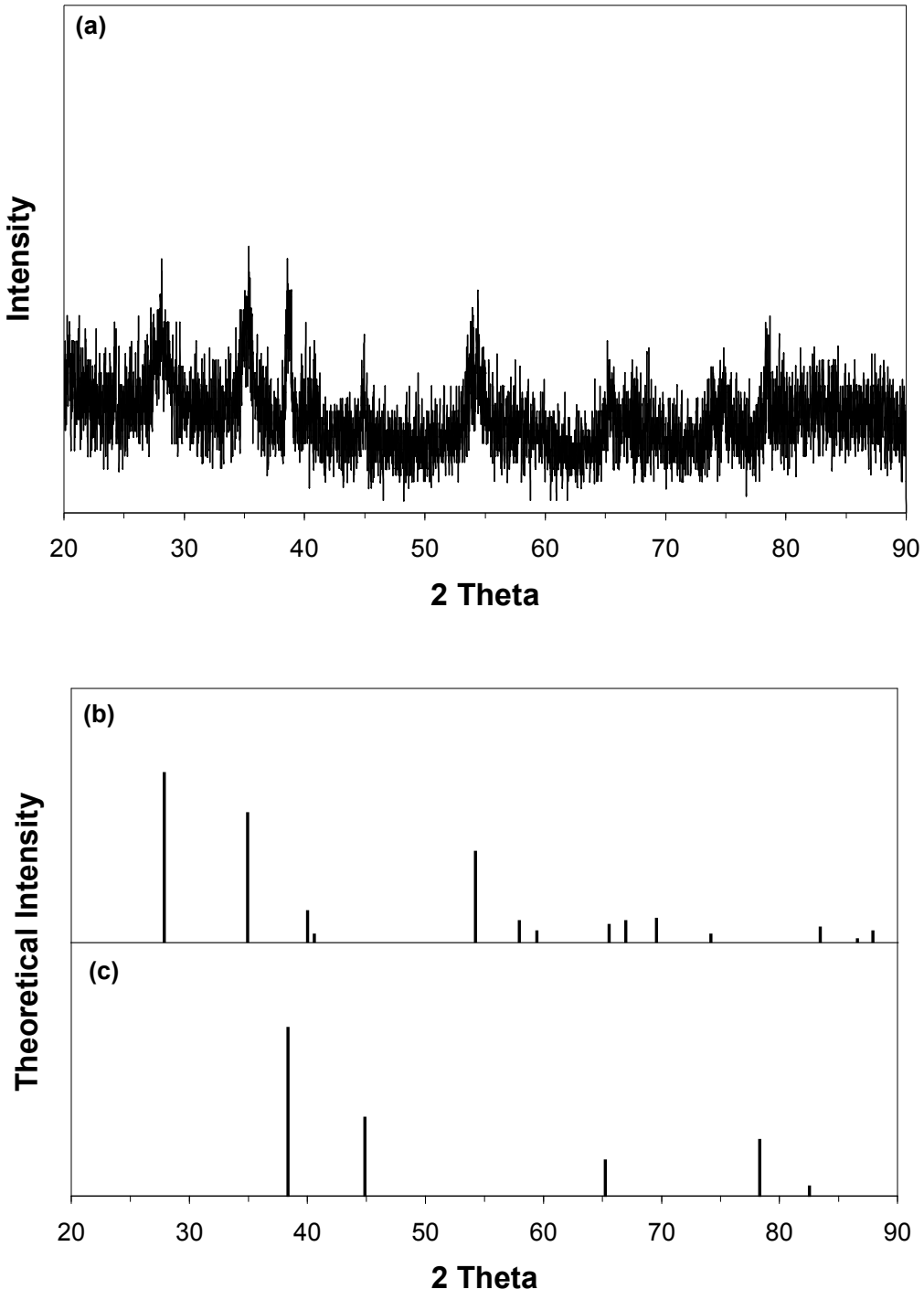

Figure 6.16: (a) X-ray diffraction pattern of the $RuO_2 \cdot xH_2O$/0.083g Al sample heated at 10°C/min to 430°C in air using a DTA. Theoretical x-ray diffraction patterns for (b) anhydrous RuO_2 and (c) Al.

6.4 Summary of hydrous RuO_2/Al energetic systems

Hydrous ruthenium oxide ($RuO_2 \cdot xH_2O$) xerogels were synthesized through the addition of a 1,2 epoxide, propylene oxide, to hydrated ruthenium chloride, $RuCl_3 \cdot xH_2O$, in ethanol. After a blue-black monolithic gel formed in 4 hours, the samples were allowed to age for 24 hours and were dried in ambient conditions. The dried samples were then characterized by XPS, XRD, DTA and TGA. XPS showed the Ru($3d_{5/2}$) peak at a binding energy of 281.7 eV, corresponding to that of hydrous ruthenium oxide. XRD data revealed the synthesized material as amorphous, with heating the sample in inert atmospheres causing complete reduction of the oxide to the zero-valent state whereas heating the sample in air resulting in both crystalline anhydrous RuO_2 and zero-valent ruthenium, depending on the method of heating. DTA traces show an endotherm ending at 150°C corresponding to the loss of coordinated water as well as two higher temperature crystallization exotherms when the sample is heated in both inert and oxygen-rich atmospheres. TGA runs also confirmed the complete reduction of the hydrous oxide when heated in nitrogen below 270°C and the formation of anhydrous ruthenium oxide when heated in air, confirming the XRD results.

Characterization of the RuO_2/Al nanoenergetic samples display major differences and some similarities have been identified when comparing the $RuO_2 \cdot xH_2O$/Al samples of varying Al concentration heated in the different atmospheres of argon and air. From DTA traces, all samples in both environments show endotherms below 100°C due to the loss of water, crystallization exotherms in the temperature region of 200°C, and reaction exotherms in the temperature range of 450°C to 625°C. Differences, however, outweigh

the similarities. The samples heated in argon show an endotherm at 300°C corresponding to the reduction of the crystalline RuO_2 to $Ru^{(0)}$. This reduction results in the reaction of elemental Ru and Al to form intermetallics of varying stoichiometries. The stoichiometry specifically depends on the original concentration of Al in the sample. The samples heated in air do not encounter this reduction to elemental Ru, thereby the reaction occurs between RuO_2 and Al. However, post-DTA XRD patterns show the sole existence of anhydrous RuO_2 with the absence of Al.

Also, the integrated heat of reaction for the reaction between the Ru and Al species is dependent on the original aluminum concentration from synthesis. In general, the more Al present in the sample before reaction, the higher the heat of reaction. This generality holds for the samples heated in air and argon. However, in comparing the heats of reaction for the samples heated in both environments, the samples heated in air had heats of reaction greater than two times that of the samples heated in argon.

CHAPTER 7

OVERALL ENERGETIC COMPARISON OF THE IRON (III) OXIDE/ALUMINUM AND RUTHENIUM (IV) OXIDE/ALUMINUM SYSTEMS

7.1 Overview

This chapter presents a summary of the reactions that were studied for the iron (III) oxide/aluminum and ruthenium (IV) oxide/aluminum energetic systems presented in this work.

7.2 Overall energetic comparison of the Fe_2O_3/Al and RuO_2/Al systems

The aluminum-containing iron (III) oxide and ruthenium (IV) oxide energetic systems presented in this work possess a wide range of heats of reaction. Table 7.1 provides a summary of the reactions studied in this work, including: sample designation, heat of reaction, secondary heat of reaction, if applicable, peak temperature of reaction(s), and reaction products. The secondary heats of reaction correspond to exothermic reactions occurring after aggregations of nano-scale aluminum particles melt, enabling a second reaction between the iron (III) oxide and aluminum phases. Reaction products were all confirmed by x-ray diffraction. From this table, specific materials systems can be selected for specific applications based on the heat required and the synthesis conditions.

Table 7.1: Summary of all reactions of the Fe_2O_3/Al and RuO_2/Al systems presented in this work.

Sample	*Heat of Reaction (J/g)*	*Secondary Heat of Reaction (J/g)*	*Peak Temperature of Reaction(s) (°C)*	*Reaction Products*
$RuO_2 \cdot x\ H_2O$/0.083 g Al (air)	-1199.0		534	RuO_2
$RuO_2 \cdot x\ H_2O$/0.064 g Al (air)	-1059.0		534	RuO_2
$Fe^{(III)}_xO_yH_z$(PO)/1:1 nano Al	-864.4		567	Al_2O_3, Fe
$Fe^{(III)}_xO_yH_z$(DMO)/1:1 nano Al	-779.0		538	Al_2O_3, Fe
$Fe^{(III)}_xO_yH_z$(PO)/1:1 nano Al CNT	-689.7		565	Al_2O_3, Fe
$Fe^{(III)}_xO_yH_z$(PO)/0.5x nano Al	-554.5	-29.5	553, 745	Al_2O_3, Fe
$Fe^{(III)}_xO_yH_z$(DMO)/1:1 nano Al CNT	-544.0		576	Al_2O_3, Fe
$Fe^{(III)}_xO_yH_z$(PO)/3x nano Al	-514.7	-33.3	514, 668	Al_2O_3, Fe, excess Al
$Fe^{(III)}_xO_yH_z$(TMO)/1:1 nano Al	-505.8		570	Al_2O_3, Fe
$RuO_2 \cdot x\ H_2O$/0.083 g Al (argon)	-500.0		465, 547	$RuAl_2$, $Ru^{(0)}$
$Fe^{(III)}_xO_yH_z$(DMO)/0.5x nano Al	-488.6	-48.8	627, 760	Al_2O_3, Fe
$Fe^{(III)}_xO_yH_z$(TMO)/1:1 nano Al CNT	-483.1		557	Al_2O_3, Fe
$Fe^{(III)}_xO_yH_z$(PO)/1:1 micron Al CNT	-470.7		821	Al_2O_3, Fe
$Fe^{(III)}_xO_yH_z$(PO)/1:1 micron Al	-395.6		969	Al_2O_3, Fe
$RuO_2 \cdot x\ H_2O$/0.027 g Al (air)	-392.0		539	RuO_2
$Fe^{(III)}_xO_yH_z$(TMO)/3x nano Al	-388.6	-31.6	541, 664	Al_2O_3, Fe, excess Al
$Fe^{(III)}_xO_yH_z$(DMO)/3x nano Al	-387.0	-40.0	562, 690	Al_2O_3, Fe, excess Al
$Fe^{(III)}_xO_yH_z$(DMO)/1:1 micron Al	-350.3		971	Al_2O_3, Fe
$RuO_2 \cdot x\ H_2O$/0.064 g Al (argon)	-288.0		465, 554	$RuAl_2$, Ru_2Al_3, $Ru^{(0)}$
$Fe^{(III)}_xO_yH_z$(TMO)/1:1 micron Al	-279.9		809	Al_2O_3, Fe
$Fe^{(III)}_xO_yH_z$(TMO)/0.5x nano Al	-101.4	-95.6	479, 676	Al_2O_3, Fe
$RuO_2 \cdot x\ H_2O$/0.027 g Al (argon)	-25.0		462, 555	RuAl, $Ru^{(0)}$

CHAPTER 8

CONCLUSIONS

This work has detailed the synthesis of nanoenergetic materials through sol-gel chemistry for the Fe_2O_3/Al and RuO_2/Al systems. In addition to thermal analysis of the exothermic reactions, characterization of the as-synthesized and post-reaction samples was performed by diffraction, imaging, and spectroscopic techniques. Also, mechanistic elucidation of the sol-gel epoxide addition synthesis was studied in order to verify a proposed 'proton scavenging' mechanism.

Elucidation of the 'proton scavenging' mechanism

The intent of the work was to continue the study on the published theory of the sol-gel synthesis of iron (III) oxide/hydroxide materials characterized by the addition of a weak base epoxide, propylene oxide, to an iron nitrate solution. Two epoxides, propylene oxide and tetrahydrofuran, and a heterocyclic nitrogen compound, pyridine, have been successfully used in the synthesis of porous iron (III) oxide-based materials. X-ray photoelectron spectroscopy, x-ray diffraction, infrared spectroscopy, transmission electron microscopy and atomic force microscopy have been used to characterize the new materials. Detailed analysis of XPS data has revealed the formation of an iron (III) oxide/hydroxide in each of the three individual syntheses. TEM and AFM images show a naturally porous surface structure with individual nanoscale $Fe^{(III)}{}_xO_yH_z$ clusters. The broadening of peaks in the x-ray diffraction pattern was also consistent with the

nanocrystalline nature of the particles that were formed. In addition to synthesizing new materials from other weak bases, reaction mechanisms have been proposed stemming from a 'proton scavenging' mechanism. Mechanistically, the 'proton scavenging' mechanism is indeed relevant for all three syntheses. The epoxides, i.e. propylene oxide and tetrahydrofuran, scavenge protons from the hydrated iron complexes to form protonated epoxides, which are then irreversibly ring-opened to form diols. Pyridine also reacts with the hydrated iron complexes, extracting protons, to form the protonated pyridinium ion. Reaction mechanisms were confirmed by pH, XPS, and infrared spectroscopy data.

Fe_2O_3/Al nanoenergetic materials systems

The intent of the work was to study and expand upon the sol-gel synthesis of Fe_2O_3/Al nanoenergetic composite materials using different epoxides as gelation agents, a 1,2 epoxide, propylene oxide, and two 1,3 epoxides, trimethylene oxide and 3,3-dimethyloxetane. The sol-gel method creates a porous iron (III) oxide/hydroxide matrix in which Al particles are able to reside within those pores, creating direct interfacial contact between the Fe_2O_3 and Al particles and allowing for successful initiation of a thermitic reaction. Using the three different epoxides results in different $Fe^{(III)}{}_xO_yH_z$ matrix morphologies which directly affect the surface area contact between iron (III) oxide and aluminum particles, as evidenced by surface area analysis results of the as-synthesized iron (III) matrix. Transmission electron microscopy and x-ray diffraction were used to characterize the materials revealing the synthesis of an amorphous $Fe^{(III)}{}_xO_yH_z$ material in direct contact with crystalline Al particles for all samples, which, after heating in a DTA, result in a successful thermite reaction with reaction products

Al_2O_3 and $Fe^{(0)}$. Differential thermal analysis was used to quantify the heats of reaction for the samples showing that surface area of the Fe_2O_3 matrix is proportional to the exothermic heat of reaction for the samples due to the higher interfacial surface area contact between the Fe_2O_3 and Al particles. DTA also revealed that the onset of the thermite reaction begins before the Al particles commence melting.

Iron (III) oxide matrices were synthesized from propylene oxide (PO), trimethylene oxide (TMO), and 3,3 dimethyl oxetane (DMO), to which other materials were added to study their energetic characteristics. These included 1:1 Fe:nano Al, 3x the stoichiometric quantity of nano Al, ½ the stoichiometric quantity of nano Al, 1:1 Fe:nano Al plus the addition of carbon nanotubes (CNT), 1:1 Fe: micron Al, and 1:1 Fe: micron Al plus CNT. After heating these samples in a DTA to 1000°C, the exothermic outputs were tabulated. The PO-synthesized samples, with the greatest oxide matrix surface area available for contact with aluminum particles, consistently had the highest heat of reaction values. DMO-prepared samples, with the second highest oxide matrix surface area, had the second highest heat of reaction values for its samples. TMO samples, with the smallest oxide matrix surface area for the oxidant and fuel particles to contact, had the lowest heat of reaction values.

Within each gelation chemical system, the 1:1 Fe:nano Al consistently had the highest integrated heat of reaction values. The 3x nano Al and ½ nano Al samples had two exotherms, a primary exotherm accounting for ~90% of the magnitude of the exotherm corresponding to the solid-state reaction between the iron (III) oxide and aluminum particles, and a secondary reaction due to the melting of unreacted aluminum and iron oxide particles. This secondary exotherm arises from an increase in diffusion of

the aluminum particles in the liquid state to react with the iron (III) oxide particles. Also, the addition of carbon nanotubes to the syntheses does not enhance reaction output. Whereas samples synthesized with nano-scale aluminum particles start the exothermic thermite reaction at ~430°C, the samples synthesized with micron-scale aluminum did not react until ~800°C, after the aluminum particles melt at ~660°C.

RuO_2/Al nanoenergetic materials systems

The intent of this work was to study the sol-gel synthesis of hydrous ruthenium oxide from the addition of a 1,2 epoxide to a hydrated ruthenium chloride solution. After verifying that gelation successfully occurs 4 hours after the addition of the epoxide, characterization of the material was carried out by XPS, XRD, DTA, and TGA. Through deconvolution of the C(1s)/Ru(3d) region, XPS established that the synthesized gel material was a hydrous ruthenium oxide, $RuO_2 \cdot xH_2O$, which also contains residual organic species not removed during the drying process. After heating the hydrous ruthenium oxide in inert and oxygen-containing atmospheres to temperatures up to 1400°C, evaluation of the XRD patterns showed that the as-prepared material was amorphous and samples heated in inert atmospheres were completely reduced to $Ru^{(0)}$ below 250°C. XRD patterns of samples heated in air revealed the existence of anhydrous RuO_2 as well as $Ru^{(0)}$, unless a continuous supply of oxygen was present in the system to maintain a high oxygen partial pressure to thermodynamically maintain the oxide as the stable phase. DTA traces show an endothermic loss of water below 150°C, with exotherms for samples heated in both air and argon due to crystallization. The lower temperature exotherm of the sample heated in argon is smaller than the corresponding

sample heated in air due to the competing endothermic decomposition of the hydrous oxide into ruthenium metal and oxygen gas in the same temperature interval. TGA data also illustrates that the synthesized material contained approximately 45% organic material by weight which is evolved below 250°C with the complete reduction of the original material to $Ru^{(0)}$ below 250°C for the sample heated in argon. Also, the TGA trace demonstrates that the sample heated in air becomes an anhydrous ruthenium oxide by this same temperature with high temperature weight loss due to the well-known formation of gaseous higher valency ruthenium oxide species as well as high temperature thermal decomposition of the RuO_2 species into ruthenium metal and oxygen gas.

Energetic samples were synthesized with varying concentrations of nano-scale aluminum ($RuO_2 \cdot xH_2O$/0.083 g Al, $RuO_2 \cdot xH_2O$/0.064 g Al, $RuO_2 \cdot xH_2O$/0.027 g Al, and $RuO_2 \cdot xH_2O$/no Al). These samples were heated in a DTA to 1000°C in different atmospheres, air and argon. For the samples heated in argon, the $RuO_2 \cdot xH_2O$ matrix is completely reduced to $Ru^{(0)}$ before reaction with the aluminum particles where the integrated heats of reaction for these samples are proportional to the initial concentration of aluminum. Post-DTA XRD patterns show the formation of crystalline intermetallics. The stoichiometry of the Ru_xAl_y intermetallic formed depends on the ratio of Ru:Al from the original syntheses, as determined by the Ru/Al phase diagram.

The RuO_2/Al energetic samples heated in air start reaction at ~430°C. Again, heats of reaction values for these samples are proportional to the initial aluminum concentration with higher quantities of aluminum having higher heat of reaction values. Post-DTA x-ray diffraction patterns for all the samples heated in air show the sole

existence of anhydrous RuO_2, the diffraction peaks for Al are absent in the patterns. This is due to the reaction in air producing enough heat to essentially vaporize the Al particles.

Overall energetic comparison of synthesized samples

In comparing the Fe_2O_3/Al and RuO_2/Al systems heated in air and argon, the RuO_2/0.083 g Al sample heated in air has the highest heat of reaction value at -1,199 J/g. The RuO_2/0.027 g Al sample heated in argon has the lowest heat of reaction value at -25 J/g. Between these two values is presented a wide variety of heat of reaction values.

CHAPTER 9

RECOMMENDATIONS

This research project was successful in confirming a sol-gel synthesis mechanism where weak base molecules, propylene oxide, tetrahydrofuran, and pyridine, induce gelation of an iron (III) salt aqueous solution. XRD, XPS pH, and IR data were instrumental in determining reaction mechanisms for these molecules. Utilizing other weak base molecules as gelation chemicals and determining their respective reaction mechanisms would establish if they also follow the 'proton scavenging' mechanism. Also, times to gelation are presented for the Fe_2O_3 and RuO_2 systems; however, no definitive study on the kinetics of time to reaction is presented. A kinetic study on the gelation of hydrated metal salt would be instrumental in ensuring the proper time to add the fuel component to the sol to keep the fuel particles well-distributed within the metal oxide matrix, a key variable in maximizing heat of reaction values. The study would involve how the metal salt anion, metal salt concentration, concentration of water within the sol, and gelation chemical effect gelation time. Another vital component recommended studying in the synthesis of energetic materials with differing metal oxide matrix morphologies is to examine how the gelation chemical produces specific metal oxide morphology. In this study, using the gelation chemicals propylene oxide and trimethylene oxide, for example, produce very different oxide matrices with different matrix surface area values. When the fuel component is added to the metal oxide matrix

with different geometries, different reaction heats can be expected, therefore it is possible to control the heat output from a specific system.

For characterization of the energetic materials, fuels other than aluminum could be studied, e.g. tantalum, as well as using smaller diameter aluminum particles to study how that effects heat of reaction values. Also, it is recommended to continue to study the exothermic reaction of other Group 8 metal oxide matrices with similar electronic configurations, e.g. osmium oxide, with fuel particles. As the Fe_2O_3/Al systems were studied using different gelation chemicals to produce different iron (III) oxide matrix morphologies, the same study on the effect of heat of reaction on gelation chemical should be completed on the RuO_2/Al system. Most importantly, it is recommended to study the Fe_2O_3/Al systems heated in air. The current study heated the samples in argon, which possibly could suppress full reaction potential, as seen with the RuO_2/Al systems heated in argon having lower heat of reaction values compared to those heated in air.

APPENDIX A

X-ray Diffraction Patterns of Other Systems Synthesized from the Gelation Chemical Trimethylene Oxide (TMO)

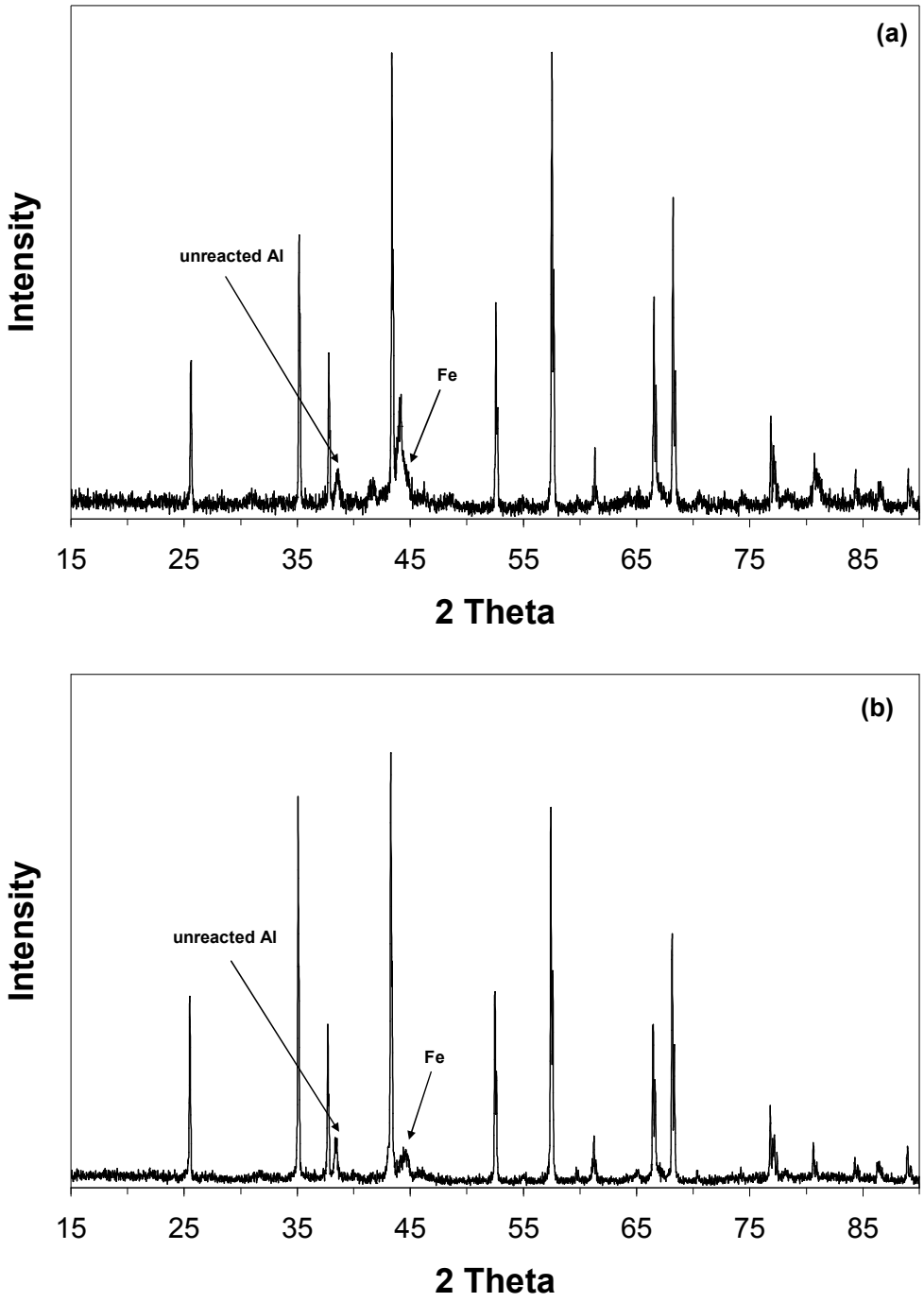

Figure A.1: XRD patterns of other iron (III) oxide/aluminum systems heated in a DTA to 1000°C at 10°C/min using trimethylene oxide as the gelation chemical. (a) Fe_2O_3/3x stoichiometric ratio of Fe:nano Al (3 x 0.083 g = 0.249 g Al), (b) Fe_2O_3/½ stoichiometric ratio of nano Al (½ x 0.083 g = 0.0415 g), (c) Fe_2O_3/1:1 Fe nano Al plus CNT, (d) Fe_2O_3/1:1 Fe:micron Al, and (e) Fe_2O_3/1:1 Fe:micron Al plus CNT.

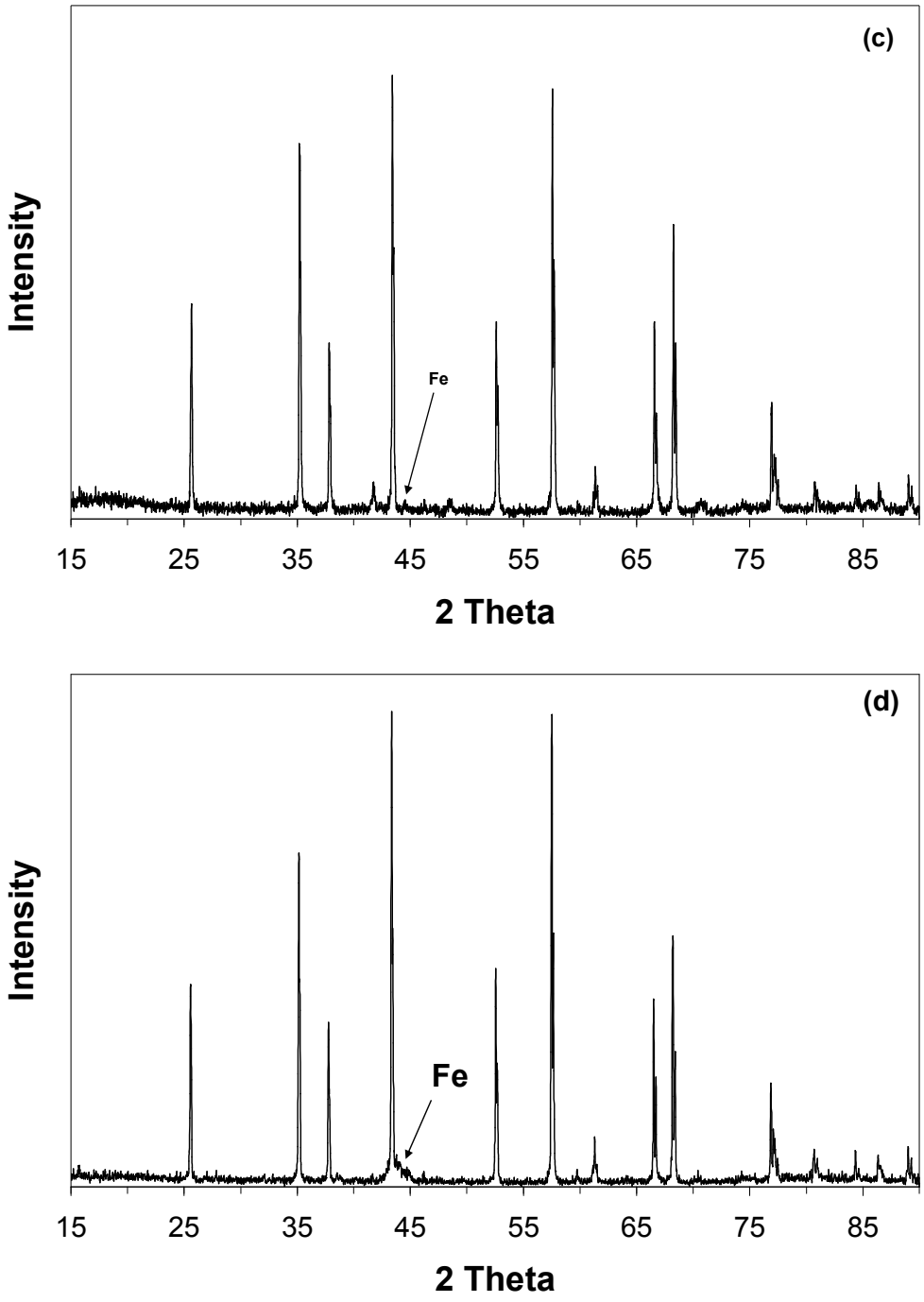

Figure A.1 continued

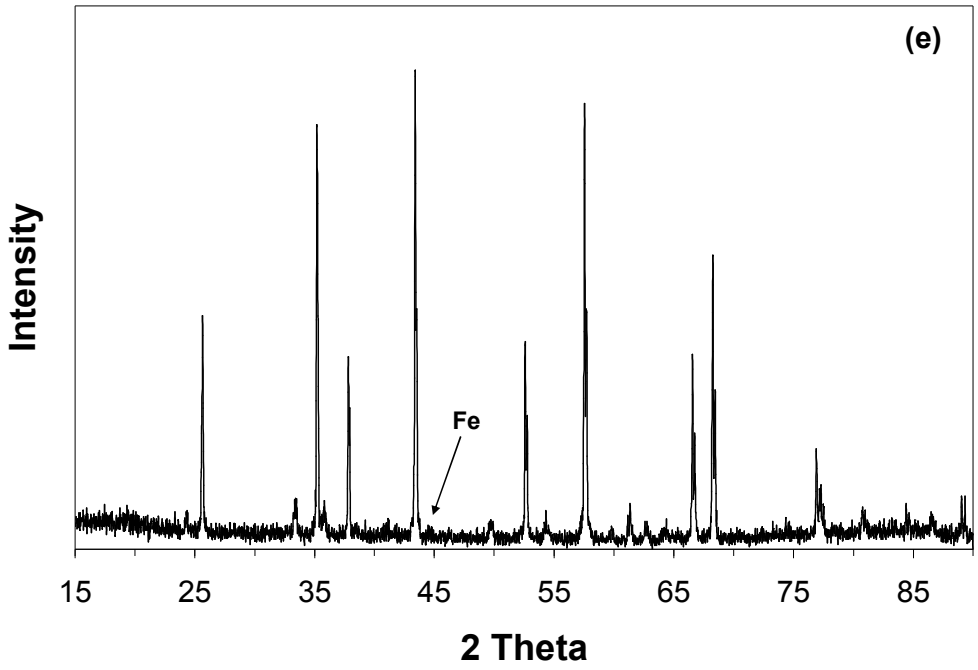

Figure A.1 continued

APPENDIX B

X-ray Diffraction Patterns of Other Systems Synthesized from the Gelation Chemical 3,3 Dimethyl Oxetane (DMO)

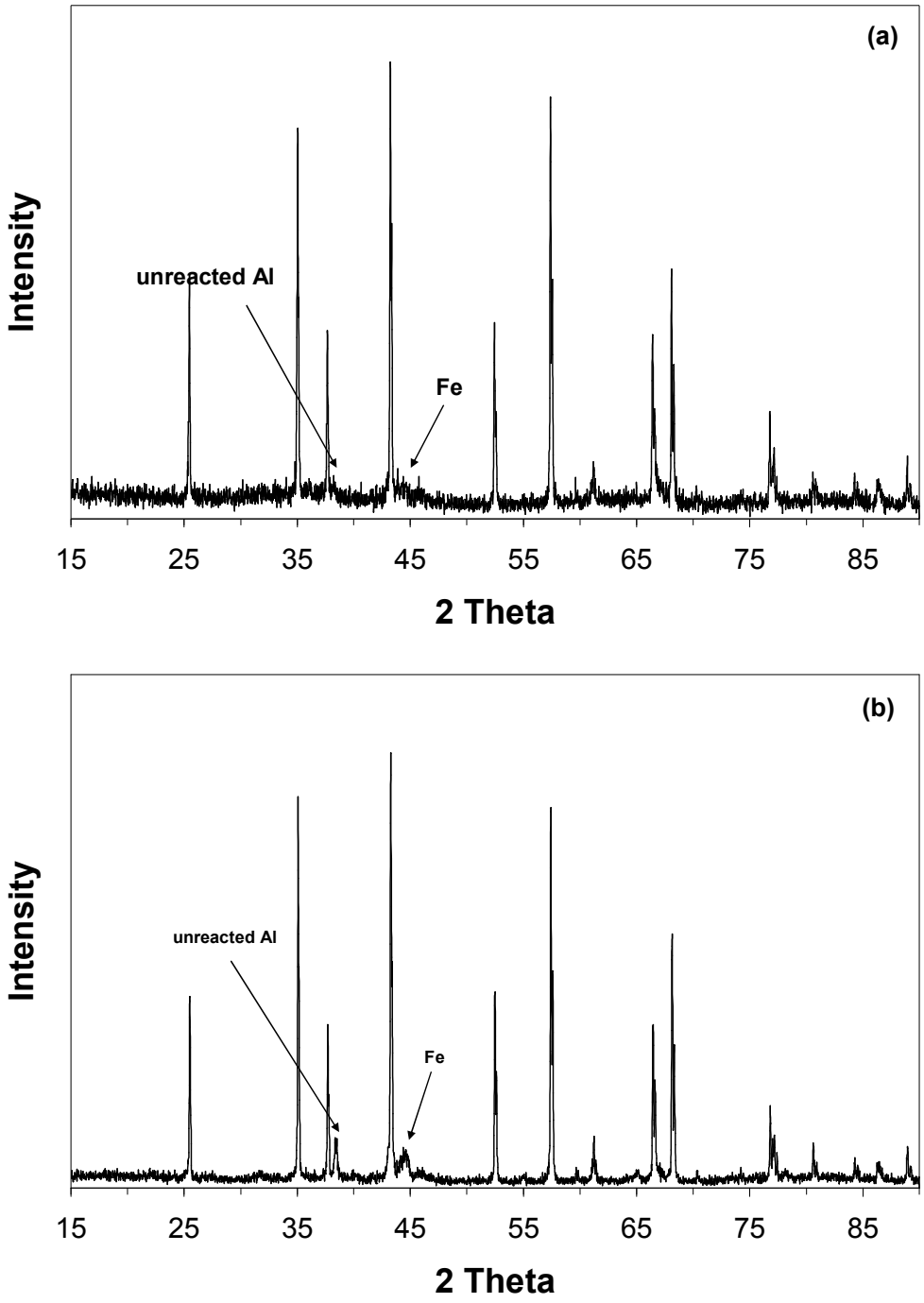

Figure A.2: XRD patterns of other iron (III) oxide/aluminum systems heated in a DTA to 1000°C at 10°C/min using 3,3 dimethyl oxetane as the gelation chemical. (a) Fe_2O_3/3x stoichiometric ratio of Fe:nano Al (3 x 0.083 g = 0.249 g Al), (b) Fe_2O_3/½ stoichiometric ratio of nano Al (½ x 0.083 g = 0.0415 g), (c) Fe_2O_3/1:1 Fe nano Al plus CNT, (d) Fe_2O_3/1:1 Fe:micron Al, and (e) Fe_2O_3/1:1 Fe:micron Al plus CNT.

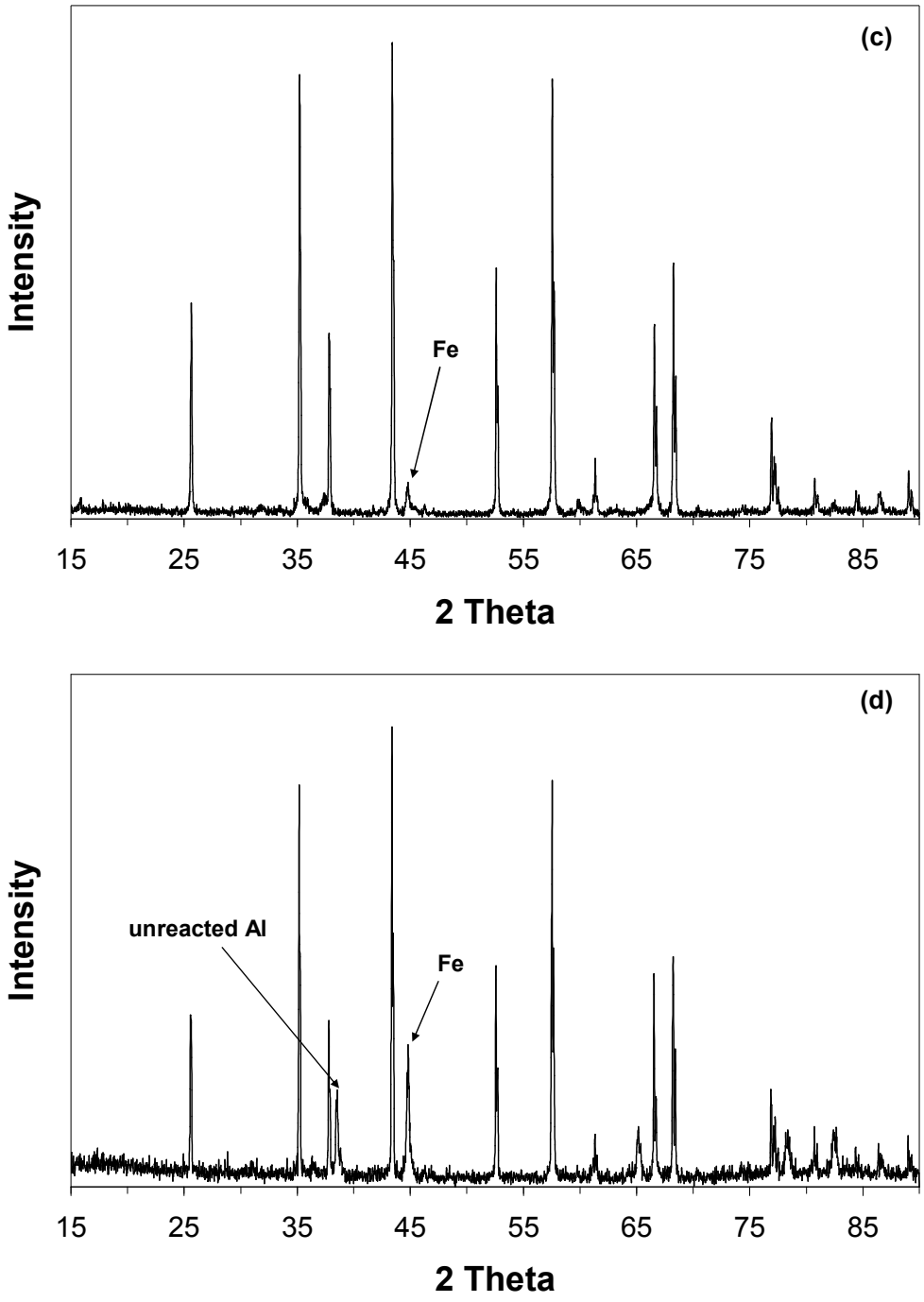

Figure A.2 continued

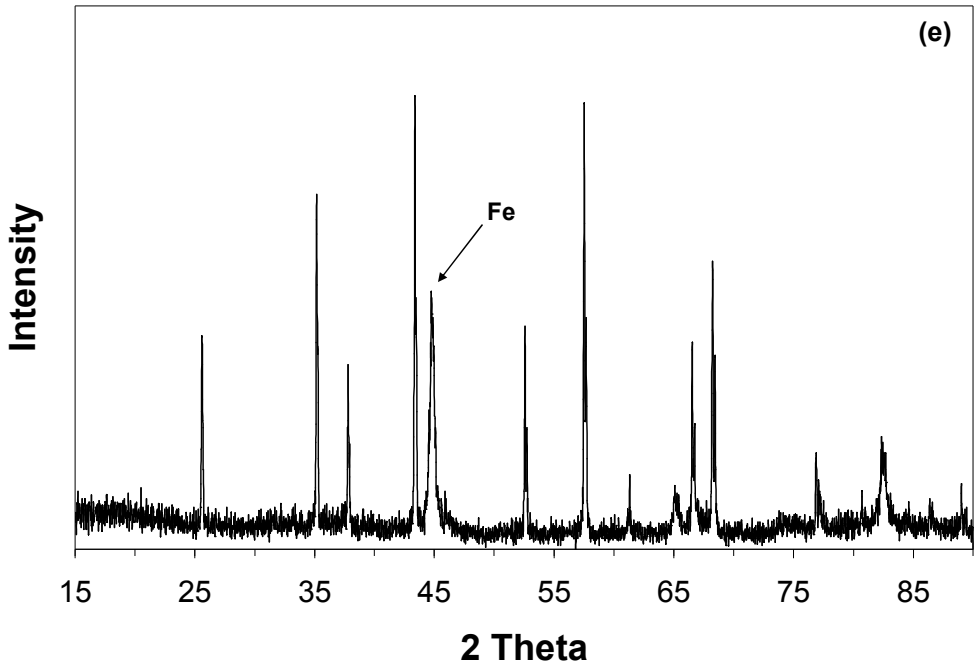

Figure A.2 continued

REFERENCES

1. Rugunanan, R. A.; Brown, M. E., Combustion of Binary and Ternary Silicon/oxidant Pyrotechnic Systems. Part I: Binary systems with Fe2O3 and SnO2 as Oxidants. *Combustustion Scence and Technology* **1994,** 95, 61-83.

2. Rugunanan, R. A.; Brown, M. E., Combustion of Binary and Ternary Silicon/oxidant Pyrotechnic Systems. Part II: Binary Systems with Sb2O3 and KNO3 as Oxidants. *Combustustion Scence and Technology* **1994,** 95, 85-99.

3. Simpson, R. L.; Tillotson, T. M.; Hrubesh, L. W.; Gash, A. E., Nanostructured Energetic Materials Derived from Sol-gel Chemistry. *Proceedings Institut Chemishe Energetic Materials Analysis, Diagnostic, and Testing Meeting* **2000**.

4. Prakash, A.; McCormick, A.; Zachariah, M., Aero-Sol-Gel Synthesis of Nanoporous Iron-Oxide Particles: A Potential Oxidizer for Nanoenergetic Materials. *Chemistry of Materials* **2004,** 16, 1466-1471.

5. Tillotson, T. M.; Gash, A. E.; Simpson, R. L.; Hrubesh, L. W.; Satcher, J. H. J.; Poco, J. F., Nanostructured Eneregetic Materials using Sol-Gel Methodologies. *Journal of Non-Crystalline Solids* **2001,** 285, 338-345.

6. Tillotson, T. M.; Hrubesh, L. W.; Simpson, R. L.; Lee, R. S.; Swansiger, R. W.; Simpson, L. R., Sol-gel processing of energetic materials. *Journal of Non-Crystalline Solids* **1998,** 225, 358-363.

7. Gash, A. E.; Simpson, R. L.; Satcher, J. H., Jr., Direct preparation of nanostructured energetic materials using sol-gel methods. *ACS Symposium Series* **2005,** 891, (Defense Applications of Nanomaterials), 198-210.

8. Pantoya, M. L.; Son, S. F.; Danen, W. C.; Jorgensen, B. S.; Asay, B. W.; Busse, J. R.; Mang, J. T., Characterization of metastable intermolecular composites. *ACS Symposium Series* **2005,** 891, (Defense Applications of Nanomaterials), 227-240.

9. Fischer, S. H.; Grubelich, M. C., Theoretical energy release of thermites, intermetallics, and combustible metals. *Proceedings of the International Pyrotechnics Seminar* **1998,** 24th, 231-286.

10. Bhattacharya, S.; Gao, Y.; Apperson, S.; Subramaniam, S.; Shende, R.; Gangopadhyay, S.; Talantsev, E., A Novel On-Chip Diagnostic Method to Measure Burn Rates of Energetic Materials. *Journal of Energetic Materials* **2006,** 24, 1-15.

11. Kim, S.; Zachariah, M., Enhancing the Rate of Energy Release from Nanoenergetic Materials by Electrostatically Enhanced Assembly. *Advanced Materials* **2004,** 16, (20), 1821-1825.

12. Patel, N. Intermediate strain rate behavior of two structural energetic materials. Georgia Institute of Technology, Atlanta, 2004.

13. Brown, M. E.; Taylor, S. J.; Tribelhorn, M. J., Fuel-oxidant particle contact in binary pyrotechnic reactions. *Propellants, Explosives, Pyrotechnics* **1998,** 23, (6), 320-327.

14. Valliappan, S.; Swiatkiewicz, J.; Puszynski, J. A., Reactivity of aluminum nanopowders with metal oxides. *Powder Technology* **2005,** 156, (2-3), 164.

15. Pantoya, M.; Granier, J., Combustion Behavior of Highly Energetic Thermites: Nano versus Micron Composites. *Propellants, Explosives, Pyrotechnics* **2005,** 30, (1), 53-62.

16. Ferguson, J. D.; Buechler, K. J.; Weimer, A. W.; George, S. M., SnO2 atomic layer deposition on ZrO2 and Al nanoparticles: Pathway to enhanced thermite materials. *Powder Technology* **2005,** 156, (2-3), 154-163.

17. Prentice, D.; Pantoya, M. L.; Clapsaddle, B. J., Effect of Nanocomposite Synthesis on the Combustion Performance of a Ternary Thermite. *Journal of Physical Chemistry B* **2005,** 109, (43), 20180-20185.

18. Plantier, K. B.; Pantoya, M. L.; Gash, A. E., Combustion wave speeds of nanocomposite Al/Fe2O3: the effects of Fe2O3 particle synthesis technique. *Combustion and Flame* **2005,** 140, (4), 299-309.

19. Wharton, R. K.; Formby, S. A.; Merrifield, R., Airblast TNT equivalence for a range of commercial blasting explosives. *Journal of Hazardous Materials* **2000,** 79, 31.

20. Goldschmidt, H., *Iron Age* **1908,** 82, 232.

21. Zumdahl, S., *Chemistry*. Third ed.; D.C. Heath and Company: Lexington, 1993; p 1123.

22. Wang, L. L.; Munir, Z. A.; Maximov, Y. M., Thermite reactions--their utilization in the synthesis and processing of materials. *Journal of Materials Science* **1993,** 28, 3693.

23. Lowe, T., The revolution in nanometals. *Advanced Materials and Processes* **2002,** 160, 63.

24. Pierre, A. C., *Introduction to sol-gel processing*. Kluwer Academic Publishers: Boston, 1998; p x, 394 p.

25. Richter, M.; Abramova, A.; Bentrup, U.; Fricke, R., Proof of Reversible Ag^{+}/Ag^{0} Redox Transformation on Mesoporous Alumina by in-situ UV-Vis Spectroscopy. *Journal of Applied Spectroscopy* **2004,** 71, (3), 400-403.

26. Diaz, A. N.; Lovillo, J.; Ramos Peinado, M. C., (4-Ethoxyphenyl)urea as a Fluorescence Probe in Sol-Gel Processes. *Chemistry of Materials* **1997,** 9, (12), 2647-2651.

27. Mukherjee, S. P., Sol-Gel processes in glass science and technology. *Journal of Non-Crystalline Solids* **1980,** 42, 477-488.

28. Battisha, I. K.; Afify, H. H.; Hamada, I. M., Structural and magnetic susceptibility studies of SiO2: Fe2O3 nano-composites prepared by sol-gel technique. *Journal of Magnetism and Magnetic Materials* **2005,** 292, 440.

29. West, A. R., *Basic Solid State Chemistry*. Second ed.; John Wiley & Sons, Ltd.: 1999.

30. Mabuchi, T.; Nishikiori, H.; Tanaka, N.; Fujii, T., Relationships Between Fluorescence Properties of Benzoquinolines and Physicochemical Changes in the Sol-Gel-Xerogel Transitions of Silicon Alkoxide Systems. *Journal of Sol-Gel Science and Technology* **2005,** 33, 333-340.

31. Eerenstein, W.; Kalev, L.; Niesen, L.; Palstra, T. T. M.; Hibma, T., Magneto-resistance and superparamagnetism in magnetite films on MgO and MgAl2O4. *Journal of magnetism and magnetic materials* **2003,** 258, 73.

32. Fabrizoli, P.; Burgi, T.; Baiker, A., Environmental Catalysis on Iron Oxide–Silica Aerogels: Selective
Oxidation of NH_3 and Reduction of NO by NH_3. *Journal of Catalysis* **2002,** 206, 143-154.

33. Lin, Y.; Sun, F. Q.; Yuan, X. Y.; Geng, B. Y.; Zhang, L. D., Sol-gel Electrophoretic Deposition and Optical Properties of Fe_2O_3 Nanowire Arrays. *Applied Physics A: Materials Science & Processing* **2004,** 78, (8), 1197.

34. Long, J. W.; Logan, M. S.; Rhodes, C. P.; Carpenter, E. E.; Stroud, R. M.; Rolison, D. R., Nanocrystalline Iron Oxide Aerogels as Mesoporous Magnetic Architectures. *Journal of the American Chemical Society* **2004,** 126, (51), 16879-16889.

35. Pajonk, G. M., Catalytic aerogels. *Catalysis Today* **1997,** 35, (3), 319.

36. Tongpool, R.; Jindasuwan, S., Sol-gel processed iron oxide-silica nanocomposite films as room-temperature humidity sensors. *Sensors and Actuators B: Chemical* **2005,** B106, (2), 523-528.

37. Wang, C.-T.; Ro, S.-H., Nanocluster iron oxide-silica aerogel catalysts for methanol partial oxidation. *Applied Catalysis A: General* **2005,** 285, (1-2), 196.

38. Clapsaddle, B.; Gash, A. E.; Satcher, J. H. J.; Simpson, R. L., Silicon Oxide in an iron (III) oxide matrix: the sol-gel synthesis and characterization of Fe-Si mixed oxide nanocomposites that contain iron oxide as the major phase. *Journal of Non-Crystalline Solids* **2003,** 331, 190-201.

39. Gash, A. E.; Tillotson, T. M.; Jr., J. H. S.; Poco, J. F.; Hrubesh, L. W.; Simpson, R. L., Use of Epoxides in the Sol-Gel Synthesis of Porous Iron(III) Oxide Monoliths from Fe(III) Salts. *Chemistry of Materials* **2001,** 13, (3), 999-1007.

40. Gash, A. E.; Satcher, J. H. J.; Simpson, R. L., Strong Akaganeite Aerogel Monoliths Using Epoxides: Synthesis and Characterization. *Chemistry of Materials* **2003,** 15, 3268-3275.

41. Pesiri, D.; Aumann, C. E.; Bilger, D.; Booth, R. D., Industrial Scale Nano-Aluminum Powder Manufacturing. *Journal of Pyrotechnics* **2004**, (19), 19.

42. Gash, A. E.; Satcher, J. H.; Simpson, R. L., Monolithic nickel(II)-based aerogels using an organic epoxide: the importance of the counterion. *Journal of Non-Crystalline Solids* **2004,** 350, 145-151.

43. Baumann, T. F.; Gash, A. E.; Chinn, S. C.; Sawvel, A. M.; Maxwell, R. S.; Satcher, J. H., Jr., Synthesis of High-Surface-Area Alumina Aerogels without the Use of Alkoxide Precursors. *Chemistry of Materials* **2005,** 17, (2), 395-401.

44. Gash, A. E.; Tillotson, T. M.; Satcher, J. H., Jr.; Hrubesh, L. W.; Simpson, R. L., New sol-gel synthetic route to transition and main-group metal oxide aerogels using inorganic salt precursors. *Journal of Non-Crystalline Solids* **2001,** 285, (1-3), 22-28.

45. Aitasalo, T.; Holsa, J.; Jungner, H.; Lastusaari, M.; Niittykoski, J.; Saarinen, J., Eu2+ doped calcium aluminate coatings by sol-gel methods. *Optical Materials* **2005,** 27, (9), 1537.

46. Baiju, K. V.; Sibu, C. P.; Rajesh, K.; Pillai, P. K.; Mukundan, P.; Warrier, K. G. K.; Wunderlich, W., An aqueous sol-gel route to synthesize nanosized lanthana-doped titania having an increased anatase phase stability for photocatalytic application. *Materials Chemistry and Physics* **2005,** 90, (1), 123.

47. Celerier, S.; Laberty-Robert, C.; Ansart, F.; Calmet, C.; Stevens, P., Synthesis by sol-gel route of oxyapatite powders for dense ceramics: Applications as electrolytes for solid oxide fuel cells. *Journal of the European Ceramic Society* **2005,** 25, (12), 2665.

48. Fu, L. J.; Liu, H.; Li, C.; Wu, Y. P.; Rahm, E.; Holze, R.; Wu, H. Q., Electrode materials for lithium secondary batteries prepared by sol-gel methods. *Progress in Materials Science* **2005,** 50, (7), 881.

49. Garcia Cerda, L. A.; Montemayor, S. M., Synthesis of CoFe2O4 nanoparticles embedded in a silica matrix by the citrate precursor technique. *Journal of Magnetism and Magnetic Materials* **2005,** 294, (2), e43.

50. Houbertz, R., Laser interaction in sol-gel based materials--3-D lithography for photonic applications. *Applied Surface Science* **2005,** 247, (1-4), 504.

51. Hsiao, C. N.; Huang, K. S., Synthesis, characterization, and applications of polyvinylpyrrolidone/SiO2 hybrid materials. *Journal of Applied Polymer Science* **2005,** 96, (5), 1936-1942.

52. Huang, X. H.; Chen, Z. H., Preparation of CoFe2O4/SiO2 nanocomposites by sol-gel method. *Journal of Crystal Growth* **2004,** 271, 287-293.

53. Huang, X.-H.; Chen, Z.-H., Sol-gel preparation and characterization of CoFe2O4-SiO2 nanocomposites. *Solid State Communications* **2004,** 132, (12), 845.

54. Jan, S.-S.; Chen, Y.-C.; Chou, J.-C., Effect of Mg2+-dopant on the characteristics of lead titanate sensing membrane for ion-sensitive field-effect transistors. *Sensors and Actuators B: Chemical* **2005,** 108, (1-2), 883.

55. Kiisk, V.; Sildos, I.; Lange, S.; Reedo, V.; Tatte, T.; Kirm, M.; Aarik, J., Photoluminescence characterization of pure and Sm3+-doped thin metaloxide films. *Applied Surface Science* **2005,** 247, (1-4), 412.

56. Mao, L.; Li, Q.; Dang, H.; Zhang, Z., Synthesis of nanocrystalline TiO2 with high photoactivity and large specific surface area by sol-gel method. *Materials Research Bulletin* **2005,** 40, (2), 201.

57. Miyake, H.; Kozuka, H., Photoelectrochemical Properties of Fe_2O_3-NbO_5 Films Prepared by Sol-Gel Method. *Journal of Physical Chemistry B* **2005,** 109, 17951-17956.

58. Moussa, N.; Ghorbel, A.; Grange, P., Vanadia-Silica Catalysts Prepared by Sol-Gel Method: Application for Epoxidation Reaction. *Journal of Sol-Gel Science and Technology* **2005,** 33, (1), 127-132.

59. Pustelny, T.; Zielonka, I.; Karasinski, P.; Jurusik, J., Bragg's grating coupler in planar optical sol-gel waveguides. *Optica Applicata* **2004,** 34, (4), 477-487.

60. Ristic, M.; Popovic, S.; Music, S., Application of sol-gel method in the synthesis of gallium(III)-oxide. *Materials Letters* **2005,** 59, (10), 1227.

61. Xomeritakis, G.; Tsai, C.-Y.; Brinker, C. J., Microporous sol-gel derived aminosilicate membrane for enhanced carbon dioxide separation. *Separation and Purification Technology* **2005,** 42, (3), 249.

62. Kolawa, E.; So, F. C. T.; Flick, W.; Zhao, X. A.; Pan, E. T.; Nicolet, M. A., Reactive sputtering of ruthenium dioxide films. *Thin Solid Films* **1989,** 173, (2), 217-24.

63. Zhitomirsky, I.; Gal-Or, L., Ruthenium oxide deposits prepared by cathodic electrosynthesis. *Materials Letters* **1997,** 31, (1,2), 155-159.

64. Ardizzone, S.; Daghetti, A.; Franceschi, L.; Trasatti, S., The point of zero charge of hydrous ruthenium dioxide. *Colloids and Surfaces* **1989,** 35, (1), 85-96.

65. Panic, V.; Dekanski, A.; Miskovic-Stankovic, V. B.; Milonjic, S.; Nikolic, B., On the deactivation mechanism of RuO2-TiO2/Ti anodes prepared by the sol-gel procedure. *Journal of Electroanalytical Chemistry* **2005,** 579, (1), 67-76.

66. Suffredini, H. B.; Tricoli, V.; Avaca, L. A.; Vatistas, N., Sol-gel method to prepare active Pt-RuO2 coatings on carbon powder for methanol oxidation. *Electrochemistry Communications* **2004,** 6, (10), 1025-1028.

67. Kim, I.-H.; Kim, K.-B., Ruthenium oxide thin film electrodes for supercapacitors. *Electrochemical and Solid-State Letters* **2001,** 4, (5), A62-A64.

68. Harper, J. M. E.; Hoernstroem, S. E.; Thomas, O.; Charai, A.; Krusin-Elbaum, L., Mechanisms for success or failure of diffusion barriers between aluminum and silicon. *Journal of Vacuum Science & Technology, A: Vacuum, Surfaces, and Films* **1989,** 7, (3, Pt. 1), 875-80.

69. Krusin-Elbaum, L.; Wittmer, M.; Yee, D. S., Characterization of reactively sputtered ruthenium dioxide for very large scale integrated metalization. *Applied Physics Letters* **1987,** 50, (26), 1879-81.

70. Jevtic, M. M.; Jelenkovic, E. V.; Tong, K. Y.; Pang, G. K. H., Noise and structural properties of reactively sputtered RuO2 thin films. *Thin Solid Films* **2006,** 496, (2), 214-220.

71. McKeown, D. A.; Hagans, P. L.; Carette, L. P. L.; Russell, A. E.; Swider, K. E.; Rolison, D. R., Structure of Hydrous Ruthenium Oxides: Implications for Charge Storage. *Journal of Physical Chemistry B* **1999,** 103, (23), 4825-4832.

72. Swider-Lyons, K. E.; Love, C. T.; Rolison, D. R., Selective vapor deposition of hydrous RuO2 thin films. *Journal of the Electrochemical Society* **2005,** 152, (3), C158-C162.

73. Kim, K. S.; Winograd, N., X-ray photoelectron spectroscopic studies of ruthenium-oxygen surfaces. *Journal of Catalysis* **1974,** 35, (1), 66-72.

74. Suh, D. J., Catalytic applications of composite aerogels. *Journal of Non-Crystalline Solids* **2004,** 350, 314-319.

75. Terezo, A. J.; Pereira, E. C., Preparation and characterisation of Ti/RuO2 anodes obtained by sol-gel and conventional routes. *Materials Letters* **2002,** 53, (4-5), 339-345.

76. Sahul, R.; Tasovski, V.; Sudarshan, T. S., Ruthenium oxide cryogenic temperature sensors. *Sensors and Actuators, A: Physical* **2006,** A125, (2), 358-362.

77. Bhaskar, S.; Dobal, P. S.; Majumder, S. B.; Katiyar, R. S., X-ray photoelectron spectroscopy and micro-Raman analysis of conductive RuO2 thin films. *Journal of Applied Physics* **2001,** 89, (5), 2987-2992.

78. Sugimoto, W.; Yokoshima, K.; Ohuchi, K.; Murakami, Y.; Takasu, Y., Fabrication of Thin-Film, Flexible, and Transparent Electrodes Composed of Ruthenic Acid Nanosheets by Electrophoretic Deposition and Application to Electrochemical Capacitors. *Journal of the Electrochemical Society* **2006,** 153, (2), A255-A260.

79. Suh, D. J.; Park, T.-J.; Kim, W.-I.; Hong, I.-K., Synthesis of high-surface-area ruthenium oxide aerogels by non-alkoxide sol-gel route. *Journal of Power Sources* **2003,** 117, (1-2), 1-6.

80. Min, M.; Machida, K.; Jang, J. H.; Naoi, K., Hydrous RuO2/Carbon Black Nanocomposites with 3D Porous Structure by Novel Incipient Wetness Method for Supercapacitors. *Journal of the Electrochemical Society* **2006,** 153, (2), A334-A338.

81. Zheng, J. P.; Cygan, P. J.; Jow, T. R., Hydrous ruthenium oxide as an electrode material for electrochemical capacitors. *Journal of the Electrochemical Society* **1995,** 142, (8), 2699-703.

82. Cordfunke, E. H. P.; Konings, R. J. M., The enthalpy of formation of ruthenium dioxide. *Thermochimica Acta* **1988,** 129, 63-69.

83. Mucklich, F.; Ilic, N., RuAl and its alloys. Part I. Structure, physical properties, microstructure and processing. *Intermetallics* **2004,** 13, (1), 5-21.

84. Livage, J.; Henry, M.; Sanchez, C., Sol-gel chemistry of transition metal oxides. *Progress in Solid State Chemistry* **1988,** 18, (4), 259-341.

85. Dobinson, B.; Hofmann, W.; Stark, B. P., *The Determination of Epoxides*. Pergamon Press: Oxford, 1969.

86. Schamm, S.; Berjoan, R.; Barathieu, P., Study of the chemical and structural organization of SIPOS films at the nanometer scale by TEM-EELS and XPS. *Materials Science and Engineering B* **2004,** 107, (1), 58.

87. Briggs, D.; Seah, M. P., *Practical Surface Analysis*. John Wiley & Sons: Chicester, 1983; p 533.

88. Tan, B. J.; Klabunde, K. J.; Sherwood, P. M. A., X-ray Photoelectron Spectroscopy Studies of Solvated Metal Atom Dispersed Catalysts. Monometallic Iron and Bimetallic Iron-Cobalt Particles on Alumina. *Chemistry of Materials* **1990,** 2, 186-191.

89. Mills, P.; Sullivan, J. L., A study of the core level electrons in iron and its three oxides by means of x-ray photoelectron spectroscopy. *Journal of Physics D: Applied Physics* **1983,** 16, 723-732.

90. Tannenbaum, R.; Hakanson, C.; Zeno, A. D.; Tirrell, M., Spectroscopic Study of the Chemistry at the Cr-PMMA Interface. *Langmuir* **2002,** 18, (14), 5592-5599.

91. Wagner, C. D.; Riggs, W. M.; Davis, L. E.; Moulder, J. F., *Handbook of X-ray Photoelectron Spectroscopy*. 1st Edition ed.; Perkin-Elmer Corporation (Physical Electronics): 1979.

92. Tannenbaum, R.; Rutkowska, M.; Eisenberg, A., Ionomeric Blends. V. FTIR Studies of Ionic Interactions in Polyurethane-Styrene Blends. *Journal of Polymer Science* **1987,** 25, 663-671.

93. Cummings, D. L.; Wood, J. L., In-plane vibrations of the pyridinium ion. *Journal of Molecular Structure* **1973,** 17, (2), 257-64.

94. Florian, J.; Kubelkova, L.; Kotrla, J., Vibrational spectra of hydrogen-bonded complexes on zeolite surfaces as a benchmark for evaluating performance of ab initio

methods. Complex with the pyridinium ion. *Journal of Molecular Structure* **1995,** 349, 435-8.

95. Glazunov, V. P.; Odinokov, S. E., Infrared spectra of pyridinium salts in solution. I. The region of middle frequencies. *Spectrochimica Acta, Part A: Molecular and Biomolecular Spectroscopy* **1982,** 38A, (4), 399-408.

96. Harmon, K. M.; Shaw, K. E., Hydrogen bonding. Part 71. Hydrogen bonding effects on the spectra, solubility, and F- reactivity of 2,3- and 3,4-dicarboxypyridines: identification of a bifurcated hydrogen bond in 2,3-dicarboxypyridine. *Journal of Molecular Structure* **1999,** 513, (1-3), 219-230.

97. Ada, E. T.; Hanley, L.; Etchin, S.; MeIngailis, J.; Dressick, W. J.; Mu-San, C.; Calvert, J., Ion Beam Modification and Patterning of Organosilane Self-Assembled Monolayers. *Journal of Vacuum Science and Technology B* **1995,** 13, (6), 2189-2196.

98. Lupis, C. H. P., *Chemical Thermodynamics of Materials*. Prentice-Hall, Inc.: New York, 1983; p 581.

99. Duraes, L.; Costa, B. F. O.; Vasques, J.; Campos, J.; Portugal, A., Phase investigation of as-prepared iron oxide/hydroxide produced by sol-gel synthesis. *Materials Letters* **2005,** 59, (7), 859.

100. Schaffer, J. P.; Saxena, A.; Antolovich, S. D.; Thomas H. Sanders, J.; Warner, S. B., *The Science and Design of Engineering Materials*. 2nd Ed. ed.; WCB McGraw-Hill: Boston, 1999; p 826.

101. Munir, Z. A.; Anselmi-Tamburini, U., Self-propagating exothermic reactions: The synthesis of high-temperature materials by combustion. *Materials Science Reports* **1989,** 3, (7-8), 277.

102. Eckert, J.; Holzer, J. C.; Ahn, C. C.; Fu, Z.; Johnson, W. L., Melting behavior of nanocrystalline aluminum powders. *Nanostructured Materials* **1993,** 2, (4), 407.

103. Froment, P.; Genet, M. J.; Devillers, M., Surface reduction of ruthenium compounds with long exposure to an X-ray beam in photoelectron spectroscopy. *Journal of Electron Spectroscopy and Related Phenomena* **1999,** 104, (1-3), 119.

104. Rolison, D. R.; Hagans, P. L.; Swider, K. E.; Long, J. W., Role of Hydrous Ruthenium Oxide in Pt-Ru Direct Methanol Fuel Cell Anode Electrocatalysts: The Importance of Mixed Electron/Proton Conductivity. *Langmuir* **1999,** 15, (3), 774-779.

105. Ji, L.; Lin, J.; Zeng, H. C., Thermal processes of volatile RuO2 in nanocrystalline Al2O3 matrixes involving g->a phase transformation. *Chemistry of Materials* **2001,** 13, (7), 2403-2412.

106. Pagnaer, J.; Nelis, D.; Mondelaers, D.; Vanhoyland, G.; D'Haen, J.; Van Bael, M. K.; Van den Rul, H.; Mullens, J.; Van Poucke, L. C., Synthesis of RuO2 and SrRuO3 powders by means of aqueous solution gel chemistry. *Journal of the European Ceramic Society* **2004,** 24, (6), 919-923.

107. Campbell, P. F.; Ortner, M. H.; Anderson, C. J., Differential thermal analysis and thermogravimetric analysis of fission product oxides and nitrates to 1500 Deg. *Anal. Chem.* **1961,** 33, 58-61.

108. Povarova, K. B.; Padalko, A. G.; Drozdov, A. A.; Kasanskaya, N. K.; Korenovskii, N. L.; Skachkov, O. A.; Veselov, A. N.; Morozov, A. E.; Bannykh, I. O., Differential barothermal analysis in the course of reactive powder barothermal processing of RuAl alloys. *Journal of Thermal Analysis and Calorimetry* **2005,** 80, (3), 607-612.

109. Wolff, I. M., Synthesis of RuAl by reactive powder processing. *Metallurgical and Materials Transactions A: Physical Metallurgy and Materials Science* **1996,** 27A, (11), 3688-3699.

110. Gobran, H. A.; Ilic, N.; Mucklich, F., Effects of particle size and pressure on the reactive sintering of RuAl intermetallic compound. *Intermetallics* **2004,** 12, (5), 555-562.

VITA

JEREMY D. WALKER

Jeremy Duane Walker was born in Toledo, OH in 1978. He attended Lucy Ragsdale High School in Jamestown, NC, graduating in 1996, at which point he enrolled at North Carolina State University in Raleigh, NC. Walker graduated Magna Cum Laude with a B.S. in Chemical Engineering and a minor in French Language in 2000. After graduation, he accepted a position as a Materials Research Engineer at Alcatel Telecommunications in Claremont, NC, before pursuing his Ph.D. at Georgia Institute of Technology in Materials Science and Engineering.